^{57}Fe and ^{119}Sn Mössbauer studies on new Heusler compounds for spintronic applications

Dissertation
zur Erlangung des Grades
"Doktor der Naturwissenschaften"
am Fachbereich Chemie, Pharmazie und Geowissenschaften
der Johannes Gutenberg-Universität Mainz

vorgelegt von
Teuta Gasi
geboren in Skopje-Mazedonien

Mainz, 2013

Für meine Familie

Tag der mündlichen Prüfung: 26.06.2013

Die vorliegende Arbeit wurde in der Zeit von Februar 2010 bis Februar 2013 am Institut für Anorganische und Analytische Chemie im Fachbereich Chemie, Pharmazie und Geowissenschaften der Johannes Gutenberg-Universität, Mainz angefertigt.

Mainz, Februar 2013

Hiermit versichere ich, dass ich die vorliegende Dissertation selbstständig verfasst und keine anderen als die angegebenen Hilfsmittel benutzt habe. Alle der Literatur entnommenen Stellen sind als solche gekennzeichnet.

Mainz, Februar 2013

Contents

9 Structural and magnetic properties of $\mathrm{Mn}_{3-x}\mathrm{Fe}_x\mathrm{Ga}$ 105

1 Abstract

Since the huge variety of applications in spintronics using Heusler compounds has grown in the last decade, the progress on searching this family of alloys can be followed in numerous published papers. A typical Heusler compound X_2YZ consists of two transition elements (X, Y) and of one main group element (Z). This thesis reports on Heusler alloys with particular interest in their potential half-metallic properties, and on those which could show a perpendicular magnetic anisotropy (PMA). The latter is attractive for use in spin torque transfer devices and occurs in tetragonally distorted Heusler compounds. Spin transfer torque (STT) is an effect which uses a spin polarized current to influence/change the orientation of a magnetic layer. The most significant results in this thesis are: the synthesis of new cubic Heusler phases Fe_2YZ which theoretically were predicted as tetragonal (chapter one); the synthesis of Mn_2FeGa , which appears in the tetragonal structure interesting for STT (chapter 2); the synthesis of Fe_2MnGa with a magnetic phase transition, in particular exhibiting the exchange bias (EB)-effect, which is based on the coexistence of a ferromagnetic and an antiferromagnetic phase (chapter 3), and finally the synthesis of the series $Mn_{3-x}Rh_xSn$ (chapter 4), which offers tetragonal Mn_2RhSn as a potential material for spintronic devices. In this thesis, Heusler compounds have been synthesized and investigated that contain at least one Mössbauer atomic probe, namely ^{57}Fe and ^{119}Sn. The application of Heusler compounds is based on their peculiar crystal structure and the resulting electronic and magnetic properties. Selected materials were studied in detail using XRD-measurements to characterize their crystal structure, whereas additionally their magnetic properties were investigated by applying SQUID magnetometry and by measuring hyperfine magnetic fields on Fe or the induced hyperfine magnetic fields on Sn-atoms, respectively, by means of Mössbauer spectroscopy. In case of the Heusler compounds studied here Mössbauer spectroscopy plays a major role, since Heuslers mostly exhibit a certain disorder, which could influence their magnetic and structural properties. The type of disorder can be hardly determined only from the laboratory powder XRD, that is why we use the advantage of Mössbauer spectroscopy as a local method to clarify the type and degree of disorder. This thesis is structured as follows:

In chapter 1, the new soft ferromagnetic cubic Heusler phases Fe_2NiGe, Fe_2CuGa and Fe_2CuAl were synthesized and characterized. In previous theoretical studies they have been predicted to exist in a tetragonal Heusler structure. However, our experimental results revealed that these compounds basically crystallize in the cubic inverse Heusler (X-) structure with differing degrees of atomic disorder. One may suppose that disorder prevents the crystallization of the tetragonal phase. Mössbauer spectroscopy was used as a powerful local technique to clarify the degree of disorder and to estimate the magnetic moments at the iron sites. All the compounds are soft ferromagnets with high Curie temperatures up to 900 K which makes them suitable for potential magnetic applications.

Chapter 2 reports about the synthesis and investigation of Mn_2FeGa. It has been found that Mn_2FeGa annealed at 400 °C adopts the inverse tetragonal structure ($I\bar{4}m2$). Theoretically, it was suggested to exist in the inverse cubic Heusler structure. Depending on the synthesis conditions, magnetic and structural properties of Mn_2FeGa crucially change. Hence, the crystal structure of Mn_2FeGa annealed at 800 °C changes to a pseudocubic Cu_3Au-like structure, where Fe and Mn atoms are statistically distributed. This change of crystal structure has been confirmed by Mössbauer results due to the occurrence and absence of the quadrupole splitting in case of the inverse tetragonal and the pseudocubic structure, respectively. However, the inverse tetragonal structure, the hard magnetic behavior and the high thermal stability of the magnetization up to 650 K suggest that Mn_2FeGa annealed at 400 °C could be a a material for spin torque transfer applications (STT). Additional advantages could be achieved especially if this sample is optimized as thin film.

In chapter 3, Fe_2MnGa was also successfully synthesized and investigated by various techniques. The relation between the crystal and magnetic properties has been investigated by changing the annealing conditions and by mechanical treatment. The XRD patterns for all the compounds are similar and correspond to a pseudocubic Cu_3Au-like structure. However, the Mössbauer data and magnetic properties considerably differ from each other. The broad features in the spectra are an evidence of disorder in all the samples. It follows that changing the annealing conditions and mechanical treatment influences the local arrangement of the atoms which determines the magnetic properties. Emphasis was on an as-grown sample without further annealing, which undergoes a FM-AFM transition. This magnetic transition leads to a large EB behavior, which mainly originates from the co-existence of FM and AFM phases below the FM-AFM transition temperature. This particular behavior and the high T_C makes this compound also attractive and suitable for technological applications.

Chapter 4 is devoted to new Mn-based Heusler compounds $Mn_{3-x}Rh_xSn$, where we have tried to induce a transition in hexagonal Mn_3Sn to a tetragonal structure by replacing the Mn by the larger Rh atom. The XRD measurements have proved the presence of the inverse tetragonal structure ($I\bar{4}m2$) in four samples (Mn_2RhSn, $Mn_{2.1}Rh_{0.9}Sn$, $Mn_{2.3}Rh_{0.7}Sn$ and $Mn_{2.4}Rh_{0.6}Sn$) from this series. Interesting were found to be Mn_2RhSn and $Mn_{2.1}Rh_{0.9}Sn$, since they appeared to be a single phase, whereas the other compounds are mixed phases and also strongly disordered. The latter was confirmed by ^{119}Sn-Mössbauer measurements. Temperature dependent Mössbauer spectra point to the coexistence of phases with different magnetic ordering temperatures, the relative fraction of which differs in the various materials. The phases Mn_2RhSn and $Mn_{2.1}Rh_{0.9}Sn$ occur in the inverse tetragonal structure and reveal hard ferrimagnetic behavior. This property is one of the main criteria that a compound should fulfill for being a candidate for STT. Finally in the Appendix a large variety of $Mn_{3-x}Fe_xGa$ materials with $1 \leq x \leq 3$ is documented which are disorderd and frequently phase mixtures.

2 Zusammenfassung

Seit der Entwicklung einer großen Vielfalt von Anwendungsmöglichkeiten der Spintronik auf Basis von Heusler Verbindungen innerhalb der letzten Dekade kann der Forschungsfortschritt an dieser Material Klasse in einer Vielzahl von Publikationen verfolgt werden. Eine typische Heusler Verbindung X_2YZ besteht aus zwei Übergangsmetallen (X, Y) und einem Hauptgruppenelement (Z). Diese Arbeit berichtet von Heusler Verbindungen mit besonderem Augenmerk auf deren potentielle halbmetallische Eigenschaften und davon insbesondere solche, die eine richtungsabhängige magnetische Anisotropie (perpendicular magnetic anisotropy-PMA) zeigen könnten. PMA ist insbesondere für Spin transfer Torque (STT) Bauelemente von großem Interesse und tritt in tetragonal verzerrten Heusler Verbindungen auf. Bei STT-Elementen werden mittels spinpolarisierter Ströme die magnetische Orientierung von magnetischen Schichten beinflusst. Die signifikantesten Ergebnisse dieser Arbeit sind: die Synthese neuer kubischen Heusler Phasen Fe_2YZ, die theoretisch als tetragonal vorausgesagt wurden (Kapitel 1), die Synthese von Mn_2FeGa, das in der tetragonal verzerrten Struktur kristallisiert und Potential für STT Anwendungen zeigt (Kapitel 2); die Synthese von Fe_2MnGa, das einen magnetischen Phasenübergang mit exchange-bias (EB) Effekt zeigt, der auf einer Koexistenz von ferromagnetischen (FM) und antiferromagnetischen (AFM) Phasen beruht (Kapitel 3); Schlussendlich wird in Kapitel 4 die Synthese von $Mn_{3-x}Rh_xSn$ diskutiert, in welcher insbesondere tetragonales Mn_2RhSn als potentielles Material für Anwendungen in der Spintronik vorgestellt wird.

In dieser Arbeit wurden hauptsächlich Heusler Verbindungen mit mößbaueraktiven Elementen ^{57}Fe und ^{119}Sn, synthetisiert und untersucht. Die Anwendbarkeit von Heusler Verbindungen basiert auf ihrer speziellen Kristallstruktur und den daraus resultierenden elektronischen und magnetischen Eigenschaften. Die Kristallstruktur ausgewählter Materialien wurde durch XRD Messungen charakterisiert und zusätzlich wurden die magnetischen Eigenschaften mittels SQUID-Magnetometrie untersucht, sowie durch das Messen von Hyperfeinfeldern von Fe und induzierten Hyperfeinfeldern in Sn mittels Mößbauer Spektroskopie.

Im Falle der hier untersuchten Heusler Verbindungen spielt die Charakterisierung durch Mößbauer Spektroskopie eine entscheidende Rolle, da Heusler Verbindungen meistens ein gewisses Mass an Fehlordnung aufweisen, welche deren magnetischen und strukturellen Eigenschaften beeinflussen kann. Die Art der Fehlordnung jedoch kann nur schwer durch standard Pulver-Röntgendiffraktion bestimmt werden, weshalb wir die Vorteile der Mößbauer Spektroskopie als lokale Methode nutzen, um den Typ und den Grad der Fehlordnung aufzuklären. Diese Arbeit ist wie folgt gegliedert:

In Kapitel 1 wurden die neuen, kubisch-weichferromagnetischen Heuslerphasen Fe_2NiGe, Fe_2CuGa und Fe_2CuAl synthetisiert und charakterisiert. In vorangegangenen theoretischen Studien wurde für deren Existenz in tetragonaler Heuslerstruktur vorhergesagt. Ungeachtet dessen belegten unsere experimentellen Untersuchungen, dass diese

Verbindungen hauptsächlich in der kubischen invers Heusler(X-)struktur mit unterschiedlichen Anteilen an atomarer Fehlordnung kristallisieren. Es ist anzunehmen, dass diese Fehlordnung die Kristallisation in einer tetragonalen Phase verhindert. Mößbauer Spektroskopie wurde als kraftvolle lokale Technik eingesetzt, um den Grad der Fehlordnung zu bestimmen und die magnetischen Momente der Eisenpositionen abzuschätzen. Alle Verbindungen sind weiche Ferromagneten mit hoher Curietemperatur bis zu 900 K, weswegen alle als potentielle Materialien für magnetische Anwendungen geeignet sind.
In Kapitel 2 wurde Mn_2FeGa synthetisiert. Es zeigte sich, dass Mn_2FeGa nach Temperatur Nachbehandlung bei 400 °C die invers tetragonale Struktur ($I\bar{4}m2$) annimmt. Theoretisch wurde die Existenz in der inversen kubischen Heuslerstruktur vorausgesagt. Abhängig von den Synthesebedingungen ändern sich die magnetischen und strukturellen Eigenschaften von Mn_2FeGa eklatant. Deshalb ändert sich die Kristallstruktur von M_2FeGa bei Temperung bei 800 °C zu einer pseudokubischen Cu_3Au-artigen Struktur, in welcher Fe- und Mn-Atome statistisch verteilt vorliegen. Dieser Übergang der Kristallstrukturen wurde durch Mößbauer Spektroskopie anhand des Vorliegens oder Fehlens der Quadrupolaufspaltung im Falle der invers tetragonalen bzw. pseudokubischen Modifikation nachgewiesen. Dennoch legen die invers tetragonale Struktur, das hardmagnetische Verhalten und die hohe thermische Stabilität der Magnetisierung bis zu 650 K nahe, dass Mn_2FeGa bei 400 °C getempert ein geeignetes Material für spin torque transfer Anwendungen sein kann. Weitere Vorteile dieser Verbindung könnten insbesondere durch Optimierung als dünne Filme erreicht werden.
In Kapitel 3 wurde Fe_2MnGa ebenfalls erfolgreich synthetisiert und durch verschiedene Methoden charakterisiert. Der Zusammenhang von Kristallstruktur und magnetischen Eigenschaften wurde durch verschiedene Temperungskonditionen und mechanischer Behandlung untersucht. Die XRD-Messungen aller Verbindungen sind ähnlich und weisen auf eine pseudokubische Cu_3Au-artige Struktur hin. Dennoch unterscheiden sich die Mößbauerdaten und magnetischen Eigenschaften deutlich voneinander. Die große Bandbreite der spektroskopischen Daten sind ein Beweis für die Fehlordnung in allen Proben. Daraus folgt, dass eine Veränderung der Temperungungskonditionen und der mechanischen Behandlung Einfluss auf die lokale Anordnung der Atome hat, welche wiederum die magnetischen Eigenschaften bestimmt. Der Schwerpunkt lag auf einer geschmolzenen Probe ohne weitere Temperung, die einen FM-AFM Phasenübergang zeigte. Diese magnetische Phasenumwandlung führt zu einem starken EB-Verhalten, welches seinen Ursprung hauptsächlich in der Koexistenz von FM- und AFM-Phasen unterhalb der FM-AFM-Übergangstemperatur hat. Dieses spezielle Verhalten und die hohe T_C machen diese Verbindung ebenfalls attraktiv und geeignet für technische Anwendungen.
Kapitel 4 ist den neuen Mn-basierten Heusler-Verbindungen $Mn_{3-x}Rh_xSn$ gewidmet, bei denen wir versuchten, durch den Austausch von Mn durch das größere Rh eine Umwandlung zu einer tetragonalen Struktur von den hexagonalen Mn_3Sn-Struktur zu erreichen. Die XRD-Messungen belegten das Vorhandensein der invers tetragonalen Struktur ($I\bar{4}m2$) in vier der Proben (Mn_2RhSn, $Mn_{2.1}Rh_{0.9}Sn$, $Mn_{2.3}Rh_{0.7}Sn$, $Mn_{2.4}Rh_{0.6}Sn$) aus dieser Serie. Als interessant stellten sich Mn_2RhSn und $Mn_{2.1}Rh_{0.9}Sn$ heraus, da sie aus nur einer Phase vorzuliegen scheinen, wohingegen die anderen Verbindungen aus gemischten Phasen mit gleichzeitiger starken Fehlordnung bestehen. Letzteres wurde

durch ^{119}Sn-Mößbauer-Messungen bestätigt. Temperaturabhängige Mößbauerspektren weisen auf eine Koexistenz von Phasen unterschiedlicher magnetischer Ordnungstemperatur hin, wobei sich die relativen Anteile der jeweiligen Phasenanteile von Probe zu Probe unterscheiden. Die Phasen Mn_2RhSn und $Mn_{2.1}Rh_{0.9}Sn$ liegen in der invers tetragonalen Struktur vor und zeigen hartes, ferrimagnetisches Verhalten. Diese Eigenschaft ist eine Grundvoraussetzung für Verbindungen, die sich für STT eignen sollen.
Im abschließenden Anhang wurden die Fehlordnung und gelegentliche Mischphasen einer großen Auswahl von $Mn_{3-x}Fe_xGa$-Materialien mit $1 \leq x \leq 3$, dokumentiert.

3 List of publications

1. T. Gasi, V. Ksenofontov, J. Kiss, S. Chadov, A. K. Nayak, M. Nicklas, J. Winterlik, M. Schwall1, P. Klaer, P. Adler, and C. Felser
Iron-based Heusler compounds Fe_2YZ: Comparison with theoretical predictions of the crystal structure and magnetic properties
Phys. Rev. B, 87,064411, 2013

2. T. Gasi, A. K. Nayak, M. Nicklas and C. Felser
Structural and magnetic properties of the Heusler compound Fe_2MnGa
Journal of applied physics, 113, 17E301, 2013

3. J. Winterlik, S. Chadov, A. Gupta, V. Alijani, T. Gasi, K. Filsinger, B. Balke, G. H. Fecher, C. A. Jenkins, F. Casper, J. Kbler, G. Liu, L. Gao, S. S. P. Parkin and C. Felser
Design Scheme of New Tetragonal Heusler Compounds for Spin-Transfer Torque Applications and its Experimental Realization
Adv. Mater, 24, 6283–6287, 2012

4. C. Neetzel, T. Gasi, V. Ksenofontov, C. Felser, E. Ionescu, W. Ensinger
Electroless synthesis of lepidocrocite (γ-FeOOH) nanotubes in ion track etched polycarbonate templates
Nuclear Instruments and Methods in Physics Research B, 282, 96-99, 2012

5. Ch. Wang, L. Basit, Y. Khalavka, Y. Guo, F. Casper T. Gasi, V. Ksenofontov, B. Balke, G. H. Fecher, C. Sönnichsen, Y. K. Hwu, J. J. Lee, and C. Felser
Probing the Size Effect of Co_2FeGa-SiO2@C Nanocomposite Particles Prepared by a Chemical Approach

6. Ch. Wang, F. Casper, T. Gasi, V. Ksenofontov, B. Balke, G. H. Fecher, C. Felser, Y. Khalavka, C. Sönnichsen, Y. .K. Hwu, and J. J. Lee
Structural and magnetic properties of Fe_2CoGa Heusler nanoparticles
J. Phys. D:Appl. Phys. 46, 295001 (2010)

7. Ch. Wang, Y. Khalavka, F. Casper, T. Gasi, V. Ksenofontov, B. Balke, G. H. Fecher, C. Felser, C. Sönnichsen, Y. K. Hwu, and J. J. Lee
Effects of composition and silica supports on the structure and particle size of Co_2FeGa Heusler nanoparticles

submitted to Appl. Phys. Lett. D ,(2011)

8. V. Ksenofontov, G. Wortmann, A. I. Chumakov, T. Gasi, S. Medvedev, T. M. McQueen, R. J. Cava, and C. Felser
Density of phonon states in superconducting FeSe as a function of temperature and pressure
PHYSICAL. REVIEW. B, 81, 184510(2010)

9. S. Utech, Ch. Scherer, K. Krohne, L. Carrella, E. Rentschler, T. Gasi, V. Ksenofontov, C. Felser and M. Maskos
Magnetic polyorganosiloxane core-shell nanoparticles: Synthesis, characterization and magnetic fractionation
Journal of Magnetism and Magnetic Materials, 322:3519-3526, 2010

10. L. M. Schoop , V. Ksenofontov , T. Gasi, R. J. Cava , C. Felser
The Effect of Fe Doping on Superconductivity in ZrRuP
Solid state communications (2010), arXiv:1011.0848v1

4 Motivation for the study of the Heusler compounds synthesized for this thesis

4.1 Introduction

The Heusler compounds are intermetallic compounds with the stöchiometry 2:1:1 and the general formula X_2YZ. X and Y frequently represent a transition metal whereas Z is a main group element. This is a remarkable and fascinating class of modern magnetic materials from both, a fundamental as well as an application-oriented point of view. The interest on these compounds can be traced back to 1903 when Fritz Heusler discovered ferromagnetism in Cu_2MnAl even though none of its constituents is magnetic by itself [1, 2]. To clarify their crystal structure it took three decades and the bottom line was the well ordered $L2_1$ structure which determines the microscopic mechanism responsible for the appearance of magnetic moments. Not just ferromagnetism has been found but also antiferromagnetism and ferrimagnetism are familiar and comprehensively investigated like ferrimagnetic Mn_3Ga [3]. The large variety of physical properties which can be realized in Heusler-type materials is a consequence of their peculiar crystal structure and their great chemical flexibility. The basic cubic $L2_1$ crystal structure of X_2YZ phases (space group $Fm\overline{3}m$: space group no. 225) is composed of four interpenetrating fcc sublattices (Fig 4.1, a). It may be considered as a zinblende-like arrangement of Z and X atoms with the remaining X atoms in the tetrahedral and the Y atoms in the octahedral voids. This leads to a NaCl-type arrangement of the Y and Z atoms where each Y atom is surrounded by six Z atoms in the second coordination sphere, whereas the nearest neighbors of each Y atom are eight X atoms. On the other hand each X atom is surrounded by four Y and four Z atoms. However, cubic Heusler compounds are also found in the $CuHg_2Ti$-type structure ($Fm\overline{4}3m$: space group no. 216, X-type) [4]. In contrast to the regular Heusler structure where the X atoms fill only the tetrahedral voids and YZ build a NaCl-type arrangement, in the inverse Heusler structure X and Z build the rock salt lattice and the remaining X atoms and Y fill the tetrahedral voids (Fig. 4.1, b). This structure type is often observed if the atomic number of Y is higher than the atomic number of X ($Z(Y)>Z(X)$) [1]. If the constituting atoms have similar radii an anti site disordering may occur. Based on this have been found different structure types of Heusler compounds. The random distribution of X and the Y or the X and the Z atoms leads to the BiF_3 ($Fm\overline{3}m$: Space group no. 216, DO_3) disorder (not shown in this work). Additionally are shown in Fig. 4.1, two frequent types of disorder in Heusler compounds namely B2 and A2. An even distribution of Y and Z atoms leads to a CsCl-like structure known as B2-type disorder ($Pm\overline{3}m$: space group no. 221), whereas in the A2 type all lattice sites are randomly occupied by the constituting elements ($Im\overline{3}m$: space group no. 229) [1]. However, it is known that the antisite disordering in Heusler compounds mostly destroys the halfmetallic ferromagnetic behavior, on account of this the study of the local structure is of great interest [5]. As X-ray diffraction (XRD) techniques are frequently

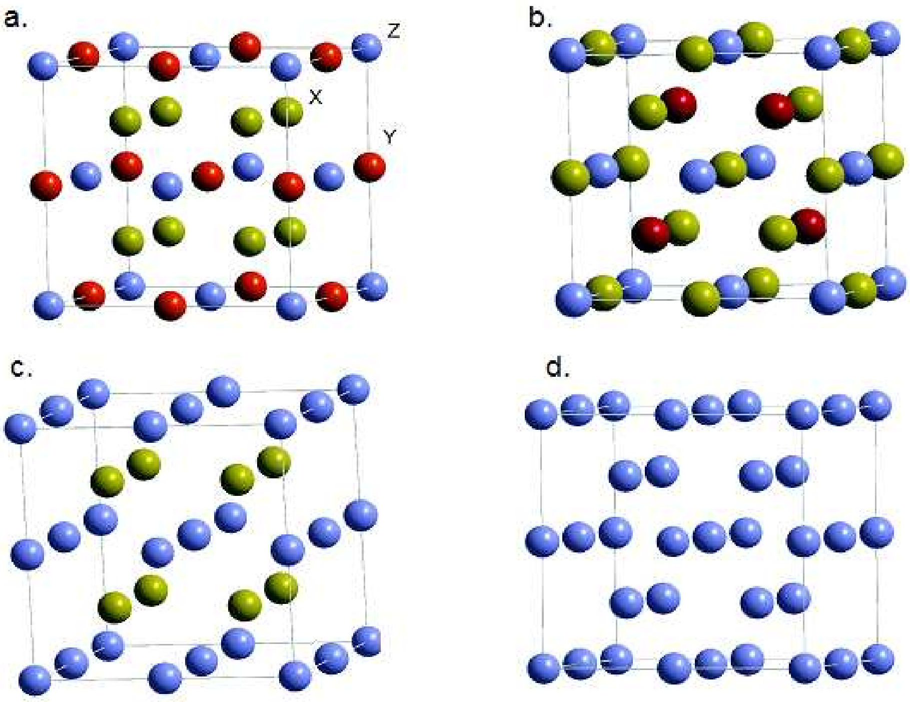

Figure 4.1: Different types of Heusler structures. Ordered Heusler with $L2_1$ structure, a) Inverse-Heusler, b) partially disordered-Heusler known as B2 type, c) and fully disordered Heusler known as A2 type, d).

insufficient for extracting the detailed atomic order in Heusler materials, additional experimental methods are required. Anomalous XRD and extended x-ray absorption fine structure (EXAFS) experiments are versatile techniques for this purpose [6], while x-ray magnetic circular dichroism (XMCD) studies give access to site-selective magnetic moments [7, 8]. In case of the present Fe- and Sn -based materials we have used ^{57}Fe and ^{119}Sn-Mössbauer spectroscopy as an informative laboratory-technique to characterize both the local atomic and magnetic order in our samples. An early contribution to the rationalization of the magnetic properties of Heusler compounds is the theoretical work by Kübler et al. on X_2MnZ-type compounds [9], which describes how large localized magnetic moments in the Mn sublattice are realized by an itinerant electronic system composed of hybridized Mn d - X d bands [9]. While Kübler et al. emphasized the importance of indirect Mn - Z- Mn interactions for the magnetic properties later work pointed out the leading character of the direct Mn- X interactions [10, 11]. The various magneto-responsive effects of Heusler compounds such as magnetic-field-induced shape memory/strain effects, magnetoresistance, and magnetocaloric effects [12, 13] promise a

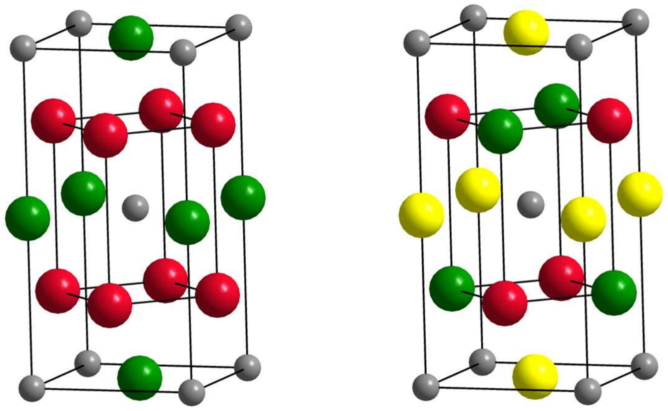

Mn_2FeGa
I4/mmm

MnFeMnGa
$I\bar{4}m2$

Figure 4.2: Tetragonal distortion of heusler compounds derived from the regular (left) and inverse heusler structures (right), respectively [25].

wide range of applications. For instance, ferromagnetic martensites are experimentally found in different half-Heusler alloys such as NiMnGa, NiFeGa, CoNiGa and related materials [14]. All these effects occur in temperature ranges which are convenient for device operation. The great current interest in Heusler compounds arises, however, at least partly from the observation of half-metallic ferromagnetism in several of these materials [15, 4] as half-metallic ferromagnets have a great potential in the emerging field of spintronic applications [16, 17]. During the last decades Co_2 based Heusler compounds have been extensively studied in the context of spintronics due to the predicted full-spin polarization of the electronic density at the Fermi-energy, which leads to ferromagnetic half-metalls [18]. For instance, Wurmehl et al. have reported an exceptionally high magnetic moment of $6\,\mu_B$ and a Curie temperature T_C of 1100 K for half-metallic Co_2FeSi [19] [20].
Not only the cubic but also tetragonally distorted Heusler compounds like Mn_3Ga [21] have found considerable attention as they are an attractive source of candidates for spin-transfer-torque (STT) applications [22]. The spin-transfer effect has been predicted in 1998 by Slonczewski [23] and Berger [24], where the magnetization orientations in magnetic multilayers (MML) were manipulated by a spin polarized current instead of an external field. A tetragonal distortion was found in the class of Mn_2YZ Heulser compounds, which crystallize in the inverse Heusler structure [2, 25, 26, 27]. Two different types of structures are known for the tetragonal cell as displayed in Figure 4.2. The regular tetragonal cell (Fig. 4.2, a) on the left (I4/mmm: space group no. 139) is derived from the well ordered full-Heusler with an elongation along the c-axis, whereas the inverse tetragonal cell (Fig. 4.2, b) on the right ($I\bar{4}m2$: space group no. 119) is derived from the inverse Heusler structure, namely the $CuHg_2Ti$-type.

In contrast to the tetragonal structure where Mn atoms occupy just one lattice site

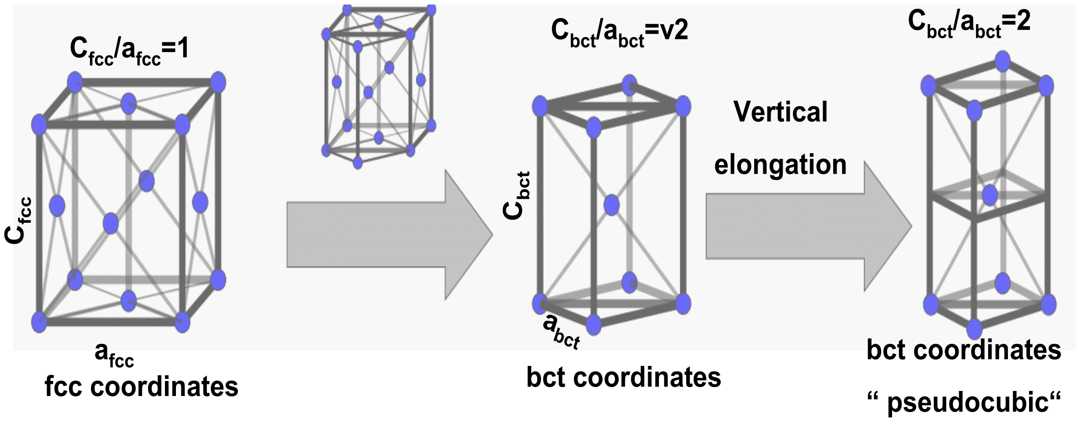

Figure 4.3: Transition from the ideal cubic structure to a pseudocubic structure by doubling the cell-edge.

with octahedral symmetry, in the inverse tetragonal structure, Mn atoms occupy two different lattice sites, one with tetrahedral and one with octahedral symmetry. A tetragonal structure known as pseudocubic structure will be in this thesis often mentioned. The transition from a cubic structure to a pseudocubic structure is illustrated schematically in Fig. 4.3. Currently, tetragonal Heusler compounds are in the main focus on realizing the STT phenomenon for non-volatile-memory and logic devices [28]. In contrast to the conventional field-induced switching the STT phenomenon offers the advantage of the significant downscaling of the device dimensions compatible for the memory and logic devices with reduced power consumption. The materials suitable as a switching element in spin-transfer torque devices need to satisfy the following conditions. The primary challenge is to minimize the switching current and the switching time and maximize or maintain the thermal stability, respectively. For non-volatility of the stored information the thermal stability factor E/k_BT needs to be more than 40 [29], where E is given by Eq. 4.1:

$$E = \frac{M_s H_K V}{2} \tag{4.1}$$

here, E is the energy barrier that separates the two magnetization directions, M_s is the saturation magnetization, H_K the anisotropy field, V the cell volume, k_B the Boltzmann constant and T the temperature. However, to E is proportional the intrinsic threshold current, which is given by Eq. 4.2:

$$I = \alpha \frac{\gamma e}{\mu_B g} M_s H_K V = 2\alpha \frac{\gamma e}{\mu_B g} E \tag{4.2}$$

where α is the magnetic damping constant, γ the gyromagnetic ratio, e the elementary charge, μ_B the Bohr magneton and g a function of the spin polarization of the tunnel junction and the angle between the magnetization of the free and reference layers [29, 28]. The switching time is given by Eq. 4.3:

$$t_{sw} = \frac{M_s V}{\gamma} \tag{4.3}$$

Therefore, low magnetic damping and high spin polarization leads to a minimization of the switching current, whereas high magnetic damping and high anisotropy field leads to a minimization of the switching time. According to this, materials with high spin polarization and Curie temperature T_C, but low saturation magnetization M_s and magnetic damping are needed to be used for STT applications. Additionally, the lattice match with the insulator (MgO) is very important. It is important to emphasize that the key for the realization of high density non-volatile memory and logic devices with low current and high thermal stability is the perpendicular anisotropy of the magnetic materials. Recent experiments have observed that Mn_3Ga thin films exhibit giant perpendicular magnetic anisotropy (PMA), high spin polarization and also a low Gilbert damping [28], and therefore, it is perfectly applicable for the implementation in spin valves or magnetic tunnel junctions [30]. The advantage of Heusler compounds for the STT-based memory and logic-devices is their predictable electronic structure and the tunability of the magnetic properties. The large tetragonal distortion of the cubic Heuslers is caused by electronic instabilities like the Jahn-Teller distortion, which is also meanwhile fairly good predictable by band structure calculations based on the van Hove singularity [4]. This is a saddle point at the Fermi energy (where the band changes its curvature), which leads to a high density of states (DOS), accordingly at the Fermi energy. A high DOS at the Fermi energy is exactly the sign of the instability of the electrons, which first undergo a magnetic transition and then a structural transition. In half-metallic cubic phases one typically has nearly 100% of spin polarization, however, despite one spin-channel shows a semiconducting band gap at Fermi energy, the other spin-chanel shows this high DOS peak due to the van Hove Singularity. This can be relaxed then only by distorting the structure. Conclusive, we remark that the promising systems for STT-applications are those based on Mn_2, and following this we have tried to synthesize and optimize Heusler alloys.

Based on the interest for materials potential for spintronics especially STT-applications, we have emphasized in this work the following Heusler compounds, namely Fe_2YZ, Fe_2MnGa, Mn_2FeGa and $Mn_{3-x}Rh_xSn$.

4.2 Synthesis and characterization

4.2.1 Experimental Details

Fe_2YZ (Y=Co, Ni, Cu; Z=Al, Ga, Ge) compounds were synthesized by repeated arc-melting or ball milling of stoichiometric amounts of pure metals in an argon atmosphere under 10^{-4} mbar pressure, whereas the series $Mn_{3-x}Fe_xGa$ and $Mn_{3-x}Rh_xSn$ were synthesized just by arc-melting. To ensure an oxygen-free atmosphere, titanium was used as getter material. The samples were three times melted and turned over. The weight loss after the whole process was less than 0.5 %. Additionally, they were annealed in evacuated glass quartz tubes. After annealing they were quenched in a mixture of ice and water. In addition it has been attempted to synthesize Fe_2ZnAl in a similar way, however, the Heusler phase could not be stabilized. The crystal structures of the products at room temperature were investigated by means of powder XRD using excitation by monochromatic Cu-$K_{\alpha 1}$ (λ_{Cu}=1.540598 Å) and Mo-$K_{\alpha 1,2}$ radiation $\lambda_{\mathrm{Mo,K}\alpha 1}$=0.7093165 Å) in θ-θ scanning mode. Disc-shaped samples were used for Fe_2CoGe, Fe_2NiGa, Fe_2CuGa, Fe_2CuAl and $Mn_{3-x}Fe_xGa$ whereas the rest of the compounds, which could be pestled were measured as powder. The XRD patterns were fitted by the Full Prof software package [31], in case of Mo-$K_{\alpha 1,2}$ radiation the α_1/α_2 splitting of the radiation was taken into account. The magnetic moments were measured by SQUID magnetometry (superconducting quantum interference device, Quantum Design MPMS-XL5) within the temperature range 5–800 K . ^{57}Fe-Mössbauer measurements were performed in transmission, backscattering and CEMS (conversion electron Mössbauer spectroscopy) modes using a constant acceleration spectrometer with a ^{57}Co (Rh-matrix) source with $h\nu = 14.4\,\mathrm{keV}$. The backscattering spectra were recorded with the miniaturized Mössbauer spectrometer MIMOS [32]. Information about bulk properties was obtained from the transmission or backscattering spectra (information depth d $\sim$ 10^4 Å), while the CEM spectra (d $\sim$ 10^3 Å) are more surface sensitive. ^{119}Sn-Mössbauer measurements were performed only in transmission mode. To obtain the reliable distribution of hyperfine parameters the data were fitted using the Voigt-based fitting (VBF) model within the Recoil software package [33]. The homogeneity and stoichiometry of the samples was controlled by a scanning electron microscope (SEM, Jeol JSM-6400) equipped with an energy-dispersive X-ray (EDX) spectroscopy detection system (EUMEX EDX). The measurements were carried out at 3×10^{-6} mbar pressure. The acceleration voltage of 20 kV with an observation angle of 35° was used. For the correction of the quantitative data the so-called ZAF method was applied which relies on atomic number (Z), absorption (A) and fluorescence (F) effects. The images were acquired via the Digital Image Processing System (DIPS) and the quantitative chemical analysis was performed with the WINEDS 4.0 program.

4.3 Heusler Compounds as Half-metallic Ferromagnets

Half-metallic ferromagnets (HMF‘s) are materials, where the majority spin density of states is metallic and the minority-spin density of states is semiconducting with an energy gap which leads to 100% spin polarization at the Fermi level (Fig. 4.4) [34, 35]. This concept was proposed by de Groot for the first time in the case of the intermetallic half-Heusler alloy NiMnSb [36] and also has been predicted by Kübler [37] in Co_2MnSn. The discovery of these materials marks the origin of high interest towards Heusler compounds as potential candidates for applications in the field of spintronics, for magneto-optical effects [38] and GMR applications [39]. Since then this class of materials has been extensively explored. These particular characteristics makes them important for spin injection devices in spintronics [34, 35]. A wide range of materials was often theoretically predicted and additionally successfully synthesized. Many published full-Heusler compounds contain Co. These materials were first synthesized by Ziebeck and Webster [40]. Hence, to date new Heusler compounds which can be used as half-metallic ferromagnets are still a hot topic, and to this date there is a constant search for novel half-metallic antiferromagnets, also known as fully-compensated ferrimagnets. In magnetic storage devices these materials do not give rise to stray flux, which leads to a considerably lower energy consumption [41] compared to traditional antiferromagnets. The simple fabrication method of the Co_2YZ materials and their high-Curie temperature which is well above room temperature makes them very attractive from the perspective of industrial applications [34].

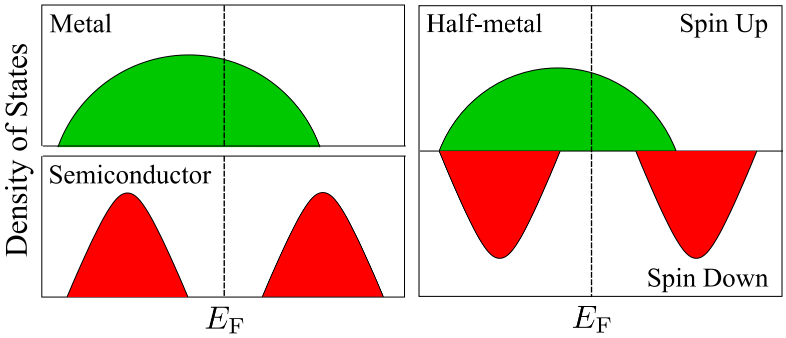

Figure 4.4: Schematic representation of the density of states for a half-metal compared to a metal and a semiconductor [42] .

In addition to the half-metallic Co_2YZ compounds, there are several other quaternary and ternary Heusler compounds which show interesting properties. As an example, another attractive class of materials is provided by the series $Co_2Cr_{1-x}Fe_xAl$ with a special emphasis on $Co_2Cr_{0.6}Fe_{0.4}Al$, which was shown to possess a relatively high magnetoresistance up to 30% in a low magnetic field of 0.1 T [2] together with the $Co_2Mn_{1-x}Fe_xSi$ series [2]. The latter is even more interesting because the $L2_1$ order was obtained in the whole range of concentrations x. However, it is already known that disordering effects destroy the half-metallic properties in many of the materials [37, 38, 2, 39]. One of the important criteria of Heusler compounds which indicate a half-metallic character is that the total magnetic moment follows a simple electron-counting rule based on the Slater-Pauling behavior [43, 44].

4.3.1 The Slater-Pauling Rule

Slater [45] and Pauling [46] discovered that the magnetic moment (m) of the 3d elements and their binary alloys can be estimated by the mean number of valence electrons (n_V) per atom. Fig. 4.5 displays the two distinct regions of the magnetism of the materials, where iron is located at the borderline. The right region of the Slater-Pauling curve represents the area of itinerant magnetism and high valence electron concentrations ($\mathrm{n}_V \geq 8$) corresponding to systems with closed packed structures (*fcc* and *hcp*, respectively). The left region in Fig. 4.5 represents the materials with localized moments and low valence electron concentrations ($\mathrm{n}_V \leq 8$), which have mostly *bcc* and *bcc*-related structures. The Heusler compounds are attributed to the latter region, so we will focus on this part of the Slater-Pauling curve later.

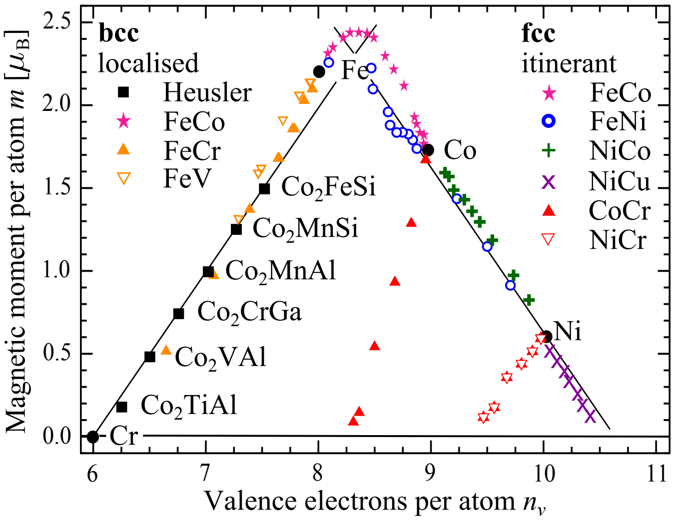

Figure 4.5: Slater-Pauling curve for 3d transition metals and their alloys [42].

The magnetic moment for the itinerant magnetism is given by the formula:

$$m = (2n\uparrow - n_V)\ \mu_B = (2(n_d\uparrow + n_{sp}\uparrow) - n_V)\ \mu_B \tag{4.4}$$

Here m denotes the magnetic moment given in multiples of Bohr magnetons μ_B per atom, where $n\uparrow$ denotes the total number of electrons in the majority states, and $\mathrm{n}_d\uparrow$ is the number of spin up electrons in d orbitals. The symbol $\mathrm{n}_{sp}\uparrow$ is the number of spin up electrons in *sp* orbitals, and n_V refers to the number of the valence electrons ($\mathrm{n}_V = n\uparrow + \mathrm{n}\downarrow$). For the late transition metals revealing ferromagnetism the majority d-bands are completely filled, hence $\mathrm{n}_d\uparrow = 5$. As the sp bands-according to the Slater-Pauling rule contribute approximately $n_{sp} = 2n_{sp}\uparrow = 0.6$ electrons, one obtains the following empirical equation which describes the total magnetic moment for itinerant magnets:

$$m = (10.6 - n_V)\mu_B \tag{4.5}$$

For instance, for Ni we have n_V=10 and therefore the magnetic moment of nickel is approximately $0.6\,\mu_B$. In comparison, the magnetic moment per atom for the localized magnetism is approximately described by the formula:

$$m = (n_V - 6)\mu_B \tag{4.6}$$

Eq. 4.6 originates from two simple equations, which will be given in the following. The sum of the electrons in the minority and majority bands, which generates the total amount of the valence electrons can be simply written as:

$$n_V = n\uparrow + n\downarrow \tag{4.7}$$

whereas the magnetic moment is given by the following equation:

$$m = (n\uparrow - n\downarrow)\mu_B \tag{4.8}$$

The combination of Eq. 4.7 and Eq. 4.8 gives the general equation:

$$m = (n_V - 2n\downarrow)\mu_B \tag{4.9}$$

Since, Kübler has found that the amount of the electrons in the d-minority band is approximately $n\downarrow$=3 [47], we obtain the aforementioned formula Eq. 4.6.

In case of a half-metallic ferromagnet n is exactly 3 due to the gap in the minority DOS. For half-Heusler compounds with 3 atoms in the unit cell, the Slater-Pauling rule is formulated as

$$M = (n_V - 18)\ \mu_B \tag{4.10}$$

where M and n_V are the magnetic moment and the number of the valence electrons per formula unit, respectively. For full-Heusler compounds with four atoms in the unit cell, the total magnetic moment thus amounts to:

$$m = (n_V - 24)\ \mu_B \tag{4.11}$$

For higher valence electron concentrations ($n_V \geq 30$), which are expected for Heusler compounds containing elements with nearly filled *d*-shells (for e.g. Ni or Cu), an itinerant Slater-Pauling behavior occurs, where the magnetic moment is determined by a fixed number of the majority spin states and by the filling of the minority spin channels [43, 44, 48]. The following approximation is valid for these Heusler compounds:

$$M_{\text{it}} \approx (34 - n_V)\ \mu_B \tag{4.12}$$

4.4 ^{57} Fe and ^{119} Sn Mössbauer Spectroscopy

4.4.1 Mössbauer Spectroscopy-introduction

A remarkable tool for describing oxidation states and chemical bonding, the symmetry of the surrounding atoms or atom groups and hyperfine magnetic splitting (Zeeman effect) is Mössbauer spectroscopy. It is a method, which has been used in this thesis for determining the local ordering in intermetallic compounds containing Fe or Sn, the magnetic moments and often the magnetization orientation in disc samples. Mössbauer spectroscopy is one of the most sensitive techniques in terms of energy resolution, due to the high energy and extremely narrow line widths of gamma rays [32]. Certainly, there are drawbacks of this method, for example, the use of gamma radiation, which is dangerous for our organism, and the requirement of recoil free absorption and emission of gamma rays called Mössbauer effect, which is feasible just in the solid state and not in gaseous or liquid solutions. The Mössbauer effect was first observed by R. L. Mössbauer in 1958 during his PhD work in experiments with ^{191}Ir and hence he became a Nobel Prize winner in 1961. Since this brilliant discovery the Mössbauer effect has been observed for many different isotopes from more than 40 elements but of course not every isotope found is suitable for investigations due to the short lifetime of the corresponding source. However, Mössbauer spectroscopy has attracted a wide attention as a subject of numerous successful investigations in solid state physics as well as in chemistry [49]. The most common isotope used in Mössbauer studies is ^{57}Fe, which has a relative abundance of 2.2 % in natural iron and also ^{119}Sn, which will be discussed in more detail in this thesis. In the Fig. 4.6 is given the set up of the Mössbauer experiment, which has been used for the samples discussed in this thesis.

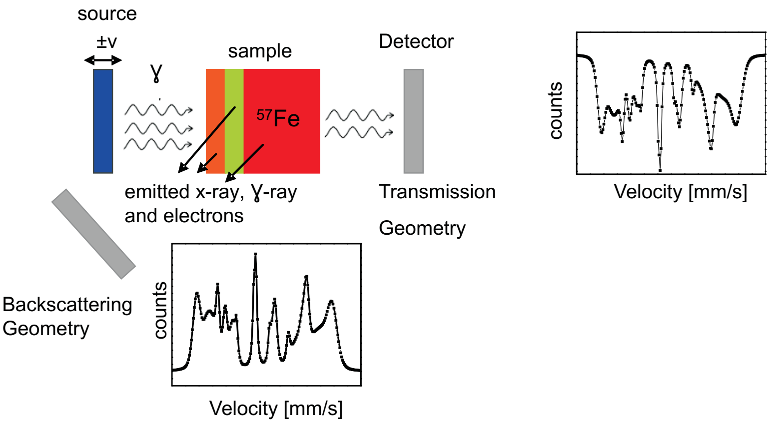

Figure 4.6: A Mössbauer experiment may be set up in transmission geometry and backscattering geometry [50].

4.4.2 Mössbauer Effect

The recoilless absorption and emission of gamma rays from a certain Mössbauer atom bound in a solid, which corresponds to a transition between the ground and the excited state of the nucleus is called Mössbauer effect [51]. It is known that the recoil energy E_R is described by the formula $E_R=E_0/2M^*c^2$, and for ^{57}Fe ($E_0=E_e$-E_g=14.4 keV). E_R is calculated to be 1.95^*10^{-3} eV. The energy of the absorbed γ-rays from a free atom is due to E_R shifted to $E_\gamma=E_0+E_R$ and the emission energy is also shifted to $E_\gamma=E_0-E_R$, respectively. Due to the high E_R, which is subjected to isolated atoms or molecules in gaseous and liquid states and which is six orders of magnitude larger than the natural line width, the nuclear resonance absorption is impossible. When the Mössbauer atom is embedded in a solid, then M stands now for the mass of the whole solid or crystallite, respectively. The mass of the crystallite compared to the mass of the single atom is many orders of magnitude larger and because of that the most of the recoil energy is converted into mean lattice vibrational energy and E_R turns out to be negligible [32]. The vibrational energy is quantized, vibrational excitations are known as phonons. The Mössbauer effect corresponds to the recoil free processes (where no phonons are involved). Its probability is described by the Lamb Mössbauer factor (f). The Lamb Mössbauer factor increases with decreasing temperature and transition energy E_γ or with increasing Debye Temperature. The Debye Temperature is a measure for the strength of the coupling between the Mössbauer atom and the lattice. Usually it takes high values in metallic compounds whereas it it is small in organic systems. A very important element for Mössbauer spectroscopy is the source of γ rays. A radiation source for ^{57}Fe-Mössbauer spectroscopy is ^{57}Co. Figure 4.7 represents the decay scheme of the ^{57}Co-source which is embedded in matrices like Rh: ^{57}Co is an isotope with a half life of 271 days. By electron capture (EC) from the K-shell ^{57}Co decays with 99.84% efficiency to the level with the nuclear spin quantum number $I = 5/2$ which corresponds to the energy 136.32 keV, which then decays again to the first excited state $I = 3/2$ with energy 14.4 keV. The $I = 3/2$ state has a mean life time of about 1.43^*10^{-7} s and then decays

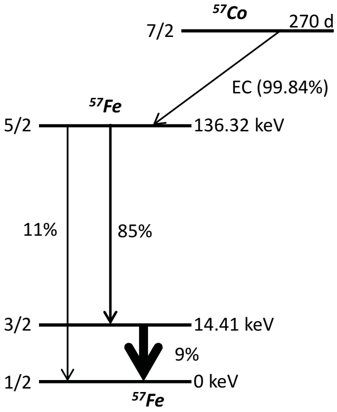

Figure 4.7: Decay scheme of ^{57}Co-source [32].

with a 9% probability by emission of a 14.4 keV γ-quantum into the $I = 1/2$ ground state. The corresponding natural line width of the Mössbauer transition is 0.097 mm/s.

4.4.3 Spectral line shape

A nuclear or electronic excited state with a certain mean lifetime τ is always associated with an energy range ΔE (this means that the energy level is spread over an energy range ΔE), which according to the Heisenberg uncertainty relation is defined by the expression:

$$\Delta E \; \tau \geq \frac{h}{2\pi} \tag{4.13}$$

Here, h equates Plank's constant.

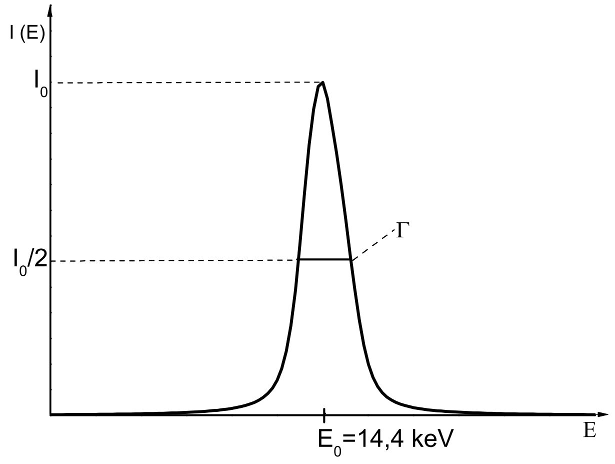

Figure 4.8: Intensity I(E) as a function of transition energy E [32].

The intensity distribution I (E) associated with the transition from an excited state into the ground state shown in Fig. 4.8 leads to a spectral line with a Lorentzian form around the maximum at energy E_0 with a certain line width ΔE=Γ given by Eq. 4.13. For Mössbauer spectroscopy experiments suitable lifetimes of nuclear excited states are in the range 10^{-6} s to 10^{-11} s. ^{57}Fe has the mean time lifetime τ=$t_{1/2}$/$\ln_2$=1.43*10^{-7} s; and therefore Γ=0.11 mm/s [32].

4.4.4 Hyperfine Interactions

The perturbation of the nuclear energy levels of a Mössbauer atom due to electric or magnetic fields is called hyperfine interaction. The essential interactions, which are described in the following, are given as hyperfine parameters isomer shift ($\boldsymbol{IS}$), the quadrupole splitting ($\boldsymbol{QS}$) and the magnetic splitting ($\boldsymbol{H}_{hf}$).

4.4.5 Isomer shift (IS)

The isomer shift corresponds to an electrostatic Coulomb interaction between the nuclear charge spread over a finite volume and the electrons inside the nuclear region (see, Fig. 4.9). It provides information about the electronic charge density at the Mössbauer atom.

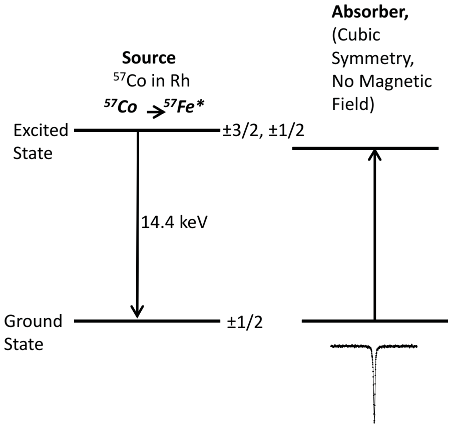

Figure 4.9: Electric monopole interaction between the nuclear charge and electrons at the nucleus shifts nuclear energy levels [50].

The expression for the isomer shift of ^{57}Fe considering that the atomic nuclei have a spherical symmetry with radius R and constant nuclear charge density $p_n(R)=3Ze/4\pi R^3$ is expressed by the following formula [32]:

$$\delta = \frac{4}{5}\pi Z e^2 \frac{\delta R}{R} R^2 \left\{ \left|\psi(0)\right|_A^2 - \left|\psi(0)\right|_S^2 \right\}, (4.14)$$

Where $\frac{\delta R}{R}$ is the fractional change in the nuclear charge radius between the ground and the excited state; and $|\psi(0)|_S^2$ and $|\psi(0)|_A^2$ are the total s-electron densities at the source and absorber nuclei, respectively [49]. The isomer shift is directly influenced by electrons from s-orbitals with non-zero probability at the nucleus and indirectly due to the shielding of s-electrons by the d and f-orbitals. The $\frac{\delta R}{R}$ ratio may be positive or negative. For $\frac{\delta R}{R}$ positive, a positive isomer shift indicates an increase of the electron density at the nucleus on going from the source to the absorber; when $\frac{\delta R}{R}$ is negative, a positive isomer shift implies that the electron density at the absorber nuclei is lower than at the source nuclei [32]. For ^{57}Fe, the ratio $\frac{\delta R}{R}$ is negative implying that an increasing electron density at the nucleus results in a more negative value of δ. Unlike the case of Fe, Sn shows the opposite.

4.4.6 Quadrupole splitting (QS)

The quadrupole splitting reflects the deviation of the nuclear charge distribution from spherical symmetry if J>1/2, and it bears information about the symmetry of the electron charge distribution in the neighborhood of the Mössbauer atom. It is known from quantum physics, that the nuclear states are characterized by a nuclear spin quantum number I and the nuclear magnetic spin quantum number m_I=(I,I-1,,-1). Only nuclear states with I>1/2 have a non-zero electric quadrupole moment and thus can interact with an inhomogeneous electric field [49]. The nuclear states can be split into sublevels $|I, \pm\ m_I\rangle$ by the electric quadrupole interaction, where the degeneracy of ± m_I levels is retained. In case of ^{57}Fe the excited state with the spin quantum number I=3/2 is split into two sublevels with m_I=±3/2 and m_I=±1/2 (see, Fig. 4.10). The energy difference between these two sublevels is defined by:

$$\Delta E_q = E_q(\pm 3/2) - E_q(\pm 1/2) = eQV_{zz}/2 \tag{4.15}$$

where e is the electron charge, Q is the nuclear quadrupole moment and Vzz is the z-component of the electric field gradient tensor. In Eq. 4.15 it is assumed that the EFG is axially symmetric. Fig. 4.10 displays the two line pattern ("quadrupole doublet") in a Mössbauer spectrum resulting from the quadrupole splitting in case of ^{57}Fe. The magnitude of the quadrupole splitting QS, is just the difference in velocity of the two lines: QS=$| v_2 - v_1 |$. Basically, to the total EFG two sources can contribute namely the lattice contribution and the valence electron contribution. Lattice contribution means the influence of charges on distant ions which surround the Mössbauer atom in non-cubic symmetry, while the anisotropic electron distribution in the valence shell of the Mössbauer atom describes the valence electron contribution [32].

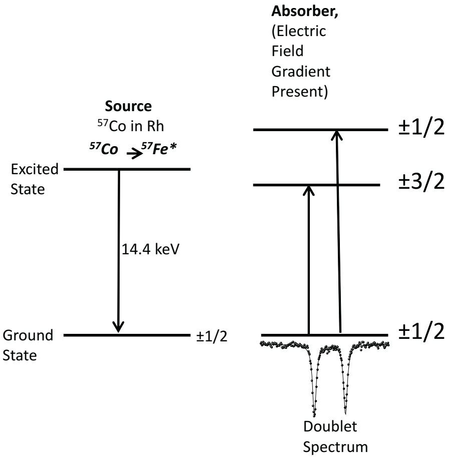

Figure 4.10: Quadrupole splitting in ^{57}Fe with I=3/2 in the excited state and I=1/2 in the ground state [50].

4.4.7 Magnetic hyperfine splitting (H_{hf})

The magnetic splitting defines the interaction between the nuclear magnetic dipole moment associated with $I > 0$ with a magnetic Field H at the nucleus. The latter is the sum of an external magnetic field and the hyperfine field H_{hf}. The parameter H_{hf} is related to the magnetic properties of the partially filled Fe 3d shells for ^{57}Fe atoms or to the induced magnetic fields at the diamagnetic ^{119}Sn nucleus. The magnetic splitting is also known as nuclear Zeeman effect. It can be described by the Hamiltonian operator:

$$H = -\mu H = -g\mu_N IH \tag{4.16}$$

Where μ is the nuclear magnetic moment, μ_N is the nuclear magneton, g is the nuclear g-factor and I is the nuclear spin. The resulting eigenvalues of the energy can be written as:

$$E_{mI} = -g\mu_N Hm_I \tag{4.17}$$

Figure. 4.11 shows the splitting of the nuclear states and the resulting six allowed transitions for ^{57}Fe, where the $I = 3/2$ level is split into four substates and the ground state with $I = 1/2$ into two substates. Each level with nuclear spin I according to Eq. 4.17 is split into $2I+1$ non-degenerate, equally spaced substates. Considering the selection rule $\Delta m_I = 0, \pm 1$ one observes six allowed transitions in case of ^{57}Fe leading to hyperfine sextets in magnetically ordered materials.

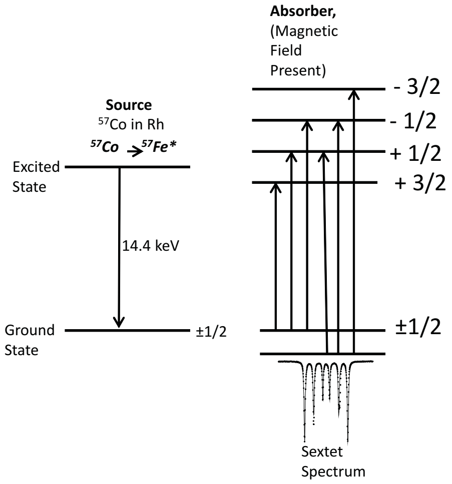

Figure 4.11: Magnetic dipole splitting (nuclear Zeeman effect) in ^{57}Fe [50].

4.4.8 Conversion Electron Microscopy (CEMS)

In contrast to the bulk-sensitive transmission mode, the probing depth of conversion electron Mössbauer Spectroscopy (CEMS) is $\leq 100\,nm$. It is a surface sensitive method which one can use for obtaining information about chemical and magnetic properties of the surface. Similar to the transmission geometry, in the CEMS mode the Mössbauer

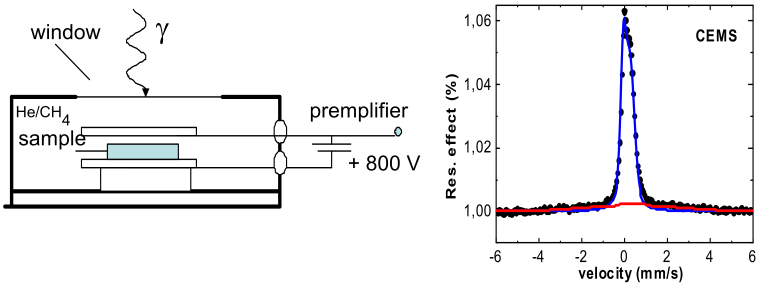

Figure 4.12: Scheme for CEMS and and a CEMS spectrum [32].

atom is excited by gamma rays with the source energy 14.4 keV in case of ^{57}Fe. The deexcitation of the Mössbauer atom into the ground state may be achieved by emitting gamma rays, or by exciting electrons from the electronic shell. The deexcitation by the creation of such so-called conversion electrons is much more probable than the radiative decay (by a factor of 9). The Mössbauer spectrum in CEMS is registered using conversion electrons originating from the atomic shells K, L, M. To register conversion electrons the sample is placed in a chamber filled with He/ 5%CH_4 as a counting gas, which effectively absorbs low-energy conversion electrons by ionization. The ionization electrons are collected by the positively charged wire, and gas amplification occurs in the normal way [32]. This method is used routinely as a powerful tool for characterization of thin films. Therefore CEMS is a promising technique for the non-destructive investigation of materials.

4.4.9 ^{119}Sn Mössbauer Spectroscopy

This chapter is devoted to the comparison of ^{57}Fe and ^{119}Sn- Mössbauer spectroscopy and to a deeper insight into ^{119}Sn-Mössbauer Spectroscopy. While the radiation source of ^{57}Fe is the isotope ^{57}Co, for ^{119}Sn the parent nuclide is ^{119m}Sn, which can be produced by a neutron irradiation of ^{118}Sn in a high flux reactor [49]. The following scheme shows the decay of the isotope to the excited state with the desired energy of 23.87 keV used for the Mössbauer experiment. As shown in Fig. 4.13, the energy level of 89.54 keV is a metastable state and an isomeric transition occurs which leads directly to the energy level at 23.84 keV with $I = 3/2$ and a mean life time of $1.85{*}10^{-8}$ sec. The latter level corresponds to a calculated natural linewidth of 0.31 mm/s for the I=3/2 → I=1/2 Mössbauer transition. One of the most favorable sources for ^{119}Sn-Mössbauer Spectroscopy is $Ca^{119m}SnO_3$. Due to the cubic symmetry of the matrix, it shows a narrow emission line width. To decrease a background radiation of 25.04 keV that is emitted from the source, a thin filter of Pd foil (100 μm) is used between the source and the detector for the measurement in transmission geometry. Since in CEMS the conversion

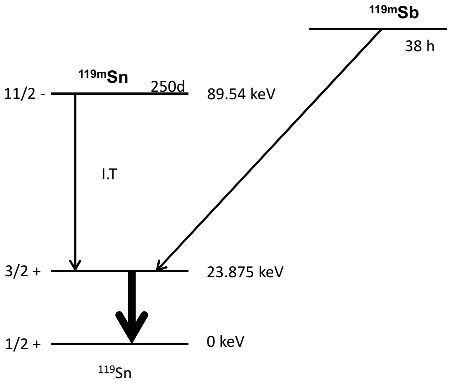

Figure 4.13: Decay scheme of ^{119m}Sn-source [49].

electrons with a probing depth of 100 nm are detected, it is not necessary to use a Pd filter for absorbing the x-rays in this case. The chemical and physical information is also extracted by the hyperfine interactions, i.e isomer shift, quadrupole splitting and magnetic splitting. In contrast to iron, tin is diamagnetic and therefore there are no inherent magnetic fields at the ^{119}Sn nuclei. However, if Sn is alloyed in ferromagnetic compounds a magnetic field can be induced, which leads to six magnetic sublevels like in the case of ^{57}Fe, the ground state of I=1/2 is split into two sublevels and the excited state I=3/2 is split into four sublevels.

4.5 Shape memory alloys (SMA)

Shape memory alloys refer to a class of materials which exhibit particular properties like pseudoelasticity and shape memory effect. Pseudoelasticity means a reversible response to an applied stress during the phase transformation (between the austenite and martenisic phases of a crystal). The martensite phase occurs at low temperatures and is the soft phase (easily deformed phase) in contrast to the austenite phase, which occurs at higher temperatures and is assigned to a stablest or strongest phase, respectively [52]. For the first time in 1932 the Swedish physicist Arne Ölander observed this phenomena during his work in experiments with Au and Cd[15] and reported this finding as thermoelastic transformation of martensite. From this resulted later the shape memory effect which was then reported by Kudjamov [53] and Chang and Road [54]. A simple sketch is given in the Figure 4.14 for an understanding macroscopically the shape memory effect. By cooling the sample below M_S, the transformation occurs and the martensite phase spreads over the whole volumen like in Fig. 4.14, (b) shown, building at the same time twins, which can keep the original shape. After the mechanical deformation, this material can relax the produced internal stresses by the movement of twin boundaries instead of the normal slip motion by dislocations as shown in Fig. 4.14(d) [52]. This effect has been found also in Heusler compounds. The first studied Heusler compound based on the shape memory effect is Ni_2MnGa. Further examples are Mn_2NiAl, Mn_2NiGa, Mn_2NiIn

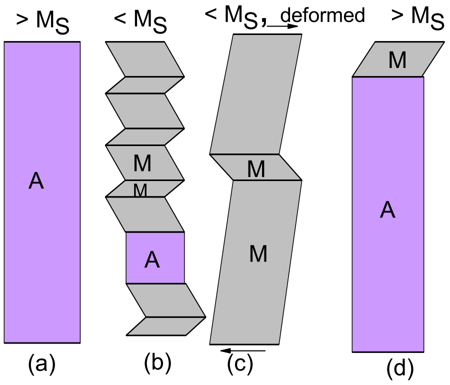

Figure 4.14: A sketch about the martensitic transformation in the shape memory effect [52].

and Mn_2NiSn [55, 56, 57]. Shape memory alloys are of scientific and commercial interest because of their applications in medicine, thermostats, robotics, hydraulic fittings (for Airplanes) [55].

5 Iron-based Heusler compounds Fe_2YZ: Comparison with theoretical predictions of the crystal structure and magnetic properties

5.1 Abstract

The present work reports on the new soft ferromagnetic Heusler phases Fe_2NiGe, Fe_2CuGa, and Fe_2CuAl, which in previous theoretical studies have been predicted to exist in a tetragonal Heusler structure. Together with the known phases Fe_2CoGe and Fe_2NiGa these materials have been synthesized and characterized by powder XRD, ^{57}Fe Mössbauer spectroscopy, SQUID, and EDX measurements. In particular Mössbauer spectroscopy was used to monitor the degree of local atomic order/disorder and to estimate magnetic moments at the Fe sites from the hyperfine fields. It is shown that in contrast to the previous predictions all the materials except Fe_2NiGa basically adopt the inverse cubic Heusler (X-) structure with differing degrees of disorder. The experimental data are compared with results from *ab-inito* electronic structure calculations on LDA level incorporating the effects of atomic disorder by using the coherent potential approximation (CPA). A good agreement between calculated and experimental magnetic moments is found for the cubic inverse Heusler phases. Model calculations on various atomic configurations demonstrate that antisite disorder tends to enhance the stability of the X-structure.

5.2 Introduction

Magnetic Heusler compounds with the general formula X_2YZ where X and Y are transition metal elements and Z is a main group element are one of the most fascinating classes of modern magnetic materials, from both a fundamental as well as an application-oriented point of view [4, 20]. The large variety of physical properties which can be realized in Heusler-type materials is a consequence of their peculiar crystal structure and their great chemical flexibility. The basic cubic $L2_1$ crystal structure of X_2YZ phases (space group $Fm\bar{3}m$) is composed of four interpenetrating fcc sublattices (see Fig.5.1). It may be considered as a zincblende-like arrangement of Z and X atoms with the remaining X atoms in the tetrahedral and the Y atoms in the octahedral voids. This leads to a NaCl-type arrangement of the Y and Z atoms where each Y atom is surrounded by six Z atoms in the second coordination sphere, whereas the nearest neighbors of each Y atom are eight X atoms. On the other hand, each X atom is surrounded by four Y and four Z atoms. An early contribution to the rationalization of the magnetic properties of Heusler compounds is the theoretical work by Kübler et al. on X_2MnZ-type compounds [9], which describes how large localized magnetic moments in the Mn sublattice are realized by an itinerant electronic system composed of hybridized Mn d-X d bands [9]. Kübler et al. emphasized the importance of indirect Mn-Z-Mn interactions for the magnetic properties. The various magneto-responsive effects of Heusler compounds such as magnetic-field-induced shape memory/strain effects, magnetoresistance, and magnetocaloric effects [12, 13] promise a wide range of applications. For instance, ferromagnetic martensites are experimentally found in different half-Heusler alloys such as NiMnGa, NiFeGa, CoNiGa and related materials [14]. All these effects occur in temperature ranges which are convenient for device operation. The great current interest in Heusler compounds arises, however, at least partly from the observation of half-metallic ferromagnetism in several of these materials [15, 4] as half-metallic ferromagnets have a great potential in the emerging field of spintronic applications [58, 17]. Since Wurmehl *et al.* have reported an exceptionally high magnetic moment of 6 μ_B and a Curie temperature T_C of 1100 K for the half-metallic Co_2FeSi [19], the interest for Heusler compounds has highly increased, and the Co-based Heusler compounds have been studied extensively [20]. The combination of Co and Fe is particularly good for obtaining high T_C's.

Not only the cubic but also tetragonally distorted Heusler compounds –like Mn_3Ga [25]– have found considerable attention as they are attractive candidates for spin-transfer-torque applications [22]. In this respect it is remarkable that in course of a recent theoretical study on potentially new Heusler compounds [59, 60] several iron-based Fe_2YZ materials with a regular tetragonal Heusler structure have been predicted [60]. Actually it was found for these phases that the inverse cubic Heusler structure (X-structure, space group $F\overline{4}3m$)), should be more stable than the regular one (see Fig.5.1). The X-structure may be formally written as (FeY)FeZ where the Fe atoms occupy the octahedral and tetrahedral voids of the zincblende-type lattice to equal parts. The inverse Fe_2YZ structures in some of the materials are, however, predicted to be unstable towards a tetragonal distortion which tends to maximize the bonding interactions [60]. Motivated by the potential importance of tetragonal iron-based Heusler compounds for applications, especially as potential rare-earth free hard magnets, and by the fundamental question of electronic instabilities in Heusler compounds this work reports the synthesis and characterization of the new compounds Fe_2NiGe, Fe_2CuGa, and Fe_2CuAl, the existence of which has been predicted in Ref [60]. In addition the properties of the known phases Fe_2CoGe [61] and Fe_2NiGa [62] have been investigated in more detail. Usually first-principle electronic structure calculations are based on a perfect crystal. However, Heusler compounds are ternary or even quaternary compounds which are widely amenable to chemical disorder. This can be the reason for discrepancies between theoretical predictions and experimental results. This aspect turns out to be of crucial importance also for the present Fe_2YZ materials and therefore will be discussed in detail. As X-ray diffraction (XRD) techniques are frequently insufficient for extracting the detailed atomic order in Heusler materials additional experimental methods are required. Anomalous XRD and extended x-ray absorption fine structure (EXAFS) experiments are versatile techniques for this purpose [6], while x-ray magnetic circular dichroism (XMCD) studies give access to site-selective magnetic moments [63, 8]. In case of the present iron-based materials we have used ^{57}Fe-Mössbauer spectroscopy as a simple laboratory-technique to characterize both the local atomic and magnetic order in our samples. The additional theoretical analysis based on first-principles electronic structure calculations treating the chemical disorder by means of the CPA method [64, 65](coherent potential approximation), shows that the cubic structure of Fe_2YZ Heusler materials becomes indeed more stable when assuming certain degree of anti-site disorder as suggested by the experiments.

5.3 Synthesis and characterization

5.3.1 Experimental details

Fe_2YZ (Y=Co, Ni, Cu; Z=Al, Ga, Ge) compounds were synthesized by repeated arc-melting or ball milling of stoichiometric amounts of pure metals in an argon atmosphere under 10^{-4} mbar pressure. To ensure an oxygen-free atmosphere, titanium was used as getter material. The samples were three times melted and turned over. The weight loss after the whole process was less than 0.5%. Additionally, they were annealed in evacuated glass quartz tubes for two weeks at 673 K and then in order to test the influence of the annealing temperature on the degree of disorder some of them were further annealed at 1173 K. After annealing they were quenched in a mixture of ice and water. In addition it has been attempted to synthesize Fe_2ZnAl in a similar way, however, the Heusler phase could not be stabilized. The crystal structures of the products at room temperature were investigated by means of powder XRD using excitation by monochromatic Cu-$K_{\alpha1}$ ($\lambda_{\mathrm{Cu,K}\alpha1}$=1.540598 Å) or Mo-$K_{\alpha1,2}$ radiation ($\lambda_{\mathrm{Mo,K}\alpha1}$=0.7093165 Å) in θ-θ scanning mode. Disc-shaped samples were used for Fe_2CoGe, Fe_2NiGa, Fe_2CuGa and Fe_2CuAl. Since Fe_2NiGe samples were better produced by ball-milling, they were measured as powders. The XRD patterns were fitted by the FullProf software package [31], in case of Mo-$K_{\alpha1,2}$ radiation the α_1/α_2 splitting of the radiation was taken into account. The magnetization was measured by different SQUID magnetometers (MPMS-XL5 and MPMS SQUID VSM, Quantum Design) within the temperature range 1.8 to 950 K. ^{57}Fe-Mössbauer measurements were performed in transmission, backscattering and CEMS (conversion electron Mössbauer spectroscopy) modes using a constant acceleration spectrometer with a ^{57}Co (Rh-matrix) source with $h\nu = 14.4$ keV. The backscattering spectra were recorded with the miniaturized Mössbauer spectrometer MIMOS [32]. Information about bulk properties was obtained from the transmission or backscattering spectra (information depth d $\sim$ 10 μm), while the CEM spectra (d $\sim$ 100 nm) are more surface sensitive. To obtain the reliable distribution of hyperfine parameters the data were fitted using the Voigt-based fitting (VBF) model within the Recoil software package [33].

The homogeneity and stoichiometry of the samples was controlled by a scanning electron microscope (SEM, Jeol JSM-6400) equipped with an energy-dispersive X-ray (EDX) spectroscopy detection system (EUMEX EDX). The measurements were carried out at 3×10^{-6} mbar pressure. The acceleration voltage of 20 kV with inspection angle of 35° was used. For the correction of the quantitative data the so-called ZAF method was applied, which relies on atomic number (Z), and on absorption (A) and fluorescence (F) effects. The images were acquired via the Digital Image Processing System (DIPS) and the quantitative chemical analysis was performed with the WINEDS 4.0 program. According to the EDX analysis the Fe_2YZ alloys show a rather good homogeneity in

Compound	Fe	Y	Z
Fe_2CoGe	50.43	25.36	24.22
Fe_2CuGa	49.77	25.94	24.30
Fe_2NiGa	50.78	24.65	24.57
Fe_2NiGe	47.48	27.55	24.97
Fe_2CuAl	48.32	26.57	25.11

Table 5.1: Relative concentration given as percentages of the samples from the Fe_2YZ alloys according to an EDX analysis.

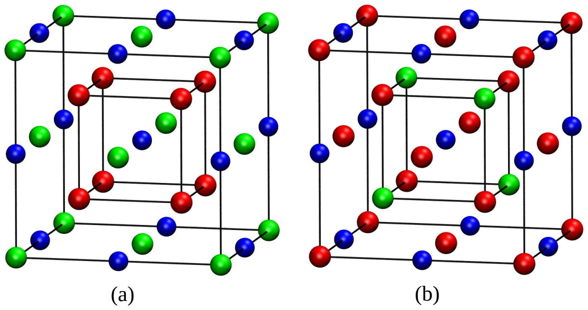

Figure 5.1: Conventional unit cell of the cubic Heusler (a) and inverse Heusler (b) X_2YZ compounds. The X, Y, and Z atom types (where X=Fe for the materials studied in this paper) are shown with red, green, and blue spheres, respectively.

their composition, except Fe_2NiGe (see Tab. 5.1).

5.3.2 XRD structural characterization

Typically well-ordered Heusler compounds crystallize in a cubic crystal structure, either in the regular $L2_1$ (space group $Fm\overline{3}m$)) or in the inverse X-(space group $F\overline{4}3m$)) structure. For both structure types the XRD patterns exhibit additional (111) and (200) fcc superstructure reflections. In many cases the intensity ratio I_{111}/I_{200} allows to distinguish them from each other. Based on plane-wave pseudopotential calculations, some of the present materials have been predicted to crystallize in a tetragonally distorted regular Heusler structure (space group $P4_2/ncm$) [60]). The XRD patterns of the Fe_2YZ materials annealed at 673 K are shown in Fig. 5.3 and in Fig. 5.2. As is seen from the typical distances between the (220), (400), and (422) reflections (note that the Miller indices correspond to an fcc lattice) all materials crystallize in a cubic structure. Additional weak reflections in the patterns of Fe_2NiGe, Fe_2CuGa, and Fe_2CuAl point to the presence of a small fraction of impurity phases. However, none of the patterns indicates any features like peak splittings which could be attributed to a tetragonal distortion predicted for Fe_2NiGe, Fe_2CuGa, and Fe_2CuAl [60]. The lattice parameters obtained from Rietveld refinement of the data by assuming the inverse cubic Heusler structure (space group $F\overline{4}3m$)) are given in Table 5.2.

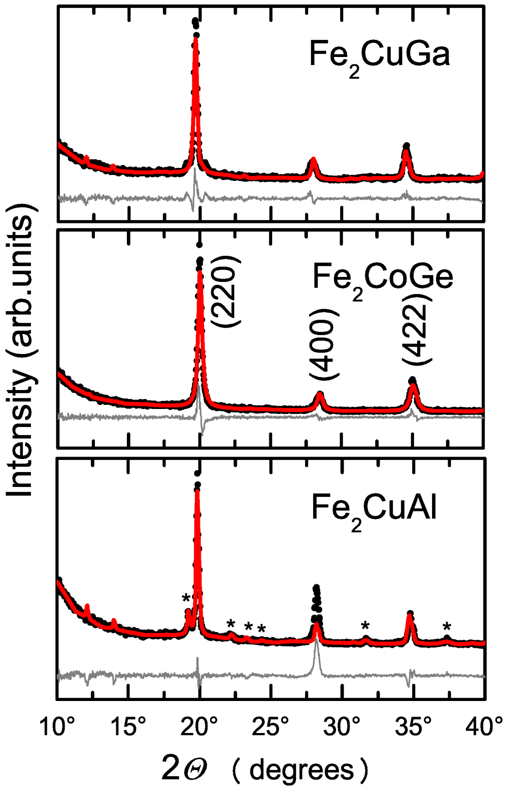

Figure 5.2: XRD of Fe_2CuGa, Fe_2CoGe and Fe_2CuAl alloys annealed at 673 K. The diffraction patterns are compared to the results of Rietveld refinements. Diffraction peaks marked with stars are assigned to an impurity phase Cu_xAl_y [66] (space group $Fm\overline{3}m$ with a = 3.63 Å). The measurements were carried out at RT using Mo-K_α radiation.

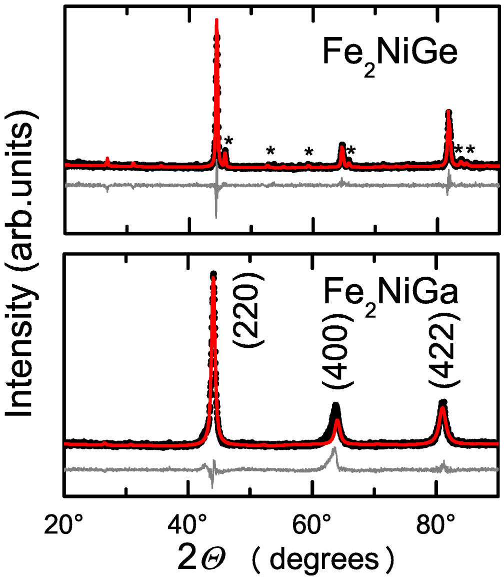

Figure 5.3: XRD of Fe_2NiGe and Fe_2NiGa alloys annealed at 673 K. The diffraction patterns are compared to the results of Rietveld refinements. Diffraction peaks marked with stars are assigned to an impurity phase Fe_xGe [67] (space group $P6_3/mmc$ with a = 3.97 Å and c=5.05 Å). The measurements were carried out at RT using Cu-K_α radiation.

The fcc superstructure reflections are not discernible in any of the XRD patterns. Two reasons have to be considered for that. First, the samples may be disordered according to the $A2$ type (with all lattice sites randomly occupied by the constituting elements). This results in a bcc-type ($Pm\overline{3}m$) diffraction pattern, where no superstructure reflections appear. Secondly, in all compounds except Fe_2CuAl the constituting elements are entirely from the 4^{th} row of the periodic table, which results in similar scattering factors. This leads to a virtual extinction of the (111) and (200) reflections, or at least, to very low intensities, if the standard laboratory sources with Cu-K_α or Mo-K_α radiation are used. In fact for a well-ordered sample of Fe_2CoGe very weak superstructure reflections have been observed [61]. Their detection requires, however, an improved signal-to-noise ratio of the XRD patterns and thus considerably longer measurement times. For studying the influence of the annealing temperature on the sample quality, in addition to the samples annealed at 673 K, the XRD patterns of samples annealed at 1173 K have been also recorded. In case of Fe_2NiGa and Fe_2CuAl sample decomposition was observed (XRD patterns not shown), the XRD patterns of the other samples (Fig. 5.4) revealed only minor changes. The phase purity of Fe_2NiGe appears to be slightly improved by annealing at higher temperature, but the Mössbauer spectra still revealed an impurity signal. Therefore, if not explicitly stated otherwise, we will focus in the rest of the paper on the samples annealed at 673 K.

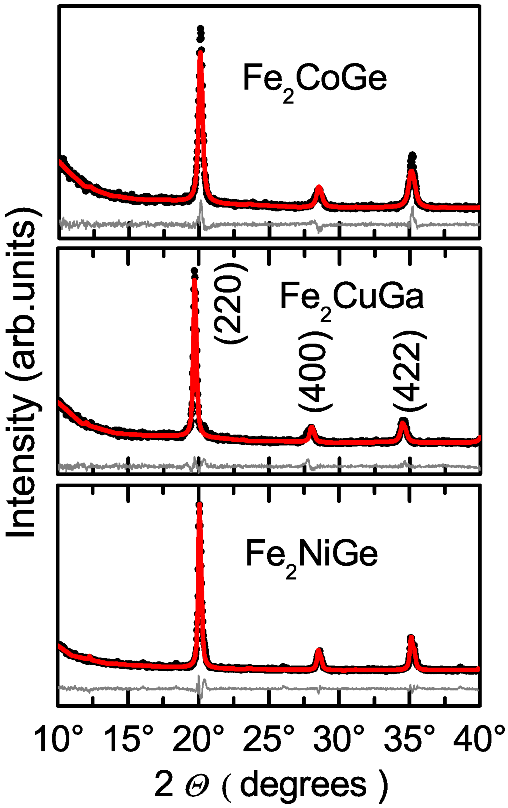

Figure 5.4: XRD of Fe_2CoGe, Fe_2CuGa and Fe_2NiGe alloys annealed at 1173 K. The diffraction patterns are compared to the results of Rietveld refinements.

Compound	a (Å)	a (Å)
Fe_2CoGe	5.78	5.76
Fe_2CuGa	5.86	5.86
Fe_2NiGa	5.81	-$^{a)}$
Fe_2NiGe	5.76	5.76
Fe_2CuAl	5.83	-$^{a)}$

Table 5.2: The lattice parameters of Fe_2YZ were determined at room temperature and are given for an fcc lattice. Left are shown the lattice parameters of Fe_2YZ annealed at 673 K and right at 1173 K , and $^{a)}$ marks those cases which have involved decomposition of the sample.

In summary, the XRD patterns verify that the synthesized Fe_2YZ materials all crystallize in cubic Heusler-type structures. It is, however, impossible to derive the exact atomic order from the XRD data. More information about the atomic and magnetic order is obtained by ^{57}Fe-Mössbauer spectroscopy, which is a local probe technique. The results obtained with this technique will be presented below.

5.3.3 Characterization of magnetic properties

As displayed in Fig. 5.5, all compounds exhibit soft ferromagnetism. It is noted, that the magnetic behavior slightly depends on the annealing temperature. The isothermic magnetization curves at 5 K are essentially saturated in an induction field of 5 T. The magnetic moments at 5 K and 5 T together with the magnetic ordering temperatures T_C are summarized in Table 5.3. The latter have been derived from the drop in the temperature dependent magnetization curves measured at 0.1 T or 1 T (Fig. 5.6). Additional anomalies in the T-dependence of Fe_2NiGe and Fe_2CuAl point to the ordering of a minority phase in these samples. The valence electron concentration (VEC) per formula unit and magnetic moments obtained from electronic structure calculations are included in Table 5.3, too. All materials considered in this paper contain 29 or 30 valence electrons per formula unit. The magnetic moment of the 673 K-annealed sample of Fe_2CoGe is somewhat larger than the value of 5.1 μ_B reported earlier [61], while that of the 1173 K-sample is in better agreement with the published data. The experimental magnetic moments of Fe_2CoGe are quite close to the value of 5 μ_B expected from the generalized Slater-Pauling (SP) rule, which predicts the magnetic moment m per formula unit given in μ_B for half-metallic X_2YZ phases as m = VEC - 24 with VEC = 29 for Fe_2CoGe. This suggests that Fe_2CoGe could be a half-metallic ferromagnet, however, the spin polarization appears to be not complete [61](see also Section III). The magnetic

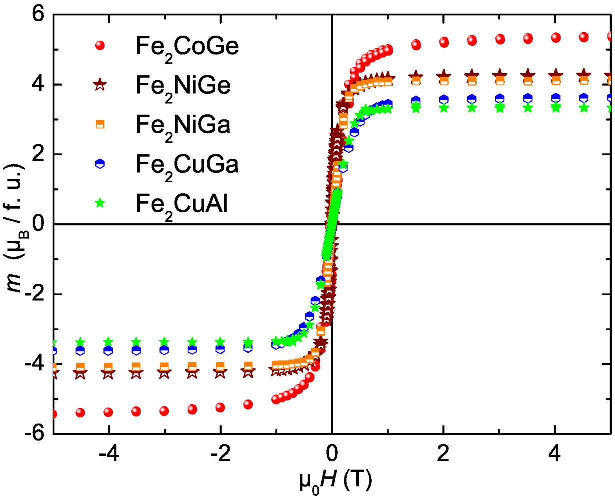

Figure 5.5: Field-dependent magnetization m per formula unit of Fe_2YZ compounds annealed at 673 K and measured at 5 K.

Table 5.3: Summary of the magnetic properties (magnetic moments m, Curie temperatures T_c) of Fe_2YZ alloys obtained from experiment (SQUID and Mössbauer measurements, left part of the Table) and from *ab-initio* electronic structure calculations (right part of the Table, indicated with m_{th}). The total magnetic moments m per formula unit are obtained from magnetization measurements at 5 K, whereas the magnetic moments at the Fe sites are derived from room temperature Mössbauer spectra.

compound	VEC a)	$m^{b)}$ (μ_B)	$T_c^{b)}$ (μ_B)	$m^{c)}$ (μ_B)	m [FeA]$^{d)}$ (μ_B)	m[FeB]$^{d)}$ (μ_B)	$m_{\mathrm{th}}^{e)}$ (μ_B)	$m_{\mathrm{th}}^{e)}$[FeA] (μ_B)	$m_{\mathrm{th}}^{e)}$[FeB] (μ_B)
Fe_2CoGe	29	5.40	925 [61]	5.0	2.6	1.6	5.15	2.68	1.51
Fe_2NiGe	30	4.29	750	4.46	2.5	1.7	4.47	2.53	1.67
Fe_2NiGa	29	4.20	845	-	-	$2.05^{f)}$	4.81	2.64	1.82
Fe_2CuGa	30	3.60	798	3.40	2.5	1.7 $2.1^{g)}$	4.04	2.34	1.78
Fe_2CuAl	30	3.30	875	-	2.2	1.7	3.80	2.23	1.67

a) VEC is the valence electron concentration
b) measurement for the 673 K-annealed sample
c) measured for the sample annealed at 1173 K
d) estimated from the Mössbauer hyperfine fields of the 673 K-annealed sample at RT
e) theoretical moments for the fully ordered inverse cubic Heusler phase calculated for the experimental lattice parameters
f) derived from average H_{hf} value of the Mössbauer hyperfine pattern
g) derived from the average H_{hf} value of the broad component in the Mössbauer hyperfine pattern

moments of all the other materials do not follow the generalized SP rule. The magnetic ordering temperatures are quite high ($T_C > 700$ K) which makes the materials suitable for potential applications. A detailed comparison of experimental magnetic moments from both bulk magnetization and Mössbauer measurements with theoretical moments will be compiled in Section III.

5.3.4 Mössbauer measurements

The potential of Mössbauer spectroscopy for studying the degree of atomic order in iron-containing Heusler compounds has been demonstrated previously for the series $Co_{2-x}Fe_{1-x}Si$ [5] and $Co_2Mn_{1-x}Fe_xAl$ [68]. The former compounds crystallize in well-ordered cubic Heusler structures which evolve from the regular $L2_1$ structure for Co_2FeSi to the inverse X structure for Fe_2CoSi. The Mössbauer spectra of $Co_{2-x}Fe_{1-x}Si$ ($0.1 \leq x \leq 0.9$) are composed of two sharp six-line patterns with magnetic hyperfine fields H_{hf} in the range 320–340 kOe (sextet A) and 185–195 kOe (sextet B), respectively. The successive replacement of Co by Fe atoms in $Co_{2-x}Fe_xSi$ leads to a corresponding increase in the area fraction of sextet B. From the above mentioned series it can be concluded unambiguously that the A sextet corresponds to Fe sites with (8-4x) Co and 4x Fe atoms in the first coordination sphere, the B sextet corresponds to Fe sites with four Fe(A) and four non-magnetic Si neighbors, independent of x. The variation in the H_{hf} values of the two sites due to the substitution is quite small. In the $L2_1$ structure of Co_2FeSi the Fe(A) atoms have O_h symmetry with eight Co nearest neighbors and six Si atoms in the second

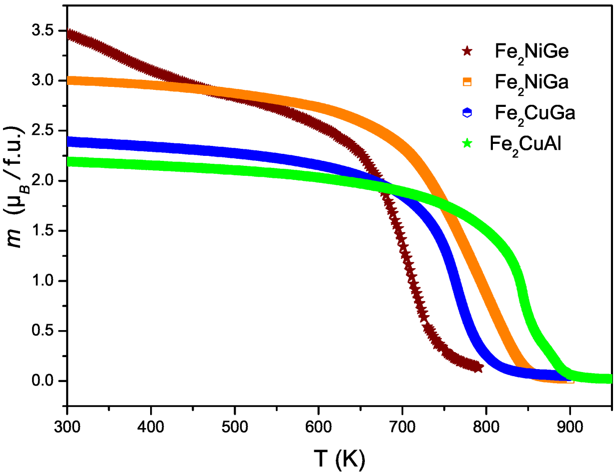

Figure 5.6: Temperature-dependent magnetization m per formula unit of Fe_2YZ alloys annealed at 673 K. The measurements were performed in the range of 300–900 K at 0.1 T (for Fe_2CuAl, Fe_2CuGa, Fe_2NiGa) and 1 T (for Fe_2NiGe) induction fields.

coordination shell. In the final member compound Fe_2CoSi all atoms have T_d symmetry and the Fe(A) sites are surrounded by four Fe(B) and four Co atoms. On the other hand a B2-type disorder in the series $Co_2Mn_{1-x}Fe_xAl$ gives rise to a strongly broadened hyperfine pattern which reflects the superposition of Fe sites in different coordination environments. A detailed analysis of these spectra has been given in Refs. [5, 69]. The Mössbauer spectra demonstrating the hyperfine field distribution at RT for the present Fe_2YZ materials annealed at 673 K are shown in Fig. 5.7 and Fig. 5.8. The transmission and backscattering spectra in Fig. 5.7 are representative for the bulk materials and will be discussed in detail below. The more surface sensitive conversion electron Mössbauer (CEM) spectra (Fig. 5.8) reveal additional line broadening and the details seen in the backscattering or transmission spectra are lost. This points to enhanced disorder in the surface layers. Also Mössbauer spectra of the samples annealed at 1173 K were recorded. As there was no improvement of atomic order in any of the samples and according to XRD even partial decomposition occurred for Fe_2NiGa and Fe_2CuAl, we restrict the discussion to the 673 K-annealed samples. All data were fitted with a Voigt profile model which yields a distribution of hyperfine fields. Actually this approximates the superposition of local coordination environments as has been exemplified in more detail in Ref [68].

The values of the Mössbauer parameters of Fe_2YZ obtained from the data evaluation for bulk samples are summarized in Table 5.4. All spectra can be described by two or three hyperfine sextets which show that the corresponding materials are magnetically ordered at room temperature. The detailed spectral shapes differ, however, which suggests a varying degree of disorder within the series of compounds. The Mössbauer spectra and H_{hf} values of Fe_2CoGe are close to those of $Co_{2-x}Fe_{1+x}Si$ [5] with two well-defined sextets. Thus, the sextet with higher H_{hf} is assigned to Fe(A) sites and the second sextet

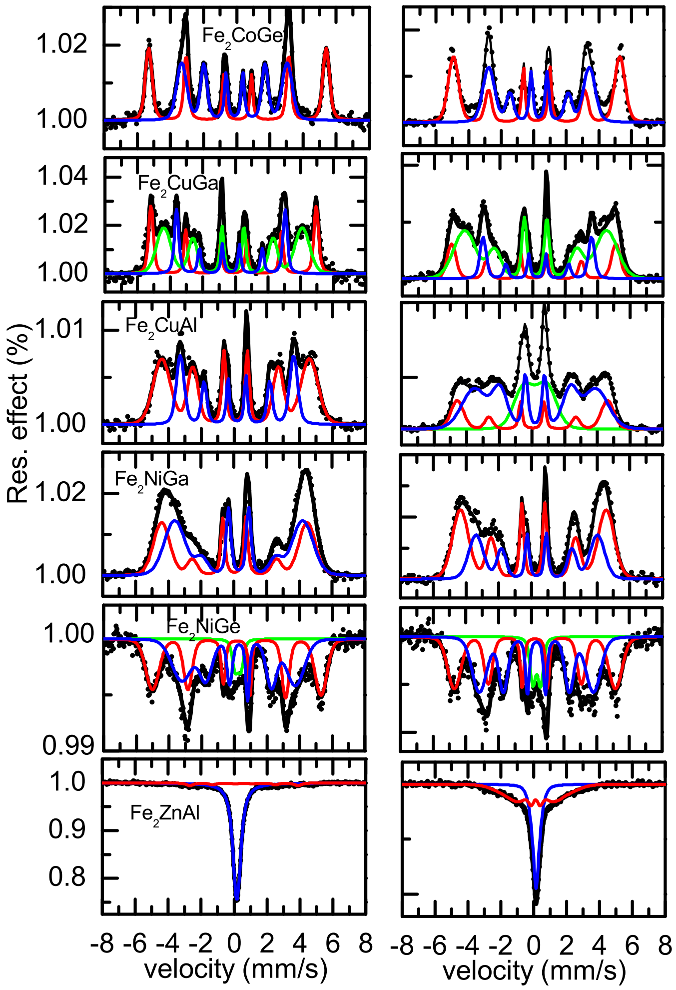

Figure 5.7: Mössbauer spectra of the Fe_2YZ samples annealed at 673 K (left) and at 1173 K (right). The spectra of Fe_2NiGe and Fe_2ZnAl are a transmission spectra, the others are backscattering spectra. The experimental points are shown as black dots, fitted by the black solid line (total signal). The total signal is decomposed into two (or three) distinct contributions. The outer one (red) with large H_{hf} corresponds to Fe(A), the inner one (blue) with smaller H_{hf} to Fe(B) as discussed in the text.

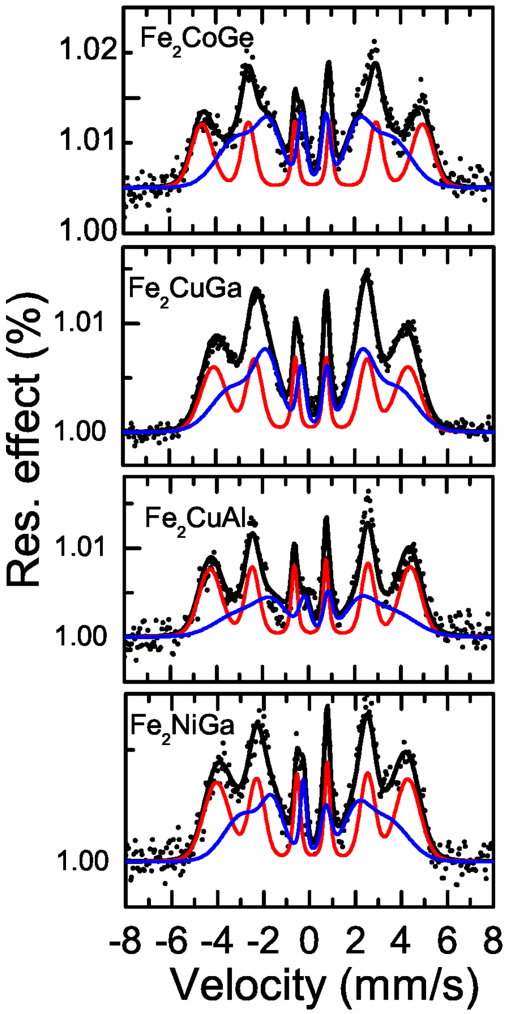

Figure 5.8: Conversion Electron Mössbauer spectra of Fe_2YZ samples annealed at 673 K and measured at RT. The experimental points are shown as black dots, fitted by the black solid line (total signal). The total signal is decomposed into two distinct contributions (red and blue, respectively), each corresponding to a certain environment of the Fe atoms.

Table 5.4: Mössbauer parameters at room temperature of Fe_2YZ samples annealed at 673 K. H_{hf} denotes the hyperfine field, IS the isomer shift, and A the relative area fraction. The maximum errors in H_{hf},A, and IS were ± 4 kOe, ± 3%, and ± 0.02 mm/s, respectively.

	$T_{\mathrm{anneal}} = 673$ K		
sample	H_{hf} (kOe)	A (%)	IS (mm/s)
Fe_2CoGe	332	48	0.05
	197	52	-0.14
Fe_2CuGa	314	28	-0.11
	264	49	-0.15
	207	22	-0.27
Fe_2NiGa	275	44	0.04
	242	56	0.30
Fe_2NiGe	320	44	0.15
	216	51	0.27
Fe_2CuAl	279	67	0.10
	214	33	0.18

with lower H_{hf} value to the Fe(B) sites. The intensity ratio of the two sextets is approximately 1:1. Since the two Fe atoms in inverse Heusler Fe_2YZ phases adopt two different lattice sites, as explained above, these data evidence that Fe_2CoGe like Fe_2CoSi crystallizes in the inverse Heusler (X) structure. Mössbauer spectra not only give information about the atomic distribution over the crystallographic sites but also allow an estimation of the ordered magnetic moments for Fe atoms at the A and B sites, respectively. In cubic or nearly cubic compounds the internal magnetic hyperfine field is determined by the Fermi contact term, which arises from the polarization of the s-electron density at the nucleus. It has been shown that H_{hf} scales linearly with the magnetic moments determined from neutron or magnetization studies [70]. Taking a slope of 125 kOe/μ_B for Fe germanides from Ref. [70] one roughly estimates the magnetic moments as $\sim 2.6\ \mu_B$ and $\sim 1.6\ \mu_B$ for Fe(A) and Fe(B) atoms in Fe_2CoGe, respectively. Considering the total magnetic moment of 5.4 μ_B from the magnetization studies (at 5 K) the remaining Co moment must be about 1.1 μ_B in case of ferromagnetic ordering. These estimates are in fair agreement with the calculated moments of 2.7 μ_B and 1.4 μ_B for the Fe sites and 0.9 μ_B for the Co sites reported in Ref. [61]. As for all the present materials the Curie temperatures are above 700 K the estimates of the moments from the room temperature Mössbauer spectra can be used for comparison with theoretical results. These data are included in Table III. Quite similar spectra are observed for Fe_2NiGe. Accordingly, also Fe_2NiGe essentially crystallizes in the inverse Heusler structure but line broadening for both subspectra and the small deviation from the ideal intensity ratio of 1:1 indicate some disorder. In case of Fe_2NiGe, from the H_{hf} values (see Table 5.4) one estimates the magnetic moments as 2.5 μ_B and 1.7 μ_B for the Fe(A) and Fe(B) atoms, respectively. The sum of the moments nearly corresponds to the total magnetic moment of 4.3 μ_B

for Fe_2NiGe obtained from magnetometry, which suggests that the Ni sites do not contribute much to the magnetic ordering. It is noted, however, that the present material is not completely single-phase. The Mössbauer spectrum reveals a 6% contribution of a paramagnetic quadrupole doublet ($IS = 0.23$ mm/s, $\Delta E_\mathrm{Q} = 0.37$ mm/s). In agreement with the clues from the XRD patterns this signal is assigned to an Fe_xGe_y impurity as the magnetic behavior of this system is known to depend strongly on the Fe-Ge ratio[70].

In contrast to Fe_2CoGe and Fe_2NiGe the Mössbauer spectrum of Fe_2NiGa reveals enhanced disorder. The two subspectra are no longer resolved and the spectra were modeled by a superposition of two broad sextets the average H_hf values of which are only slightly different. Hence, the distinction between well defined A and B sites is not meaningful. The disorder in Fe_2NiGa leads to a pronounced distribution of hyperfine fields and of the corresponding magnetic moments over various sites with differing local coordination environment. The nearly structureless spectra may point towards an A2-type disorder where alloying occurs between all sites. The average H_hf of 255 kOe roughly corresponds to an ordered moment of 2 μ_B per Fe or 4 μ_B per formula unit which is close to the total moment of about 4.2 μ_B. The considerable disorder in Fe_2NiGa is also suggested by the XRD pattern which reveals a pronounced broadening of the (400) and (422) reflections. Additional information about the orientation of the magnetic moments can be derived from the intensities of the Fe_2NiGa spectrum. As it is well known [71] for ^{57}Fe, in case of no or small quadrupole interaction only 6 lines of the 8 possible transitions in a magnetic field are observed with the intensity ratio $3 : Z : 1 : 1 : Z : 3$. The Z value is characteristic for the relative intensity of the $\pm 12 \longrightarrow \pm 12$ transitions and depends on the angle θ between the propagation vector of the γ-radiation and the direction of H_hf: $0 \leq Z \leq 4$. For a random orientation (powder) and thin absorbers $Z = 2$, whereas Z = 4 for $\theta = 90°$ and Z = 0 for $\theta = 0°$, respectively. Preferred orientation of crystallites accordingly leads to deviation from the ideal powder value $Z = 2$. The backscattering spectrum of Fe_2NiGa (Fig. 5.7) reveals a strongly diminished relative intensity of the second and fifth lines which suggests that the magnetization occurs essentially along the direction of the γ-beam, i.e. perpendicular to the sample surface.

Well ordered and disordered regions appear to coexist in the sample of Fe_2CuGa. The spectra of Fe_2CuGa are best described by two sharp and an additional broad sextet. The H_hf values and thus also the magnetic moments of the sharp features are very similar to those of Fe_2NiGe. These signals are attributed to Fe(A) and Fe(B) sites in well ordered domains of the material with X structure. The broad feature is assigned to domains with strong disorder. The average H_hf of 265 kOe corresponds just to the average of the H_hf values of the A and B sites. Accordingly, although the distribution of the moments is changed in course of the disorder the average magnetic moment (4.2 μ_B per formula unit) nearly remains the same. This is in agreement with the observation that the total magnetic moments in Heusler compounds frequently are not changed much by disorder. Similar spectral shapes are also obtained for Fe_2CuAl. The spectra have been approximated by two hyperfine sextets. The sharp sextet with H_hf=214 kOe is assigned to Fe(B) sites with regular coordination geometry (4 Fe and 4 Al neighbors). Its intensity contribution (33%) is, however, smaller than for an ideal inverse Heusler phase. The broad second sextet thus accounts for a superposition of Fe sites with differing environment due to disorder. As in other Al containing Heusler compounds a pronounced B2-type exchange between Fe and Al sites is expected to contribute to the disorder [68]. Antisite disorder between the Fe(B) and Al sites is possibly the origin for an enhanced intensity contribution of Fe(A)-like signals as Fe atoms at Al sites are in a similar environment as Fe(A) atoms. There is no clear evidence of an Fe-based impurity in the spectrum of Fe_2CuAl although an impurity phase was detected in the XRD pattern. This is in accord with the clue from the XRD data that the impurity corresponds to a Cu_xAl_y phase.

Having established the typical features of the Mössbauer spectra for the present materials we now discuss the results with respect to the theoretical predictions of Ref. [60]. For Fe_2CoGe the inverse cubic Heusler structure was obtained as the most stable one. This is in agreement with the Mössbauer spectra of Fe_2CoGe which show two well-defined Fe sites. For all the other materials, however, the structure predictions are contradicted by the Mössbauer spectra. In Ref. [60] an inverse Heusler structure was suggested for Fe_2NiGa. In contrast, the Mössbauer spectrum of Fe_2NiGa does not reveal the typical pattern of the inverse Heusler structure. The broad features rather point towards a strongly disordered arrangement of the atoms. In case of Fe_2NiGe, Fe_2CuGa, and Fe_2CuAl the inverse Heusler structure was shown to be more stable than the regular one, but it was suggested that there is an inherent tendency for a structural distortion. Hence, it was predicted that the regular tetragonal Heusler structure becomes more stable for these materials. As it has been shown already in Section 5.3.2, there is no sign of a tetragonal distortion in any of the present XRD patterns. The Mössbauer spectrum suggests that it is essentially the inverse Heusler structure which is adopted by Fe_2NiGe. Also the spectra of Fe_2CuGa and Fe_2CuAl show signatures of the inverse Heusler structure, however, pronounced disorder is apparent from the spectra too. Furthermore, there is no indication of quadrupole interactions in the Mössbauer spectra which would be expected for tetragonal Heusler phases.

Finally, we mention that we have tried to synthesize Fe_2ZnAl, which has also been predicted as a regular tetragonal Heusler phase [60] with a magnetic moment of $\sim 4\ \mu_B$. However, analysis of the Mössbauer spectra and XRD data of a sample with nominal composition Fe_2ZnAl revealed the presence of a non-magnetic component which was identified as FeAl. An additional magnetic component, the fraction of which increases from 10% in the 673 K annealed sample to 55% in the 1173 K sample presumably corresponds to Fe_3Al. Thus, the stabilization of a Heusler phase was not successful in this case.

5.4 Results of the electronic structure calculations

In order to gain more insight into the atomic and electronic structure and magnetism of the Fe_2YZ compounds, we have performed *ab-initio* electronic structure calculations based on density functional theory (DFT). All calculations were carried out by using the fully-relativistic Korringa-Kohn-Rostoker (KKR) Green's function method as implemented in the SPR-KKR package [72]. The exchange and correlation was treated by the

Vosko-Wilk-Nusair form of the local density approximation (LDA) [73].
The lattice parameters were taken from the experimental data (see Table 5.2). The primitive unit cell contains four atoms in the lattice with the Wyckoff positions A (0, 0, 0), B (14, 14, 14), C (12, 12, 12), D (34, 34, 34). In the regular Heusler structure the B and D positions are equivalent due to inversion symmetry, whereas in case of the inverse Heusler structure these sites become inequivalent (see Fig. 5.1). In case of the fully ordered Fe_2YZ inverse Heusler compounds sites A and B are occupied by Fe, which we will refer as Fe(A) and Fe(B) site, respectively. Since the Mössbauer measurements have clearly shown that the Heusler compounds in the Fe_2YZ series show certain degree of chemical disorder, we have considered the anti-site disorder by using the so-called coherent potential approximation (CPA) [64, 65]. In the following we will consider the cubic Heusler phases including the effects of disorder and non-stoichiometry.

5.4.1 Fe_2CoGe

To check whether the methodology presented above is suitable for the description of structural and magnetic properties of the Fe_2YZ materials, first we have performed a set of calculations for Fe_2CoGe and compared the results with the data already available from the literature [61]. We have considered four different model systems in the cubic structure, where the site occupations were selected with the following configurations: (a) fully ordered Heusler structure; (b) chemically disordered structure (50 % of Fe is mixed with Co); (c) chemically disordered inverse Heusler phase (50 % of the Fe sitting in position C mixed with Co); (d) a fully ordered inverse Heusler structure. We found, that the structure stability increases from (a) to (d). The configurations (b) and (c) are isoenergetic, sitting by 285 meV (per formula unit) lower than the ordered regular Heusler structure (a). Finally, the most stable phase appears to be the fully ordered inverse Heusler phase by about 30 meV lower energy compared to (b) and (c). Thus, the ordered regular $L2_1$ structure is unstable, and although disorder increases the stability, the most stable phase has the ordered inverse Heusler structure.

This is in good agreement with the experimental results, which suggest that Fe_2CoGe crystallizes as an inverse Heusler compound with a rather small amount of antisite disorder. For Fe_2CoGe in the X-structure the computed total magnetic moment of 5.15 μ_B is in reasonable agreement with the experimental values of 5.0-5.4 μ_B (see Table 5.3 and Ref. [61]). The calculated local moments are: 2.68, 1.51 and 1.01 μ_B on Fe(A), Fe(B), and Co, respectively. These computed values agree with the Fe moments of 2.6 and 1.6 μ_B derived from the Mössbauer spectrum of Fe_2CoGe. The present results are comparable with the calculations of Ref. [61] which report the moments of 2.74, 1.38 and 0.94 μ_B on Fe(A), Fe(B) and Co sites, respectively. By assuming the ferromagnetic order, one derives from the Mössbauer data and the measured magnetization of 5.4 μ_B the local moment of Co as 1.1 μ_B, in agreement with the present calculations. As it follows from the calculated density of states (DOS) for the ordered inverse Heusler structure (see Fig. 5.9) Fe_2CoGe is not a half-metallic ferromagnet (which is also clear from Ref. [61]).

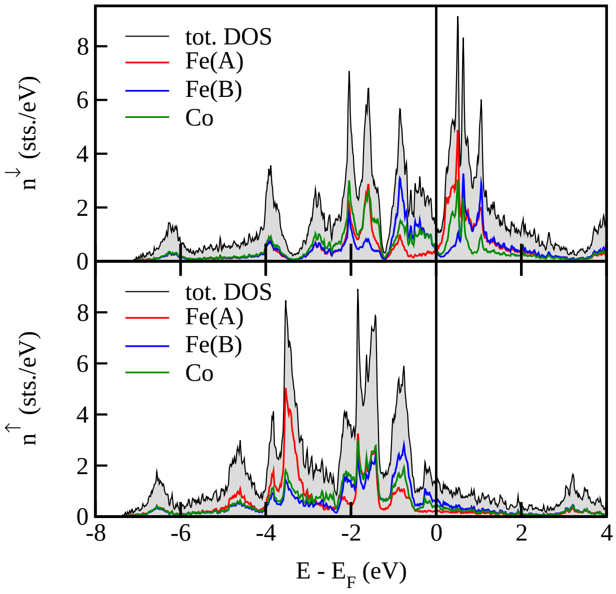

Figure 5.9: Spin resolved and atom projected DOS of Fe_2CoGe, where (a) and (b) panels correspond to the minority and majority spin channels, respectively. The red, blue and green curves refer to Fe(A), Fe(B) and Co contributions. The total DOS is shown by a gray shaded area.

5.4.2 Fe_2NiGe

The EDX data (see Table 5.1) for Fe_2NiGe indicate that the sample is slightly off-stoichiometric, with a small portion of Fe (about 2.5 %) is substituted by Ni. The line-shape of the Mössbauer spectrum suggests that the sample essentially remains ordered, but in the structure there is a certain amount of disorder present. So, for Fe_2NiGe we have theoretically investigated nine different scenarios in the inverse Heusler structure. First we have looked at the stoichiometric compound, where we considered: (a) the fully ordered inverse Heusler structure; (b) anti-site disorder between Fe(A) and Ni, where 6 % of Fe was substituted with Ni; (c) anti-site disorder between Fe(B) and Ni, where 6 % of Fe was substituted with Ni; (d) 6 % substitution of Fe(A) with Ge; (e) 6 % substitution of Fe(B) with Ge. We have also studied the off-stoichiometric compositions, where the model systems were created via: (f) removal of 3 % of Fe from site A; (g) removal of 3 % of Fe from site B; (h) 3 % substitution of Fe(A) by Ni; (i) 3 % sustitution of Fe(B) by Ni.

Indeed, calculations indicate that the fully ordered inverse Heusler structure is not the most stable configuration for Fe_2NiGe. Instead, the Fe-Ni anti-site disorder leads to more stable structures. Namely, the compositions (b) and (c) are lower in energy compared to configuration (a) by 6 and 8 meV per formula unit, respectively. In contrast to the Fe-Ni, the Fe-Ge exchange is energetically unfavorable for each of the Fe sites: compositions (d) and (e) are higher in energy by about 65 and 150 meV per formula unit compared to the fully ordered case.

Still, these small energy differences between subsequent structures are comparable with the average thermal energy of the atoms at the annealing temperature, indicating that the detailed annealing conditions can control the nature of the disorder in the Fe_2YZ inverse Heusler phases. The energy of configuration (f) is found to be 15 meV lower than (g), indicating that the creation of Fe point defects in position (A) is more likely than in position (B).

If 3% of Fe is substituted by an additional 3% of Ni, the structures (h) and (i) are isoenergetic, i. e. in this specific case from the perspective of the total energy the system is not biased towards Fe(A) or Fe(B) sites. This means, that with slight Ni excess, Fe atoms are randomly removed both from positions A and B, and the empty sites are being occupied with Ni. The spin-resolved and atom-projected DOS computed for the fully ordered stoichiometric Fe_2NiGe in the inverse Heusler structure is shown in Fig. 5.10. For the inverse Heusler phase the calculated total moment is 4.47 μ_B per formula unit,

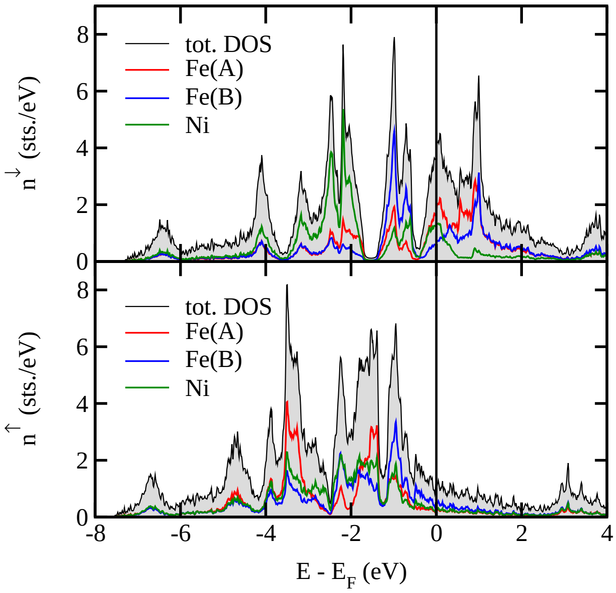

Figure 5.10: Spin resolved and atom projected DOS of Fe_2NiGe, where panels (a) and (b) correspond to the minority and majority spin channels, respectively. The contributions of Fe(A), Fe(B) and Ni are represented with red, blue and green curves. The total DOS is shown by a gray shaded area.

which agrees with the experimental moments of 4.29 or 4.46 μ_B measured for the samples with SQUID magnetometry. The computed local moments on Fe(A), Fe(B) and Ni atoms are 2.53, 1.67 and 0.29 μ_B respectively. The Fe local moments agree with those derived from Mössbauer measurements: 2.5 and 1.7 μ_B for the Fe(A) and Fe(B) sites. Similar behavior was found for the disordered structures (b)–(e) corresponding to the stoichiometric composition.

In cases (h) and (i) in which Fe was substituted by Ni, corresponding to the composition measured via EDX, the calculated total moments were 4.39 and 4.42 μ_B, respectively.

For structures (f) and (g), where 3 % of Fe is missing (no additional Ni present), the total moments were 4.38 and 4.43 μ_B, respectively. For those cases which resemble the experimental composition, the respective local moments were 2.52, 1.68 and 0.31 μ_B for configuration (i) and for structure (h) 2.54, 1.67 and 0.29 μ_B for Fe(A), Fe(B) and Ni, respectively.

Thus, a small amount of disorder, Fe deficiency or Ni excess do not change considerably the magnetic properties of Fe_2NiGe in the inverse Heusler structure.

5.4.3 Fe_2NiGa

In case of Fe_2NiGa the experimental results presented in the previous section have pointed out that the material exhibits rather strong degree of disorder. To sample the potential atomic arrangement in the disordered phase, we have carried out calculations on eleven model systems each having a stoichiometric composition.

The first scenario was the ordered inverse Heusler structure, which served as reference. For the fully ordered structure we have calculated a magnetic moment of 4.81 μ_B, which is by about 0.6 μ_B higher than the experimentally measured value of 4.20 μ_B.

Next we have looked into the effect of antisite disorder upon the magnetization and energetics of Fe_2NiGa between Fe(A) and Fe(B) and Ni and Ga for stoichiometric compositions. We found, that by exchanging the site occupation of Fe(A) with 10, 20 and 50% of Ni, the structures generated hereby are higher in energy by about 14, 15 and 89 meV per formula unit, respectively, compared to the ideal inverse Heusler phase. This indicates that a small amount of Fe(A) (up to about 10–20 %) can be exchanged by Ni rather easily.

In contrast to this, if one exchanges 50-60 % of Fe(B) with Ni, the structure with Fe(B)-Ni antisite disorder becomes more stable by about 9 meV per formula unit than the ordered phase. Thus, in case of Fe_2NiGa the ground state does not correspond to the fully ordered inverse Heusler phase. For the lowest energy configuration the calculated total moment is 4.77 μ_B, where the local moments on Fe(A), Fe(B) and Ni are 2.65, 1.86 and 0.33 μ_B, respectively. Thus, the magnetic moment of this structure is still higher than the SQUID data by about 4.2 μ_B per unit cell.

Also the average moment on the Fe sites of 2.25 μ_B is somewhat higher than the average moment of 2.05 μ_B estimated from the broad sextets in the Mössbauer spectrum. Upon exchanging either Fe(A) or Fe(B) with Ga the disordered structures were all unstable relative to the reference case independent of the Fe position. The total magnetic moments of the systems with Fe-Ni and Fe-Ga exchange are computed in the range from 5.03 to 4.59 μ_B.

Due to the fact that the Mössbauer spectra may suggest random alloying, we have also considered the case of an A2-type structure, where the constituent atoms are randomly distributed on all four lattice sites. The calculations have shown, that such an A2-type random structure where all atoms are coupled ferromagnetically, is rather unstable, by about 440 meV per formula unit compared to the reference, which is the ordered inverse Heusler phase.

5.4.4 Fe_2CuGa

For the Fe_2CuGa sample the experiment reveals both well-ordered and disordered regions. Since the ordered regions should correspond to the ideal ferromagnetic inverse Heusler structure, we have first investigated this configuration. The corresponding spin-resolved and atom-projected DOS is shown in Figure 5.11. The calculated total magnetic moment of 4.04 μ_B is somewhat larger than the experimental one (3.6 μ_B) derived from the SQUID measurements. The origin of this small discrepancy cannot be resolved unambiguously, however, the experimental moment may be too small due to the presence of the minor impurity phase as suggested by the XRD pattern. On the other hand, the calculated local moments of 2.34 μ_B for Fe(A) and 1.78 μ_B for Fe(B) sites agree with the corresponding values of 2.5 and 1.7 μ_B derived from the sharp features in the Mössbauer spectrum. The moments on the Cu and Ga sites are negligibly small.

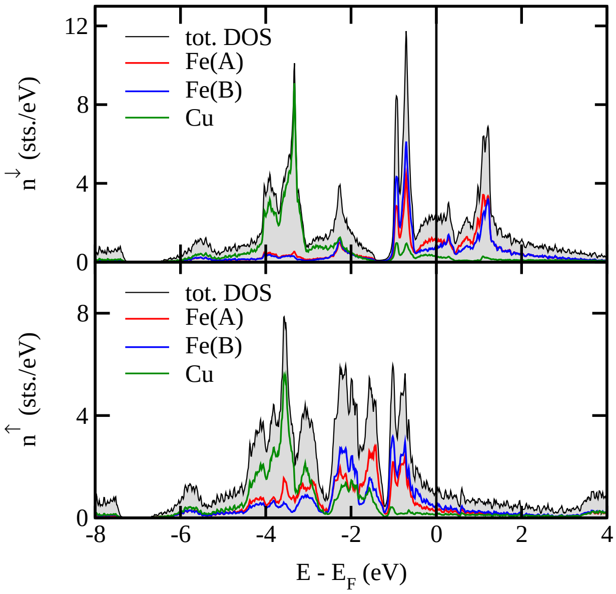

Figure 5.11: Spin resolved and atom projected DOS of Fe_2CuGa. Panels (a) and (b) correspond to the minority and majority spin channels, respectively. The contributions of Fe(A), Fe(B) and Cu are shown with red, blue and green curves, respectively, and the total DOS is shown by a gray shaded area.

To gain new insights via CPA on the potential nature of the disordered phase, we have carried out calculations for six configurations taking into account various kinds of Fe-Cu and Fe-Ga antisite disorder. The calculations indicate that 50 % of Cu-Fe(A) exchange leads to a more stable structure compared to the fully ordered inverse Heusler structure with a stabilization energy of 71 meV per primitive unit cell. Beside this, we found that an even more stable configuration can be created via chemical disorder, where alloying is present between Fe and Cu, with 18, 44 and 44 % of Fe-Cu antisite exchange on Wyckoff positions A, B and D, respectively. This structure is by 110 meV lower in energy compared to the ideal ordered inverse Heusler structure, which indicates that the system might undergo a spontaneous mixing between Fe and Cu, giving rise to the appearance of a broad sextet seen in the Mössbauer spectra. For the systems with Fe-Cu disorder the total magnetic moments assuming ferromagnetic ordering have been calculated to be in the range of 4.29-4.31 μ_B, where the local moments were 2.48, 1.95 and 1.94 μ_B for Fe(A), Fe(B) and Fe(D), respectively. The average value of 2.1 μ_B over these sites is in good agreement with the average moment of 2.1 μ_B estimated from the hyperfine field value of the broad sextet.

Next we considered the effect of Fe-Ga disorder, which has shown that even a small amount of Fe-Ga antisites is energetically unfavorable. For 10 % of antisite disorder on Fe(A) or Fe(B) sites the structures were less stable, by about 30 and 85 meV per formula unit, respectively, compared to the ordered inverse Heusler structure. This indicates that Fe-Ga antisite disorder in Fe_2CuGa is less likely to happen than Fe-Cu alloying. The calculated total moments in case of Fe-Ga antisite disorder are in the range of 4.15-4.25 μ_B which are only slightly enhanced compared to the ideal X-structure.

5.4.5 Fe_2CuAl

For the Fe_2CuAl sample it was found experimentally, that the sextet assigned to Fe(B) in the Mössbauer spectra has a lower intensity than it should have in the ordered inverse Heusler phase, indicating that there is a certain amount of disorder involved. Also, there is a second broad sextet with enhanced relative intensity present, pointing towards different local Fe coordination environments. These spectral features suggest an inverse Heusler structure, where Fe(B)-Al antisite disorder leads to an enhanced fraction of Fe(A)-like sites. We have first investigated the ideal X-phase of Fe_2CuAl theoretically, for which the computed total DOS and atom projected DOS is shown in Fig.5.12. The calculated total moment of 3.80 μ_B considering ferromagnetic ordering is somewhat higher than the measured value of 3.3 μ_B. The experimental value may, however, be too small as there is an impurity phase evident in the XRD pattern. Similar to the case of Fe_2CuGa the local moments deduced from the Mössbauer spectra on Fe(A) and Fe(B) sites of 2.2 and 1.7 μ_B, are in a real good agreement with the calculated local moments of 2.23 and 1.67 μ_B. This confirms that Fe_2CuAl basically crystallizes in a cubic inverse Heusler structure. Further, we studied the effects of Fe-Cu or Fe-Al antisites. Up to 30% of Fe-Cu antisite exchange the structure is more stable by about 12 meV per formula unit compared to the ideal inverse structure, and going above 30% the structure become less stable by about around 15 meV.

By exchanging Fe with Al the calculations show that the structures generated are practically isoenergetic with the ordered inverse Heusler structure. This result agrees with the experimental observations from Ref. [68]. The total moments for configurations with Fe-Cu and Fe-Al disorder are in the range of 3.91-3.96 and 3.80-3.81 μ_B, respectively, which is similar as in case of the fully ordered Heusler phase. Thus, the calculations indicate, that although there is a slight bias towards the Fe-Cu antisite disorder, in Fe_2CuAl the spontaneous formation of both Fe-Cu and Fe-Al type disorder is highly likely. As it follows, in many cases the antisite disorder does not change radically the magnetic properties of the Heusler compounds.

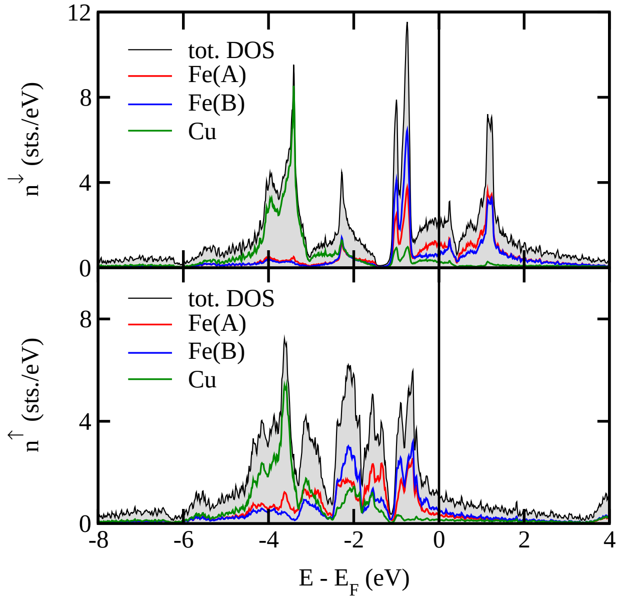

Figure 5.12: Spin resolved and atom projected DOS of Fe_2CuAl, where (a) and (b) panels correspond to the minority and majority spin channels, respectively. The red, blue and green curves refer to Fe(A), Fe(B) and Cu contributions. The total DOS is shown by a gray shaded area.

5.4.6 Fe_2ZnAl

Finally we considered the case of Fe_2ZnAl (predicted theoretically [60]). We have investigated the hypothetical inverse cubic Heusler structure, and found that the calculated total moment of 3.27 μ_B is nearly twice larger than the experimental moment of a sample with the nominal composition Fe_2ZnAl. Such significant discrepancy suggests that the sample is not a Heusler phase. In fact, the XRD and Mössbauer data revealed that in the mixed-phase samples non-magnetic FeAl, in addition to Fe_3Al were the major iron-based components.

5.5 Conclusions

We have synthesized and characterized the new iron-based Heusler phases Fe_2NiGe, Fe_2CuGa, and Fe_2CuAl, the existence of which has been suggested by previous theoretical work [60]. In addition we have investigated in more detail the known compounds Fe_2CoGe and Fe_2NiGa. The newly synthesized Fe_2YZ phases were predicted to adopt a regular tetragonal Heusler structure, whereas the present experimental results revealed that the materials basically crystallize in the cubic inverse Heusler (X-) structure with differing degrees of atomic disorder. For these Fe-based materials ^{57}Fe Mössbauer spectroscopy is a very useful local-probe technique to unravel the atomic disorder and to estimate the magnetic moments at the iron sites. All the compounds are soft ferromagnets with Curie temperatures up to about 900 K which makes them suitable for potential magnetic applications. The electronic structures of the materials have been studied by *ab-initio* DFT calculations including the effects of disorder and nonstoichiometry within the CPA approximation. The good agreement between calculated and experimental magnetic moments at the Fe sites is further support that the compounds basically adopt the cubic inverse Heusler structure. Atomic disorder which is apparent in the experimental data leads to further stabilization of the cubic structure without changing the magnetic properties too much. The case of Fe_2NiGa, which was predicted to crystallize in the cubic X-structure is not completely clear yet. Both, XRD and Mössbauer data evidence an increased atomic disorder and the calculated magnetic moments are somewhat higher than the experimental ones. Attempts to synthesize Fe_2ZnAl, a further phase which was also suggested to adopt the tetragonal Heusler structure [60], were unsuccessful. While there is a good consistency between the present experimental and theoretical results for the cubic inverse Heusler Fe_2YZ materials it remains to be clarified why Fe_2NiGe, Fe_2CuGa, and Fe_2CuAl do not adopt the tetragonal structures predicted previously.

6 Structural and magnetic properties of tetragonal Mn_2FeGa as a candidate for spin transfer torque

6.1 Introduction

Heusler compounds are due to their low Gilbert damping constants, high spin polarizations, and low magnetic moments interesting materials for spin torque transfer applications [23]. The tetragonal DO_{22} phase of the binary intermetallic and ferrimagnetic compound Mn_3Ga corresponds to a distorted cubic Heusler structure. It is in the center of attraction due to its low saturation magnetization, high Curie temperature (T_C), and high spin polarization [26, 25]. These are necessary preconditions for spin torque transfer applications in order to realize low switching currents and a high efficiency of spin injection. The tetragonal DO_{22} alloys $Mn_{3-x}Ga$ were shown to exhibit similar properties, which allow adjustment of certain parameters such as magnetic moment, coercivity, or magnetic remanence by variation of the Mn content [25]. Epitaxial thin films of these materials have been shown to exhibit giant perpendicular magnetic anisotropy (PMA) [74]. The films are thus highly interesting for implementation in spin valves or magnetic tunnel junctions [30]. The idea of this work consists in the substitution of one Mn atom by Fe. The Fe atoms should preferentially occupy the tetrahedrally coordinated positions in the unit cell due to their higher electronegativity as compared to Mn. This feature is known from the related Heusler compounds where the electronegative atoms always occupy the 8c position [34, 75, 76] with T_d symmetry [77]. The compound Mn_2FeGa is up to the present only mentioned in a theoretical study, where a cubic inverse Heusler structure was assumed [78]. Experimentally, however, we find either the tetragonally distorted structure or a more disordered phase with Cu_3Au-like structure. The experimental results of the new tetragonal compound Mn_2FeGa are very promising and suggest that it can be an important material for spin torque transfer applications (STT) as the related Mn_3Ga, especially if it is optimized as thin film structures.

6.1.1 Synthesis

Tetragonal Mn_2FeGa was obtained by repeated arc melting of stoichiometric mixtures of the corresponding elements in an argon atmosphere. Care was taken to avoid oxygen contamination. The samples were annealed afterwards for 2 weeks at different temperatures in evacuated quartz tubes. The temperature was chosen to be safely below the phase transition temperature to a hexagonal structure, which was identified using high-temperature powder x-ray diffraction (XRD) [79]. The best quality showed the sample annealed at 400 °C. After the annealing process, the samples were quenched in a mixture of ice and water to retain the desired tetragonal structure. The XRD measurements were performed at room temperature in reflection geometry in a θ-θ scanning mode. The results were fitted using the software FullProf. Using a superconducting quantum interference device (SQUID) the magnetic properties were determined in a temperature range from 5-800 K. ^{57}Fe-Mössbauer spectroscopic measurements were carried out in backscattering mode using the miniaturized Mössbauer spectrometer MIMOS and a constant acceleration drive equipped with a ^{57}Co (Rh) source with an energy of hv = 14.4 keV [32]. The data were fitted using the Recoil software and the Voigt- based fitting method (VBF) [33].

6.2 Structure characterization

The crystal structure of two samples annealed at 400 °C and 800 °C, respectively, was investigated using XRD at room temperature with Mo-K_{α_1,α_2} radiation and Rietveld refinement. No impurities were identified in the diffraction patterns depicted in Fig. 6.1(a,b).

The diffraction pattern of Fig. 6.1(a) indicates broader peaks than the diffraction pattern of Fig. 6.1(b). This will be later explained in detail, based on the high amount of disordering. The crystal structure of Mn_2FeGa annealed at 400 °C was identified to be a tetragonally distorted inverse Heusler structure (space group number 119, $I\bar{4}m2$) and the lattice parameters are a= 3.7915(1) Å and c= 7.1858(2) Å. This corresponds to a c/a ratio of 1.89. The splitting of the main cubic peak (220) into (112) and (200) peaks

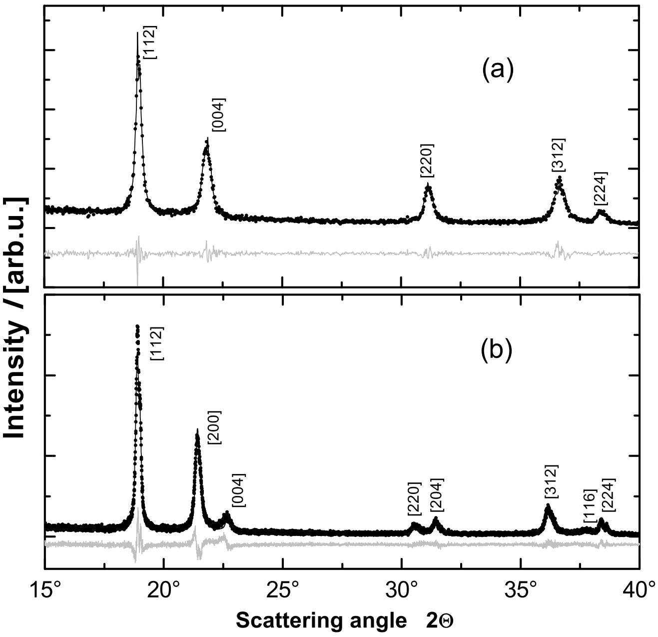

Figure 6.1: Diffraction pattern of Mn_2FeGa annealed at 400 °C (b) and 800 °C (a). The diffraction pattern (black) is compared to the curve fit from the Rietveld refinement (gray). The measurement was carried out at room temperature using a Bruker D8 diffractometer equipped with a Mo K_α x-ray.

in the corresponding XRD pattern is a clear evidence for the tetragonal structure. The remaining deviations of the intensities of the refined curve to the experimental one are possibly due to the fact that Mn_2FeGa is a highly ductile bulk material, which cannot be ground to a fine powder. The measurement was therefore carried out using a cut and polished disc of the sample. The XRD pattern of the 800 °C-annealed sample differs considerably from that of the the 400 °C-annealed sample. At first sight it appears like a cubic diffraction pattern. However it is not typical for the cubic inverse Heusler structure which was assumed in previous theoretical calculations on Mn_2FeGa [78] but it rather corresponds to the cubic Cu_3Au structure (space group $Pm\overline{3}m$; no. 221). This suggests that in the 800 °C-annealed sample the Fe and Mn atoms are statistically distributed, in contrast to the ordered arrangement in the Heusler structure. We have attempted to refine the data assuming space group $Pm\overline{3}m$. The corresponding lattice parameter was found to be a=3.7526 (1) $\mathring{A}$. However, the lines are somewhat broad and asymmetric. Furthermore, there was still a mismatch in the peak positions. Accordingly we assumed a symmetry lowering and refined the data in the tetragonal space group I4/mmm including preferred orientation effects in the disc shaped samples. This way a better agreement was achieved (Fig. 6.1,a) yielding the lattice parameters a=3.7150 (6) $\mathring{A}$ and c=7.5108 (1) $\mathring{A}$. The ratio c/a=2.02 is close to 2. Accordingly this Mn_2FeGa phase may be described by a pseudocubic unit cell with a doubled a-parameter giving c (c=2a). The pseudo-cubic structure is the consequence of the statistical distribution of the Fe and Mn atoms. The view derived from the XRD data is further supported by the Mössbauer data (see below).

6.3 Magnetic and Mössbauer studies

6.3.1 SQUID results

Magnetic measurements using SQUID magnetometry and Mössbauer results yield the informations concerning the nature of the magnetism of Mn_2FeGa annealed at elevated temperatures. For the tetragonal sample annealed at 400 °C the magnetization measurements are given in Figure 6.2. As it follows the obtained hysteresis almost reaches a saturation of magnetization at 10 T. Magnetic moments at 10 T derived from the hysteresis at 300 K and 5 K are equal, namely 1.53 μ_B. The coercive field H_C [80] was found to be 0.43 T whereas the remanent magnetization is $0.24\,\mu_B/f.u.$ The temperature dependent magnetization (see, Fig 6.2) exhibits a drastic decrease at approximately 650 K. As found from the sample annealed at 600 °C (see, appendix), this is related to a phase transition to a hexagonal structure (structure type: Ni_3Sn, space group $P6_3/mmc$) and therefore does not correspond to the intrinsic T_C of the tetragonal phase. Temperature dependent magnetization measurements in a field of 1 T performed under zero field cooling-ZFC and field cooling-FC conditions within the temperature range 400 K-5 K did not reveal major changes of the magnetic moment. Zero-field cooling (ZFC) means, the sample was cooled to a temperature of 5 K without applying a magnetic field. Then, at 5 K a magnetic field of 1 T was applied, and the sample was heated to 300 K. Afterwards the magnetization at the same field was measured as the temperature was lowered, which

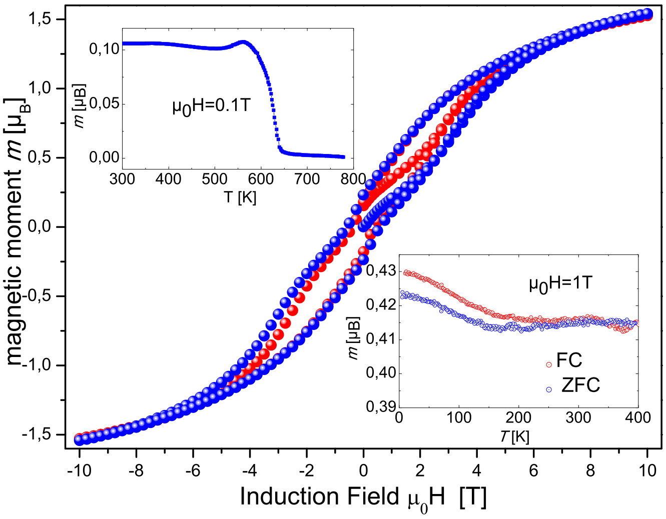

Figure 6.2: Hysteresis at 5 K (blue) and 300 K (red) of Mn$_2$FeGa annealed at 400 °C. The inset (right) shows M (T) applying a magnetic field of 1 T within the wide temperature range 400 K-5 K, whereas the inset (left) gives the M (T) in temperature range of 400 K-800 K at 0.1 T.

is known as field cooling (FC). Magnetic measurements of Mn$_2$FeGa annealed at 800 °C are given in Figure 6.3. Comparison of Fig. 6.2 and Fig. 6.3 reveals that the magnetic properties of the 800 °C-annealed sample and the 400 °C sample differ considerably. While there is a ferro-(i) magnetic transition near 650 K in both samples which appears, however, to be related to the formation of the hexagonal phase (Fig. 6.3, inset) the M (H) behavior is different. The M (H) curves for the 800 °C-sample reveal a sigmoidal shape only below 1 T and increase linearly with H at higher fields. This indicates a predominant antiferromagnetic type of ordering. The sigmoidal character at low fields may point to a spin canting or a minority ferro- or ferrimagnetic phase.

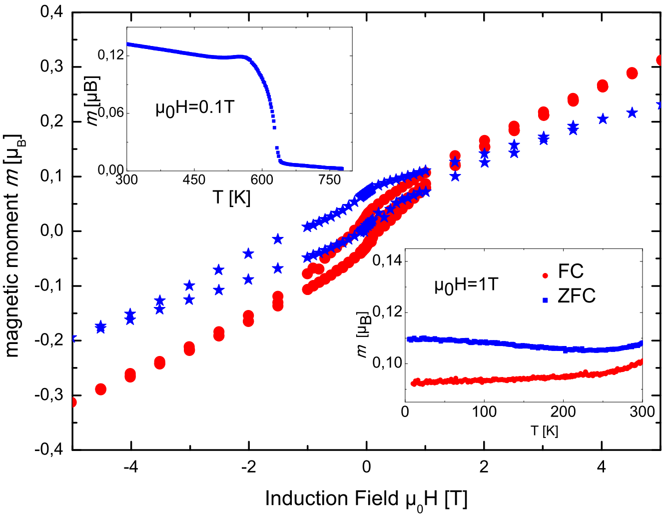

Figure 6.3: Hysteresis at 5 K (blue) and 300 K (red) of Mn_2FeGa annealed at 800 °C. The inset (left) gives temperatures dependent magnetization (M (T)) within the temperature range 300 K-800 K, and the inset (right) shows the temperature dependent magnetization (M (T)) over the temperature range 300 K-5 K.

Table 6.1: Mössbauer data of Mn_2FeGa.

Mn_2FeGa annealed at	H_{hf} [kOe]	A [%]	CS [mm/s]	QS [mm/s]	μ_{Fe} [μ_B]
400 °C	214 (2)	20	0.17 (1)	0.14 (2)	1.7
	64 (1)	80	0.044 (4)	-0.088 (1)	0.5
800 °C	64 (1)	84	-0.12 (1)	0	0.5
	48 (1)	16	-0.12 (1)	0	0.4

6.3.2 Mössbauer results

Due to the similar scattering factors of the d-elements XRD-measurements often are not able to give the crucial information about the anti site disorder in Heusler compounds. In that case Mössbauer spectroscopy is a useful tool due to the ability to study the atomic local environment of particular elements. In our case we have applied ^{57}Fe-Mössbauer spectroscopy to clarify the local surroundings of Fe-atoms in Mn_2FeGa. We use the benefit of the sensitivity of the hyperfine magnetic splitting to the local surroundings of a Mössbauer atom in Heusler related phases. In this study we have characterized Mn_2FeGa by the backscattering method [32]. We did not use transmission Mössbauer spectroscopy because of the ductility of the samples. This method is also useful when grinding of the samples can provoke a structural phase transition and a concomitant change of the magnetic phase. According to the ideal inverse tetragonal Heusler structure of the compound there should be only one Fe-position and therefore one Fe signal. The experimental spectra are, however, more complicated and they were approximated by two components with a distribution of hyperfine fields. We have assigned the majority component (80%) in the spectrum of the 400 °C sample (see,Fig. 6.4)

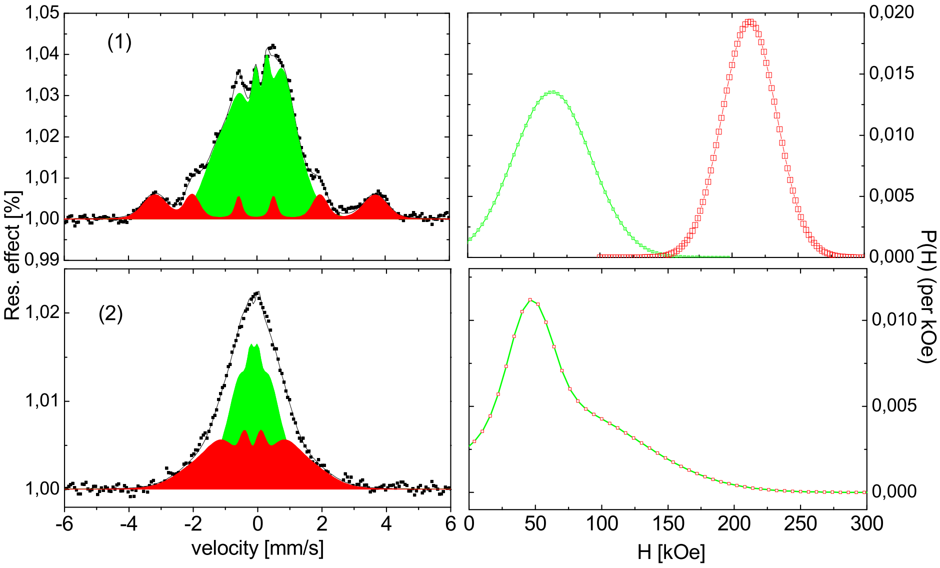

Figure 6.4: Backscattering Mössbauer spectra of Mn_2FeGa at room temperature (1) annealed at 400 °C, (2) annealed at 800 °C. Right:$|H_{hf}|$ distributions obtained from the spectra on the left.

to the crystallographic Fe-positions with two Mn and two Ga atoms in the first coordination sphere, as expected for the inverse Heusler structure. The hyperfine field of the major fraction was found to be 64 (1) kOe ($\mu_{Fe} \approx 0.5\,\mu_B$) and that of the minor fraction was found to be 214 (2) kOe ($\mu_{Fe} \approx 1.7\,\mu_B$). As in our work on other Fe_2YZ phases (Section X) we have assumed that 125 kOe corresponds to a magnetic moment of 1 μ_B. Theoretical calculations on Mn_2FeGa assuming an inverse cubic Heusler structure revealed only small magnetic moments at the Fe sites (0.28 μ_B) [78]. However, the second Fe-component (20 %) has a much higher hyperfine magnetic field and therefore a higher magnetic moment which indicates strong magnetic exchange with the local surrounding. We conclude that in this case Fe substitutes partially Mn sites having four Fe-atoms in the first coordination sphere. The resulting Mn-Fe disorder explains also the broad H_{hf} distribution in the majority signal. Noticeable values of the quadrupole interaction parameter QS in both Fe-positions confirm the tetragonal structure of Mn_2FeGa suggested by Figure 6.1. The spectrum of the sample annealed at 800 °C differs significantly from that of the sample annealed at 400 °C. In particular the Fe sites with large H_{hf} values and pronounced quadrupole interaction have completely disappeared. Instead a broad, nearly structureless feature corresponding to a broad H_{hf} distribution is observed. The latter was approximated by two components with average H_{hf} values of 64 (1) kOe (84%) and 48(1) kOe (16%), respectively. The average magnetic moment at the Fe sites is about $0.5\,\mu_B$. These results are consistent with the XRD pattern which suggests an essentially cubic, disordered Cu_3Au structure for Mn_2FeGa annealed at 800 °C, where Fe and Mn atoms are statistically distributed. The large H_{hf} variation at the Fe sites reflects the varying local environment of the Fe atoms. Furthermore, the H_{hf} distribution is essentially symmetric with respect to the center of the pattern with no signs of quadrupole interaction, in contrast to the spectrum of the 400 °C annealed sample. This confirms that the 800 °C annealed sample is essentially cubic. Considering in addition the bulk magnetization measurements with small magnetic moments (see, Fig. 6.3) described above it is concluded that for the 800 °C-annealed sample, Mn_2FeGa reveals mainly antiferromagnetic order with quite small moments at the Fe atoms and possibly large moments at the Mn atoms.

Finally, we mention that Mn_2FeGa was prepared at different temperatures (400 °C, 600 °C, 800 °C and 1100 °C), because we have tried to optimize this compound for better quality or less anti site disordering, respectively. At 1100 °C the sample was evaporated. However, at 800 °C the material was successfully synthesized but the disordering effect increased. The sample prepared at 600 °C becomes mainly hexagonal ($\approx 70\,\%$), in addtition a fraction ($\approx 30\,\%$) of the pseudocubic phase is observed. We conclude that Mn_2FeGa prepared at higher temperatures tends to an increase of disorder.

6.4 Summary

In summary, we have synthesized and characterized the new Heusler compound Mn_2FeGa, which was theoretically predicted to be a ferrimagnetic half-metal [78]. It was suggested to exist in the inverse cubic Heusler structure with a total magnetic moment of $1\,\mu_B$, where iron contributes only a small magnetic moment ($0.28\,\mu_B$). Experimentally, however, we find that Mn_2FeGa annealed at 400 °C crystallizes in the inverse tetragonal Heusler structure ($I\bar{4}m2$). This compound exhibits a low magnetic moment of $\approx 1.5\,\mu_B$ at 10 T, hard-magnetic behavior at room temperature, and a high thermal stability of the magnetization up to 650 K. Mössbauer studies of this compound display a certain Mn-Fe anti site disordering and approve the tetragonal structure due to the occurrence of a quadrupole splitting. It is confirmed that the majority fraction of the Fe sites indeed contributes a small magnetic moment of about $\approx 0.5\,\mu_B$, whereas Fe sites at Mn positions show much larger moment of $\approx 1.7\,\mu_B$. In contrast, both, XRD and magnetic data of Mn_2FeGa annealed at 800 °C differ clearly from the results of Mn_2FeGa annealed at 400 °C. The Mössbauer data have shown that with increasing the annealing temperature the anti site disorder increases, and therefore the magnetic properties also changes. Furthermore, the crystal structure changes to a pseudocubic Cu_3Au-like structure, which is confirmed by the lack of a quadrupole splitting in the Mössbauer spectrum. We have shown that the structural and magnetic properties of Mn_2FeGa crucially depend on the synthesis conditions. This suggests that the properties of Mn_2FeGa can be further optimized in thin film devices where atomic order and crystal structure can be controlled by layer to -layer deposition and the application of epitaxial strain.

7 Magnetic and structural properties of Fe_2MnGa

7.1 Introduction

A wide range of Heusler compounds have been synthesized for their possible applications in various fields. Of particular interest are Heuslers that show half-metallicity, which possesses a great importance in spintronics. Co-based compounds are interesting and well investigated for their role as spin-injector[4]. The existence of compensated ferrimagnetic ordering that eventually results in low saturation magnetization in some of the Mn_2YZ-based Heusler compounds also makes them potential candidates for spintronic applications[81, 41]. In addition, the tetragonal alloys are potential materials for achieving perpendicular magnetic anisotropy (PMA) required for high density perpendicular magnetic recording media [82, 83]. The observation of exchange bias (EB) in Mn_2PtIn stimulates further searching for new Heuslers with improved properties for spintronics[84]. Since the theoretical prediction of half metallicity in Fe_2MnGa[85], a fair amount of work has been reported by various groups. However, the structural and magnetic properties of Fe_2MnGa seem to be controversial as different groups obtained different results[85, 86, 87]. It is also reported that a small change in Fe/Mn/Ga ratio can induce a martensitic structural transition in the system[88]. However, a martinsitic structural transition was found in Fe_2MnGa single crystals, which feature led to a shape memory effect [55]. A comparable prototype for this effect is Mn_2NiGa, where a martenistic structure transition occurs near room temperature [89]. Though the stoichiometric bulk compound Fe_2MnGa possibly does not show any structural transition, it undergoes a ferromagnetic (FM) to antiferromagnetic (AFM) like transition near room temperature. Tang et al. have reported the existence of exchange bias (EB) behavior in melt spun ribbon γ-Fe_2MnGa [87]. However, to date no such behavior has been studied in the bulk compound. In a recent work Kudryavtsev et al. have reported the existence of two cubic phases in bulk Fe_2MnGa [86]. Here we report a structural study and magnetic properties of single phase bulk Fe_2MnGa. We have found that even bulk Fe_2MnGa shows large EB behavior. We discuss the possible origin of such behavior with help of dc (direct current)-magnetization and ac (alternating current)-susceptibility measurements. All these properties and the simple fabrication of the sample, make Fe_2MnGa attractive as a suitable material for spintronics [55]. One should notice that if the constituents of Heusler compounds have similar radii, an antisite disordering may occur, which mostly destroys the half-metallicity. Hence, a thorough investigation of disorder effects and their influence on the magnetic transition was performed employing ^{57}Fe Mössbauer spectroscopy.

7.2 Experimental Details

Polycrystalline ingots of Fe_2MnGa were synthesized by arc melting stoichiometric amounts of the constituent elements in a high purity argon atmosphere. The final weight loss was less than 0.5 % of the initial weight. Additionally, the sample was annealed at 400°C, 600°C, 800°C and 1100°C. To extend the structural and magnetic properties of this compound, we have rolled a disc of the as-grown sample into a foil with a thicknes of $100\,\mu m$. All the materials were structurally characterized by x-ray powder diffraction (XRD) using Cu-K_α and Mo-$K_{\alpha\,1,\alpha\,2}$ radiation. Magnetization measurements were carried out on the samples using a superconducting quantum interference device (SQUID) vibrating sample magnetometer (VSM). ^{57}Fe-Mössbauer measurements were performed in backscattering and CEMS (conversion electron Mössbauer spectroscopy) modes using a constant acceleration spectrometer with a ^{57}Co (Rh-matrix) source with $h\nu = 14.4\,keV$. The backscattering spectra within the temperature range 300 K-120 K were recorded with the miniaturized Mössbauer spectrometer MIMOS [32]. For the Mössbauer measurements at low temperatures a chamber supplied by liquid nitrogen was used.

7.3 Fe_2MnGa not annealed

7.3.1 Structural characterization

The room temperature XRD pattern for Fe_2MnGa not annealed is shown in Figure 7.1. Due to the hard and ductile nature of the sample a piece of Fe_2MnGa with flat and polished surface was used for the XRD measurement. To learn about the phase purity and the crystal structure, at first we have performed a Rietveld refinement using the space group $Pm\overline{3}m$ (space group no. 221, Cu_3Au-type), since the corresponding XRD pattern appears at first glance to be cubic. According to many publications, a cubic structure was assumed, for instance, many theoretical calculations predicted the $L2_1$ structure [85, 55], while experiments established the $L1_2(Cu_3Au)$ cubic structure [55]. In the Cu_3Au-type structure Fe and Mn occupy (0, 1/2, 1/2) and Ga atoms (0, 0, 0) Wyckoff positions, which means that Fe and Mn are disordered. In contrast, the $L2_1$ Heusler structure offers an ordered arrangement of Mn and Fe sites on octahedral and tetrahedral positions. The refinement clearly shows that the not annealed sample is single phase. The extracted lattice parameter is found to be a=3.7221(8) Å. The absence of the (100) and (110) cubic reflections in the experimental pattern expected for a $L1_2$ ($Pm\overline{3}m$) structure, indicates that disorder between the transition metal (Fe or Mn) and Ga sites may be an issue which will be later discussed in the chapter of the Mössbauer results. We prepared different batches of samples to verify the observed pattern and got similar XRD patterns with the same lattice parameter. As in Figure 7.1(a, inset) shown, a mismatch in the peak (200) is revealed in the corresponding XRD pattern between the theoretical and experimental curve. Therefore, we refined the data using the tetragonal I4/mmm structure including preferred orientation effects. Accordingly a better agreement in the peak positions was achieved. Hence, the Fe_2MnGa phase may be described by a pseudocubic structure as a consequence of a nearly statistical distribution of the Mn and Fe atoms. This clue is

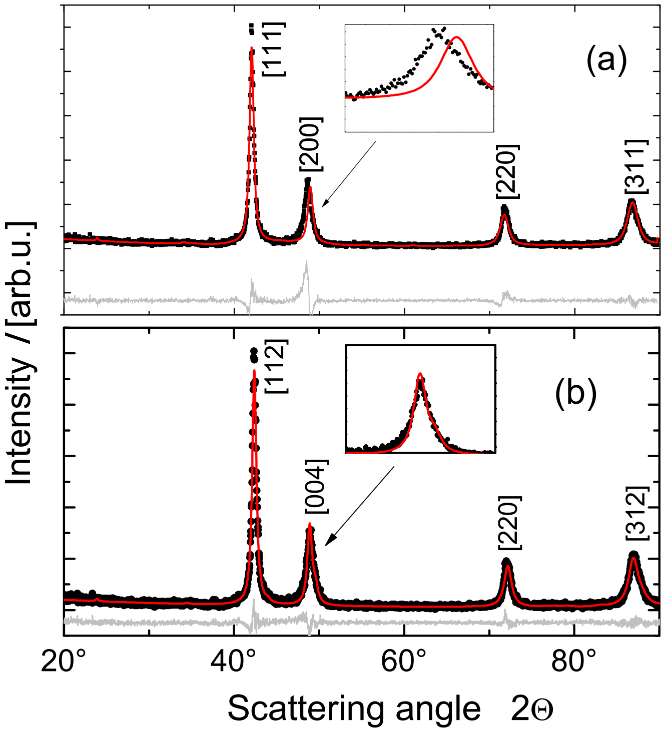

Figure 7.1: Diffraction pattern of Fe_2MnGa not annealed. The diffraction pattern (red) is compared to the curve fit from the Rietveld refinement (gray). The measurement was carried out at room temperature using excitation by Cu-$K_{\alpha1}$. Rietveld refinement using the space group Pm$\bar{3}$m is given in a, whereas Rietveld refinement using the space group I4/mmm is depicted in b. The insets (a) and (b) show the zooming of the mismatch in the peak position *(200)* or the agreement in the peak position (004), respectively.

also supported by results of Mössbauer measurements. The lattice parameters are found to be a=3.6767(2) Å and c=7.4400(2) Å. The corresponding ratio of c/a is 2.02. The observation of c/a=2.02 which is close to 2 and the lack of a quadrupole splitting in the Mössbauer data suggest a pseudocubic Cu_3Au-like structure (see, chapter Mn_2FeGa). The XRD pattern (Fig. 7.1) is not compatible with a $L2_1$ structure assumed in some theoretical calculations [85].

7.3.2 Magnetic properties

Magnetic hysteresis curves of Fe_2MnGa at different temperatures within the temperature range 5-300 K are summarized in Figure 7.2. It is found that at room temperature the sample exhibits soft magnetic properties and at lower temperatures (200 K-5 K) becomes hard-magnetic. The magnetic moment observed at room temperature at 5 T is found to be 3.6 μ_B for Fe_2MnGa, which is much higher than many theoretical calculations have predicted for the $L2_1$ phase [85], namely 2.02 μ_B. The temperature dependence of the magnetization [M (T)] measured in zero field cooled (ZFC), field cooled (FC) and field heated (FH) mode in a field of 0.1 T is shown in Fig. 7.3. In the ZFC mode, the sample was initially cooled to 2 K and the data were taken upon increasing the temperature in applied field. In the FC mode, the data were collected while cooling in field and subsequently in FH mode the data were collected during heating. It has been found that upon decreasing temperature the sample undergoes a sudden decrease in magnetization around 300 K. Furthermore, to study the nature of this transition we

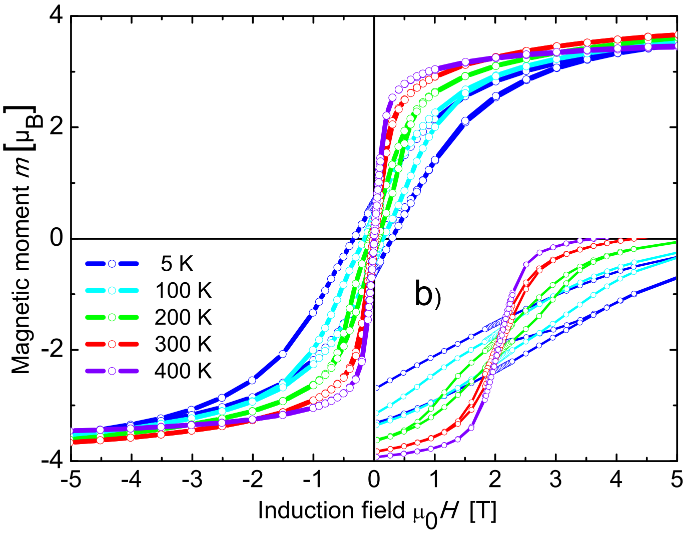

Figure 7.2: Hysteresis of not annealed Fe_2MnGa at different temperatures. The inset b) shows a zoom of the hysteresis to make the magnetic behavior visible.

have measured FC and FH-M (T) curves which show a hysteresis around the transition temperature. A thermal hysteresis between the FC and FH curves is a signature of a first-order phase transition[90]. The transition around 300 K is believed to have a FM-AFM nature. The occurrence of a structural transition appears unlikely, as the room temperature XRD pattern shows only a single phase, where the sample already enters into the transition region. The fact that the ZFC curve measured in 0.1 T shows a considerable magnetization which increases further for FC/FH curves indicates a weak AFM ordering below the transition temperature. To determine the paramagnetic (PM) to FM ordering temperature we have measured the high temperature magnetization as shown in the inset of Fig. 7.3. The sample shows a Curie temperature (T_C) of 750 K. Thus, the high T_C makes the sample interesting for technological applications. The ZFC and FC M (H) loops measured at 2 K are shown in Fig. 7.4. In ZFC mode the sample is cooled to 2 K in zero field, whereas, in FC mode a field of 1 T is applied at 350 K before cooling down to 2 K. Indeed, the low temperature phase shows AFM behavior in the M (T) curves, but no spin-flip type of magnetization change is observed in the M (H) loops. The ZFC M (H) loop shows a hard magnetic behavior. However, since the sample crystallizes in a pseudocubic (Cu_3Au-like) structure the hard magnetic behavior may not be related to the anisotropy in the sample. The spin-flop type of magnetization change of the weak AFM phase that results in a mixed FM/AFM phase at lower field might be responsible for the observation of large coercive fields. The M (H) loop measured at 300 K shows a soft magnetic behavior, which is consistent with the pseudocubic structure, with a slight increase in the magnetization compared to 2 K. It is also found that the M (H) loop does not show any saturation behavior in the magnetic field of 7 T. A magnetization of 3.8 μ_B is observed at 7 T. In a recent work Kudryavtsev et al. have reported a magnetization value of 4.86 μ_B at 2 K for a field of 10 T, where the sample consists of two different cubic phases [86]. The same group also has reported a theoretical magnetization of 6.11 μ_B in the FM metallic fcc phase and 2.03 μ_B in the ferrimagnetic half-metallic phase with $L2_1$ structure [86]. In another work Tang et al. have reported a magnetization of around 2.5 μ_B at 5 K in the melt spun ribbons γ-Fe_2MnGa [87]. However, all these studies show the existence of a FM-AFM transition around room temperature. The non-saturation behavior of the M (H) loop in the present case indicates that either the sample contains significant amount of the AFM phase even at 7 T or a small canted moment due to the presence of anti-site disorder in the sample.
For a further study about the possibility of phase coexistence in this compound, we have measured FC M (H) loops after field cooling in various fields. The loop measured after 1 T field cooling is shown in Fig. 7.4. The FC loops measured in different cooling fields show a significant increase in coercive field as compared to the ZFC loop. The increase in coercive field and the loop shifting are signatures of the presence of an exchange bias in the system [91]. Hence, the presence of EB clearly indicates that there must exist mixed FM and AFM phase in the sample. To understand the origin of the EB in the system, we have measured hysteresis loops at 2 K after cooling the sample in different fields. All the measurements are performed for fields of ±7 T. H_{EB} and H_C are calculated using $H_{EB} = -(H_1 + H_2)/2$ and $H_C = |H_1 - H_2|/2$, where H_1 and H_2 are the lower and upper cut-off fields at which the magnetization becomes zero. The variation of H_{EB} and H_C

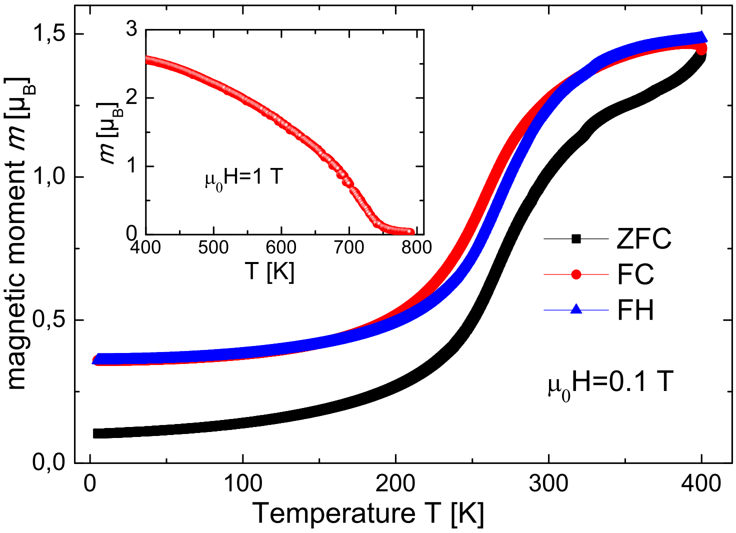

Figure 7.3: Temperature dependence of magnetization, M (T), measured in a field of 0.1 T. The inset shows M (T) measured in the temperature range of 400 K-800 K in presence of a field of 1 T.

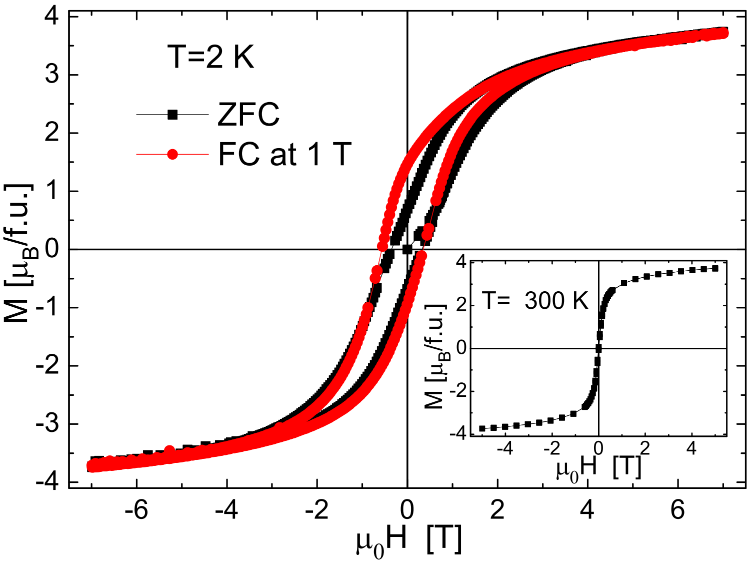

Figure 7.4: Field dependence of the magnetization, M (H), measured at 2 K in ZFC and FC mode. The inset shows M (H) measured at 300 K.

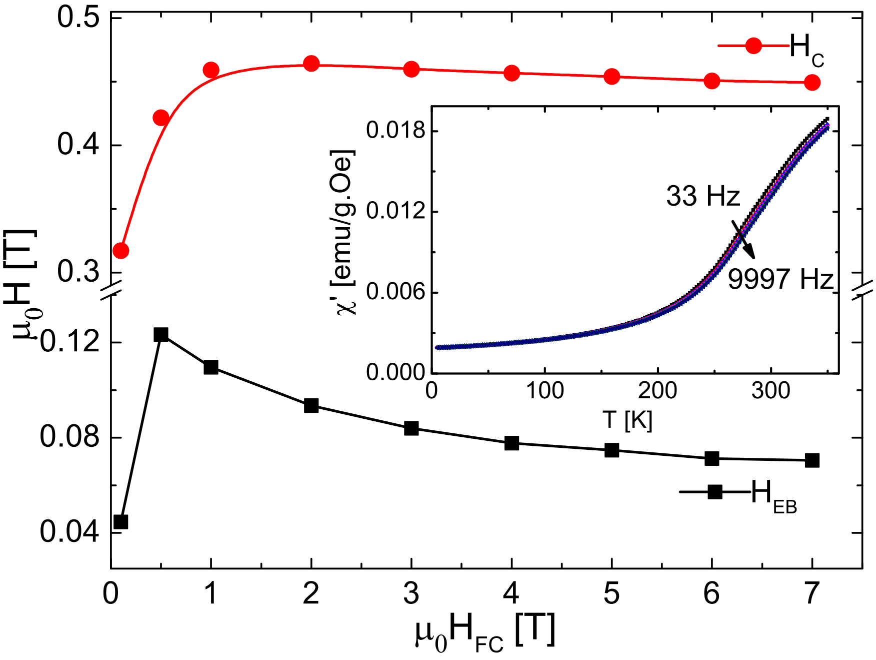

Figure 7.5: Exchange bias field (H_{EB}) and coercive field (H_C) measured at 2 K after field cooling the sample in different fields. The inset shows real part of the ac-susceptibility measurement (χ') [92] measured in different frequencies with amplitude 5 Oe.

with the cooling field is shown in Fig. 7.5. It has been found that for lower cooling field both H_{EB} and H_C increase to a maximum value before decreasing and tending towards saturation at higher fields. The H_{EB} attends a maximum value of 0.12 T at a cooling field of 0.5 T, which saturates to 0.07 T at a field of 7 T. Similarly, H_C attends a maximum value of 0.46 T at a field of 1 T that decreases slowly to 0.45 T at a cooling field of 7 T. The increase in the H_C mainly comes from the exchange interaction between the AFM and FM domains[91]. With an increase in the cooling field a higher amount of the AFM phase converts to the FM one, that helps in decreasing H_C (see Fig. 7.5). The increase in H_{EB} at lower field is due to the formation of large AFM and FM domains that leads to a large number of interfaces, which gives a maximum exchange interaction between the two phases. With increase in the cooling field the FM phase grows at costs of the AFM phase. The decrease in size of the AFM phase leads to a decrease in the exchange interaction which eventually gives a less H_{EB}. The H_{EB} shows a saturation behavior at very high field as the amounts of FM and AFM phase stay almost unchanged. It can be mentioned here that many Heusler alloys show EB behavior due the presence of a spin-glass type of magnetic state [84, 93, 94]. Therefore, we have performed ac susceptibility measurements at different frequencies, which is shown in the inset of Fig 7.5. However, whereas the FM-AFM transition is clearly visible around 300 K in the $\chi^{'}$ versus T plot, no frequency dependency is observed in the low temperature regime. The real or in-phase susceptibility ($\chi^{'}$) is the most useful feature of an AC spectrometer. It is the slope of a magnetic curve M (H) namely (dm/dH), which is very sensitive to thermodynamic phase changes, hence, it will be used to measure transition temperatures [92]. This rules out any spin-glass type of magnetic state. Hence, the EB arises mainly from the presence of the AFM phase mixed with some amount of FM phase. The origin of AFM phase comes from the first-order FM-AFM transition in this compound.

7.3.3 Mössbauer results

In this section are given the results of Mössbauer measurements of Fe_2MnGa within the temperature range 300 K–120 K carried out in backscattering mode. In addition a comparison between the backscattering and CEM spectra is given. Often it was mentioned that Mössbauer spectroscopy is a microscopic and powerful technique to obtain the local magnetic properties, that is why we use this advantage which allows us a detailed discussion about the magnetic properties of this compound. The Mössbauer spectra performed at 300 K show two components, one magnetic part displayed as a broad sextet and a smaller essentially nonmagnetic component given by a broadened singlet (see,Fig. 7.6). The broad sextet (82%) is assigned to a majority fraction of Fe atoms, which are magnetically ordered at 300 K. It can be decomposed into two sextets with the average hyperfine fields H_{hf}=205(1) kOe ($m \approx 1.6\,\mu_B$) and H_{hf}=101(2) kOe ($m \approx 0.8\,\mu_B$), respectively. Their intensities are given in Table 7.1. As previously (see, chapter Fe_2YZ), we assume that 125 kOe corresponds to $1\,\mu_B$. The hyperfine field of the nearly non-magnetic part represented by a broad singlet is found to be 13.8(6) kOe. To establish the correlation between the magnetic data and Mössbauer results, especially to clarify the magnetization M(T) hysteresis revealed in the temperature range 300 K-200 K as

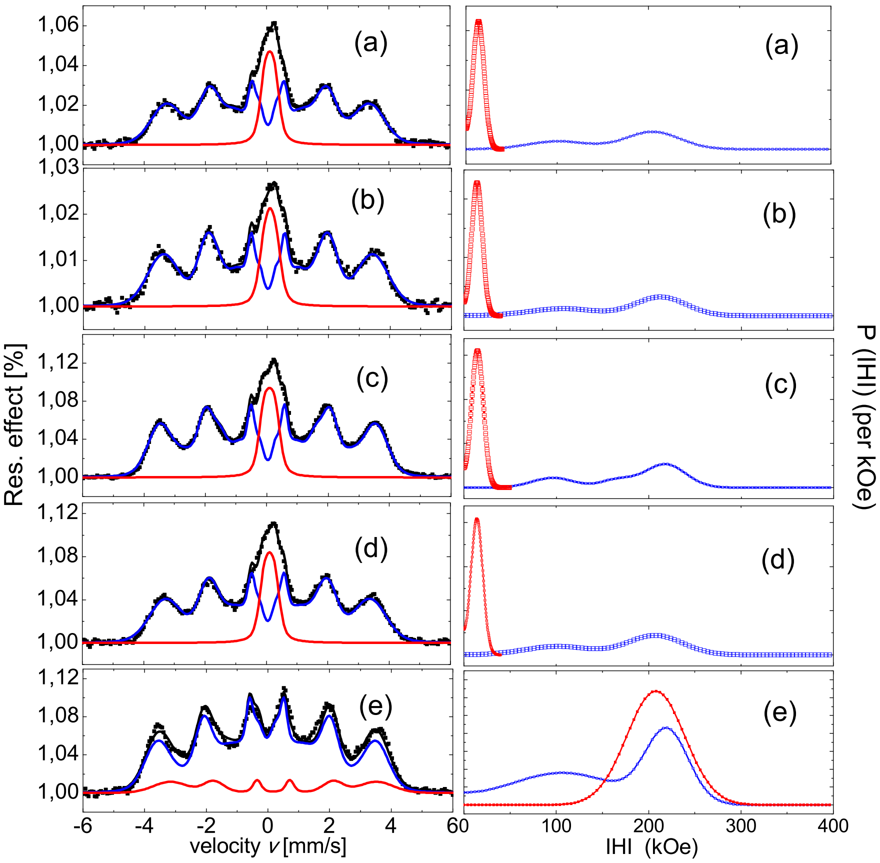

Figure 7.6: Backscattering Mössbauer spectra of Fe_2MnGa not annealed at 300 K (a), 250 K (b), 200 K(c), 150 K (d) and 120 K (e). Right:$|H_{hf}|$ distributions obtained from the spectra on the left.

Table 7.1: Mössbauer data of Fe_2MnGa not annealed. p gives the weight of the component (sum of p's is 1) [33].

Mössbauer spectrum at	p [%]	H_{hf} [kOe]	A [%]	QS [mm/s]	CS [mm/s]	μ_{Fe} [μ_B]
300 K	67	205(1)	82	0	0.044(4)	1.6
	34	101(2)		0	0.044(4)	0.8
		14(1)	18	0	0.103(4)	
250 K	66	212(1)	85	0	0.020(1)	1.7
	34	101(3)		0	0.020(1)	0.8
		15(1)	15	0	0.090(1)	
200 K	59	218(1)	84	0	0.029(3)	1.7
	25	96(3)		0	0.029(3)	0.8
	16	166(3)		0	0.029(3)	1.3
		15(1)	16	0	0.085(4)	
150 K	66	207(2)	84	0	0.046(6)	1.7
	34	101(3)		0	0.046(6)	0.8
		14(5)	16	0	0.102(5)	
120 K	53	107(5)	87	0	-0.036(9)	0.9
	47	220(1)		0	-0.036(9)	1.8
		208(1)	13	0	0.178(4)	1.7

well as the change from soft to hard magnetic behavior, Mössbauer measurements below 300 K have been performed. Above, it was assumed that there is a FM-AFM transition below 300 K which is not accompanied by a structural phase transition. The latter clue is supported by absence of any quadrupole splitting in the Mössbauer spectra. Mössbauer spectra in the temperature range from 300 K to 150 K are very similar and reveal only a minimal change of the H_{hf} distribution. The minority non-magnetic signal with approximately 15% area fraction remains unchanged in the Mössbauer measurement at 150 K. However, it is fully replaced by a magnetic pattern at 120 K. A plot of the temperature dependence of the average hyperfine magnetic field of the main magnetic sextets in the temperature range 300 K to 120 K shows an unusual anomaly of $\langle H_{hf} \rangle$ with a maximum near 200 K, which is not expected from the conventional Brillouin (see, Fig. 7.7) curve. However, this anomaly does not correlate with the experimentally observed decrease of magnetization below 300 K (see, fig 7.4) and suggests a certain decrease of the average magnetic moments associated with Fe atoms in the range of the magnetic anomaly below 200 K. Based on the fact that the magnetic order at 300 K is ferromagnetic, one may suggest that other magnetic atoms (Mn) involved in the magnetic exchange pathway, change their magnetic orientation to the opposite one. This behavior may be releated to the effective decrease of the magnetic moments of the Fe-atoms (see, Fig. 7.7). In the absence of an external magnetic field it is not possible to conclude about the type of magnetic order from Mössbauer spectra. But the anomaly in H_{hf} may point to a change in the magnetic structure. Considering the magnetic data a change from a ferromagnetic to a weak antiferromagnetic spin structure is likely.

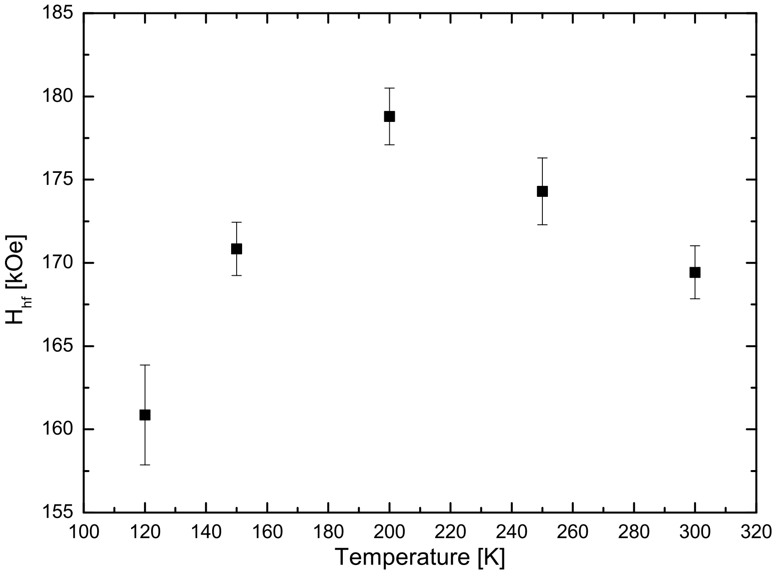

Figure 7.7: Temperature dependence of the average hyperfine field in Fe_2MnGa for the magnetically ordered majority component.

In contrast to conventional transmission or backscattering Mössbauer spectroscopy detecting γ rays of energy 14.4 keV, in CEMS the Mössbauer signal is detected via conversion electrons of an energy of 6 keV. The signal arises mainly from the surface depth of about 100 nm. Fig. 7.8 represents one spectrum of Fe_2MnGa not annealed measured by CEMS (a) and one spectrum resulting from the backscattering Mössbauer mode (b) at 300 K. There is a distinct difference between the spectra. The CEM spectrum of Fe_2MnGa revealed only one nonmagnetic component (CS=0.1505(3) mm/s; QS=0.494(9) mm/s; H_{hf}=12.6(4) kOe) unlike the Mössbauer spectrum for bulk samples in backscattering mode, where the sample clearly yields a major magnetically ordered phase, in agreement with the high magnetic moment of the sample. From the CEMS results we conclude that at the surface a structurally distorted ($QS \neq 0$) non-magnetic phase is enriched compared to the bulk.

7.4 Fe_2MnGa-rolled

7.4.1 XRD characterization

Figure 7.9 illustrates the diffraction pattern of Fe_2MnGa not annealed but rolled. According to the XRD pattern the sample exhibits a single phase. The diffraction pattern again was described using a pseudocubic (Cu_3Au-like) structure model (I4/mmm). However, an increase of the intensity of the peak (220) made a Rietveld refinement difficult. The reason for this is a pronounced texture effect, since the sample was rolled and measured in a disc shaped sample. Since all the XRD measurements of Fe_2MnGa treated in

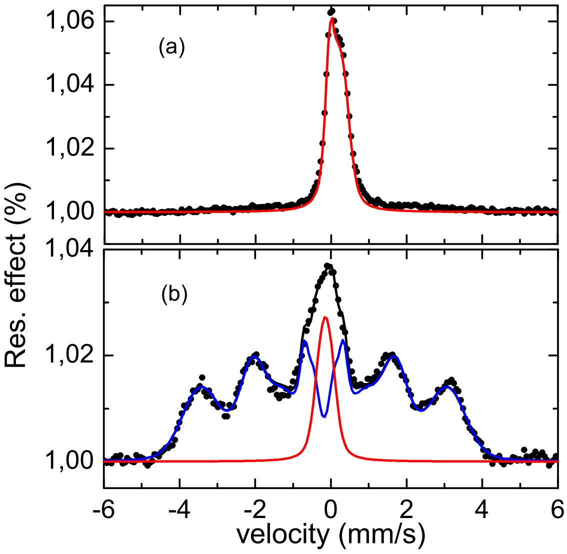

Figure 7.8: Comparison of CEM spectrum (a) and backscattering Mössbauer spectrum at 300 K (b) of Fe_2MnGa not annealed.

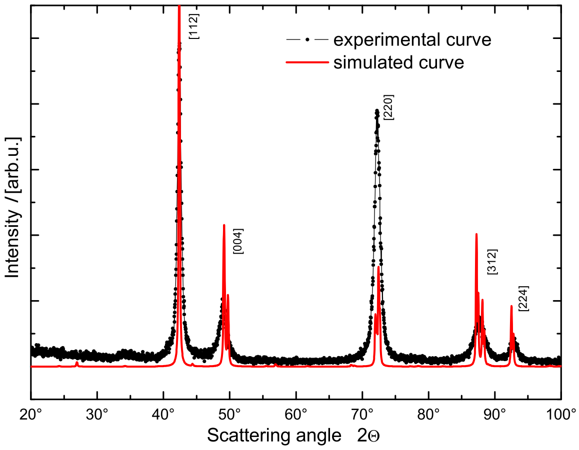

Figure 7.9: Diffraction pattern of Fe_2MnGa-rolled. The diffraction pattern (red) gives the simulated curve (I4/mmm) for Fe_2MnGa, whereas the diffraction pattern (black) shows the experimental curve. The measurement was carried out at room temperature using excitation by Cu-$K_{\alpha 1}$.

different conditions show a similar pattern, we assume that the crystallographic structure of this compound would be also the pseudocubic one. The lattice parameters used for the simulation curve are a=3.7020 Å and c=7.3763 Å.

7.4.2 Magnetic properties

For the rolled sample also magnetic measurements were performed at different magnetic fields. The hysteresis curves at 300 K and 5 K are shown in Figure 7.10. From the m (T) plot (see, Fig. 7.10) T_C is determined to be ≈ 720 K, which is somewhat lower than that of the as grown sample (T_C=750 K). The magnetic moment at room temperature derived from the hysteresis measured at 300 K gives the value of 1.75 μ_B at 5 T, which is much smaller than the corresponding value 3.6 μ_B for the not rolled sample. With decreasing the temperature also the rolled sample becomes hard magnetic, as we can see from the hysteresis measured at 5 K. A total magnetization saturation is not achieved. The reason for this could be a considerable fraction of AF phase. Figure 7.11 summarizes the measurements of the temperature dependence of magnetization M (T) at different fields. According to the literature [87, 95], temperature dependent magnetization - curves as shown in Figure 7.11(inset), may correspond to a martensitic phase. However, such a phase is always accompanied by a structural transition. In the present case a

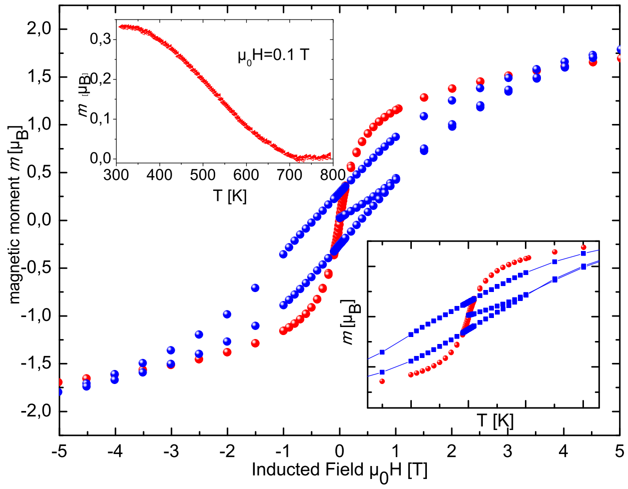

Figure 7.10: Hysteresis curves of the rolled Fe_2MnGa not annealed at 300 K (red) and at 5 K (blue). The inset (left) gives the Tc, whereas the inset (right) gives the zoom of the hysteresis to make the magnetic properties visible. H_C amounts to 0.4 T, whereas the remanent magnetization is 0.3 μ_B/f.u.(see, hysteresis curve-blue).

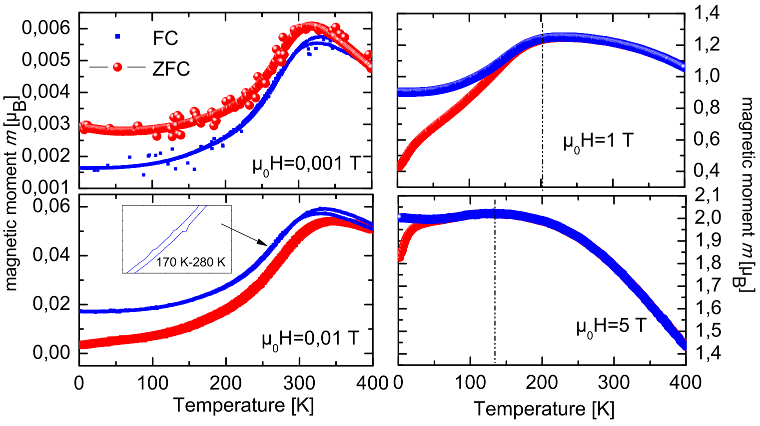

Figure 7.11: Magnetic measurements of rolled Fe_2MnGa not annealed.

Table 7.2: Mössbauer data of Fe_2MnGa not annealed but rolled.

Mössbauer spectrum at	H_{hf} [kOe]	A [%]	QS [mm/s]	CS [mm/s]	μ_{Fe} [μ_B]
300 K	19 (1)	81	0	0.104(5)	0.2
	115 (7)	19	0	-0.015(2)	0.9
200 K	21 (1)	74	0	0.033(4)	0.2
	103 (4)	26	0	0.010(2)	0.8
150 K	45 (3)	37	0	-0.024(4)	0.4
	96 (3)	63	0	0.056(4)	0.8
120 K	143 (5)	59	0	0.010(4)	1.1
	62 (5)	41	0	0.045(4)	0.5
80 K	158 (3)	59	0	-0.052(3)	1.3
	70 (5)	41	0	0.029(3)	0.6

structural transition was considered unlikely due to an absence of a quadrupole splitting obtained from the Mössbauer results. Furthermore, the M (T) performed at 1 T and 5 T represents a shifting of the transition temperature to lower temperatures. Increase of the magnetic field possibly leads to a partial transformation of AF to FM phase. Therefore the magnetic anomaly becomes less pronounced.

7.4.3 Mössbauer spectroscopy

For a further insight into the magnetic properties of Fe_2MnGa-rolled a Mössbauer spectroscopy study was performed at lower temperatures (300 K-80 K) in transmission mode to determine the ^{57}-Fe hyperfine parameters. The temperature range 300 K-80 K was chosen for comparison with the Mössbauer data of Fe_2MnGa-not annealed. The corresponding Mössbauer spectra are displayed in Figure 7.12 and the results from the fitting are given in Table 7.2. In order to interpret and compare the Mössbauer results of the rolled and not rolled sample, one should mention that above was suggested (see,

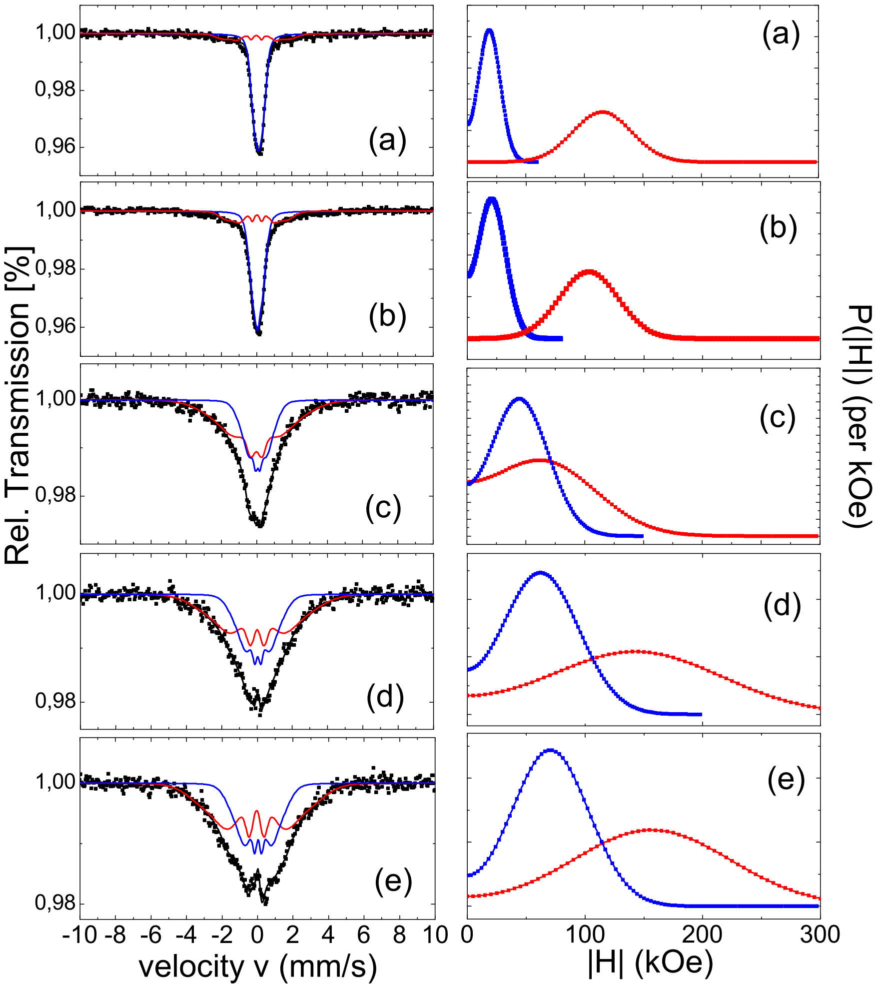

Figure 7.12: Transmission Mössbauer spectra at 300 K (a), 200 K (b), 150 K(c), 120 K (d) and 80 K (e) of Fe_2MnGa-rolled. Right:$|H_{hf}|$ distributions obtained from the spectra on the left.

Fig 7.9) the pseudocubic (Cu_3Au-like) structure for both samples. As for the as-grown sample the Mössbauer spectra over the whole temperature range 300 K-80 K display two components. However, in contrast to the spectra of as-grown Fe_2MnGa, there is a dominant essentially non-magnetic component with an area fraction of 80% in the spectra of the rolled sample measured at 300 K and 150 K. Furthermore the average H_{hf} of the magnetic component is strongly diminished. Magnetic data of the rolled sample showed a significantly smaller magnetic moment ($1.75\,\mu_B$) than Fe_2MnGa not rolled ($3.6\,\mu_B$). This implies that exerting a certain pressure favors the phase, where Fe shows nearly a zero magnetic moment. Mössbauer spectra taken at 300 K can be modeled by a singlet (81%) and a sextet (19%). With decreasing temperature from 300 K to 200 K the intensity ratio between the singlet and the sextet changes slightly from 81% to 76%. A distinct difference of the Mössbauer spectra occurs with decreasing the temperature to 150 K, where the singlet transforms into a sextet. The broad H_{hf} distributions verify the high degree of disorder in the material. Below 150 K all sites of Fe are magnetically ordered. The Mössbauer spectrum at 120 K is similar to the spectrum recorded at 80 K. Accordingly the non-magnetic phase orders below 200 K. From these data follows that rolling the sample leads to a drastic change of the atomic surrounding of Fe-atoms, which in fact also destroys the magnetic properties of the compound. This is possibly the consequence of a high level of defects which is introduced by the mechanical strain associated with the rolling process.

7.5 Fe_2MnGa annealed at 800 °C

7.5.1 XRD characterization

Similar to the XRD pattern of Fe_2MnGa-not annealed, XRD analysis of Fe_2MnGa annealed at 800 °C suggests a single phase. The Rietveld refinement is shown in Figure 7.13. As it follows, also in this case, a cubic structure corresponding to the Cu_3Au-type shows a mismatch in the peak position (200) (see, Fig. 7.13,a), whereas a pseudocubic structure corresponding to the space group (I4/mmm) agrees well with the peak positions of the experimental curve. The lattice parameter for the cubic structure is found to be a=3.7280(2) Å, whereas the fitting results for the pseudocubic structure are a=3.7034(3)Å and c=7.4740(2) Å. The corresponding ratio c/a gives 2.02.

7.5.2 Magnetic properties

Magnetic data of the sample annealed at 800 °C are shown in Figure 7.14. A soft magnetic behavior at room temperature as well as at low temperatures is evident from the hysteresis at 300 K and 5 K. The coercive field of nearly zero (0.02 T) in 5 K m(H) curve is much smaller than that of the not annealed sample (0.3 T). Magnetic moments are found to be $3.9\,\mu_B$ and $4.3\,\mu_B$, respectively, recorded at 5 T. T_C remains similar (720 K) as in the case of the not annealed sample (750 K). Temperature dependent magnetization curves at 1 T and 5 T are displayed in Figure 7.15 and verify the presence of a low temperature anomaly.

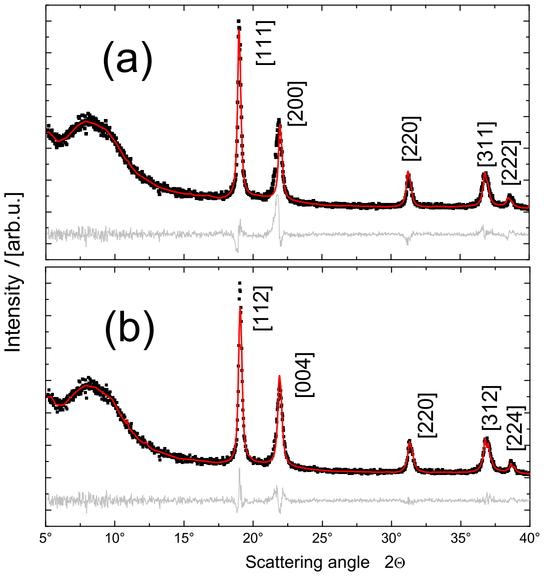

Figure 7.13: Diffraction pattern of Fe$_2$MnGa annealed at 800 °C. The diffraction pattern (red) is compared to the curve fit from the Rietveld refinement (gray). The measurement was carried out at room temperature using excitation by Mo-K$_{\alpha\,1\alpha\,2}$. The Rietveld refinement using the space group Pm$\bar{3}$m is given in a, whereas the Rietveld refinement using the space group I4/mmm is depicted in b.

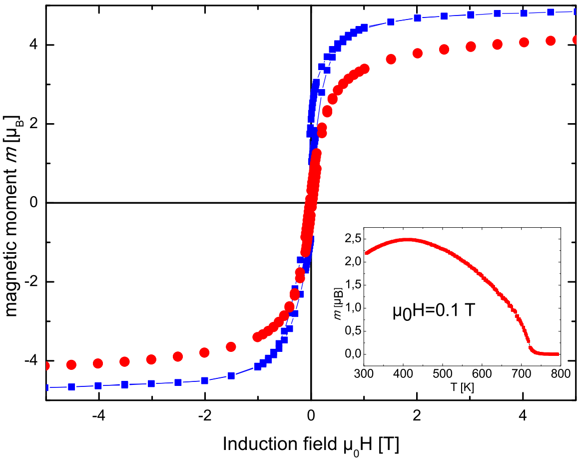

Figure 7.14: Hysteresis curves of Fe$_2$MnGa annealed at 800 °C at 300 K (red) and 5 K (blue). The inset illustrates the Curie temperature (Tc).

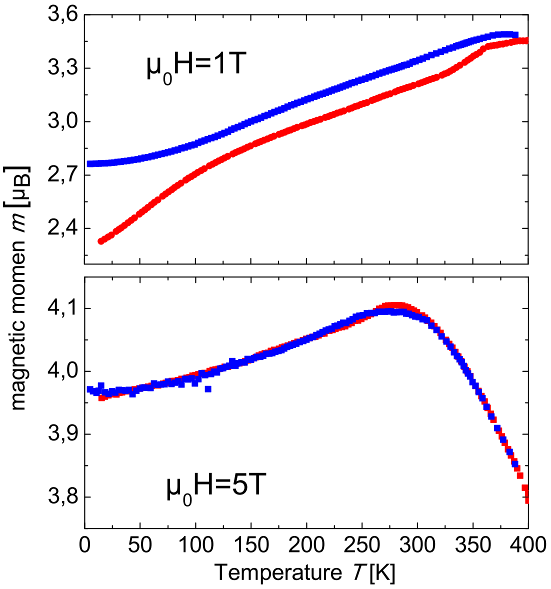

Figure 7.15: Magnetic measurements of Fe_2MnGa annealed at 800 °C at 1 T and 5 T within the temperature range 2 K-400 K.

Table 7.3: Mössbauer data of Fe_2MnGa annealed at 800 °C.

Mössbauer spectrum at	p [%]	H_{hf} [kOe]	A [%]	QS [mm/s]	CS [mm/s]	μ_{Fe} [μ_B]
300 K	64	205 (1)	64	0	0.041(2)	1.6
	36	95 (4)		0	0.041(2)	0.8
		14 (4)	36	0	0.119(4)	
140 K	78	220 (2)	44	0	0.127(6)	1.8
	22	171 (3)		0	0.127(6)	1.4
		77 (1)	56	0	-0.051(1)	0.6

7.5.3 Mössbauer spectroscopy

As in Figure 7.16 displayed, Mössbauer spectra performed at 300 K and 140 K consist of two different components. The Mössbauer spectrum at 300 K has been analyzed using a weakly magnetic component or singlet (36%) and two sextets (64%). The average hyperfine fields of the sextets are H_{hf}=205(1) kOe and 95(4) kOe. The nearly non-magnetic component giving a singlet revealed H_{hf}=14(4) kOe. Decreasing the temperature to 140 K leads to full magnetic order of this component. Accordingly the Mössbauer spectrum at 140 K is described by three broad sextets. The fitting parameters are given in Table 7.3.

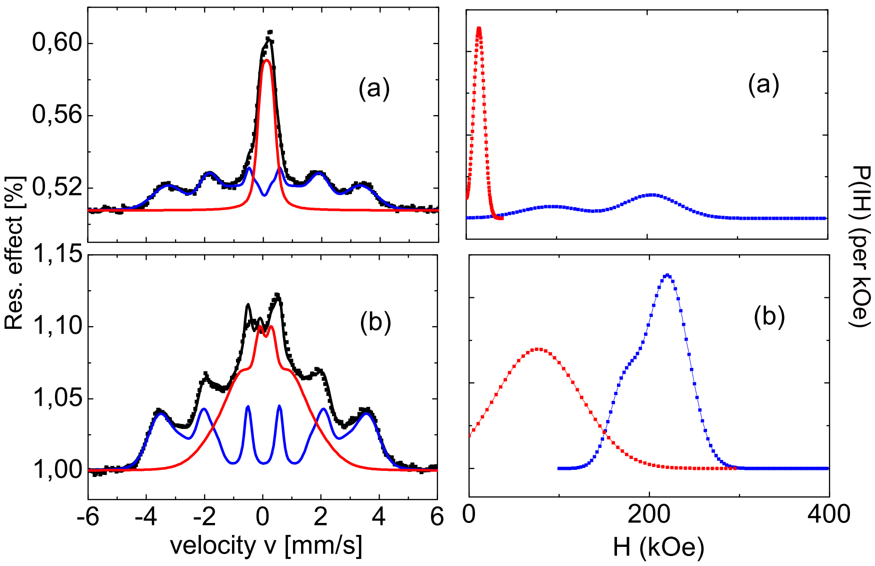

Figure 7.16: Backscattering Mössbauer spectra at 300 K (a) and 140 K (b) of Fe_2MnGa annealed at 800 °C. Right:$|H_{hf}|$ distributions obtained from the spectra on the left.

7.6 Fe_2MnGa annealed at 1100 °C

7.6.1 XRD characterization

XRD analysis of Fe_2MnGa annealed at 1100 °C is shown in Figure 7.17. A Rietveld refinement has been done using a cubic model (Cu_3Au-type) and also a pseudocubic structure (space group I4/mmm). For the cubic structure the lattice parameter is

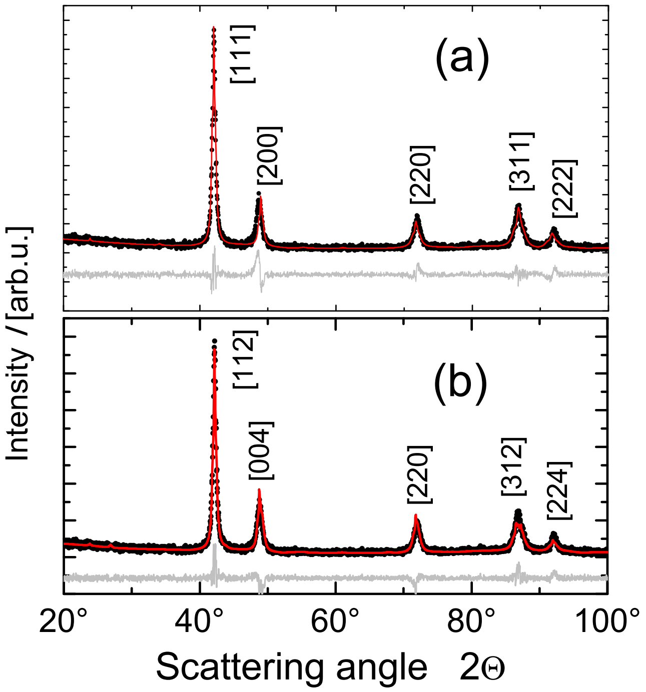

Figure 7.17: Diffraction pattern of Fe_2MnGa annealed at 1100 °C. The diffraction pattern (red) is compared to the curve fit from the Rietveld refinement (gray). The measurement was carried out at room temperature using excitation by Cu-$K_{\alpha 1}$. Rietveld refinement using the space group $Pm\overline{3}m$ is given in a, whereas Rietveld refinement using the space group I4/mmm is depicted in b.

a=3.7230 (2) Å, whereas for the pseudocubic one the lattice parameters are a=3.6993(2) Å and c=7.4609 (1) Å. The corresponding ratio c/a is 2.02. A better agreement of peak positions is found from fitting with the pseudocubic structure.

7.6.2 Magnetic properties

Similar to the as-grown but in contrast to the 800 °C-annealed Fe_2MnGa, the sample annealed at 1100 °C shows a soft magnetic hysteresis at 300 K and a hard magnetic hysteresis at 5 K. Magnetic moments are found to be 3.1 μ_B and 2.9 μ_B, respectively. Fe_2MnGa annealed at 1100 °C revealed a slightly lower magnetic moment and a lower T_C (700 K). The magnetic anomalies revealed from the M (T) measurements at 1 T and 5 T (see, fig. 7.19) remain similar as in the previous samples (see, Figs. 7.11, 7.14).

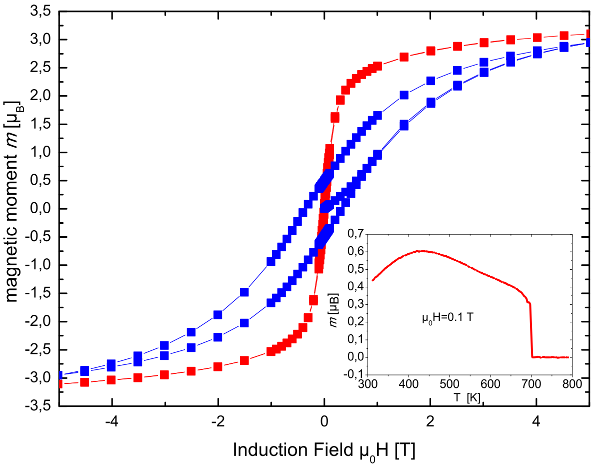

Figure 7.18: Hysteresis curves of Fe_2MnGa annealed at 1100 °C at 300 K (red) and 5 K (blue). The inset illustrates the Curie temperature (Tc). H_C amounts to 0.38 T, whereas the remanent magnetization is 0.56 μ_B/f.u.(see, hysteresis curve-blue).

7.6.3 Mössbauer spectroscopy

Mössbauer spectra of the 1100 °C annealed sample are displayed in Figure 7.20. The fitting results are given in Table 7.4. The Mössbauer spectra essentially follow the same scenario as the other samples. The spectra recorded at 300 K reveal a magnetic and an essentially non-magnetic signal, the latter being the dominant one. The H_{hf} distribution of the "nonmagnetic" component is much broader than in the other cases (see, Fig 7.20, Fig 7.16, Fig 7.6). Decreasing the temperature to 140 K, all sites of Fe are magnetically ordered. The broad sextets again demonstrate the high degree of disorder.

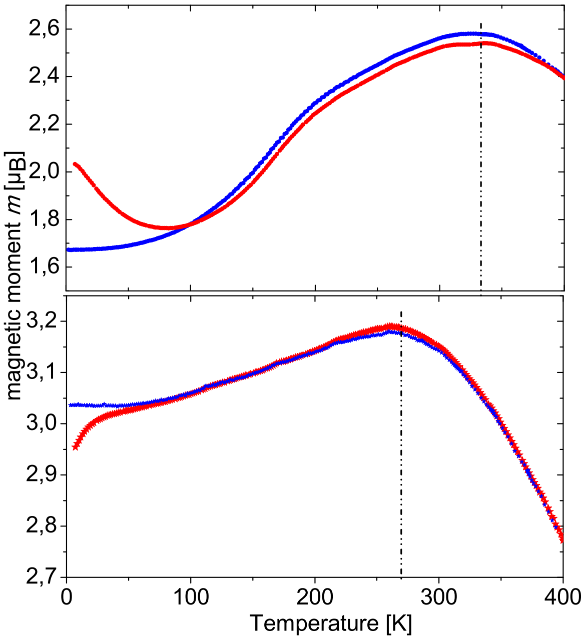

Figure 7.19: Magnetic measurements of Fe_2MnGa annealed at 1100 °C at 1 T and 5 T within the temperature range 2 K-400 K. With a dashed line is marked the shift of the transition temperature to the lower temperature with increasing the magnetic field.

Table 7.4: Mössbauer data of Fe_2MnGa annealed at 1100 C.

Mössbauer spectrum at	p [%]	H_{hf} [kOe]	A [%]	QS [mm/s]	CS [mm/s]	μ_{Fe} [μ_B]
300 K		30 (1)	61	0	0.114(2)	0.2
	62	161 (1)		0	-0.180(5)	1.3
	38	219 (4)	39	0	-0.180(5)	1.8
140 K	51	230 (7)	41	0	0.078(3)	1.8
	49	180 (7)		0	0.078(3)	1.4
		73 (3)	60	0	0.131(3)	0.6

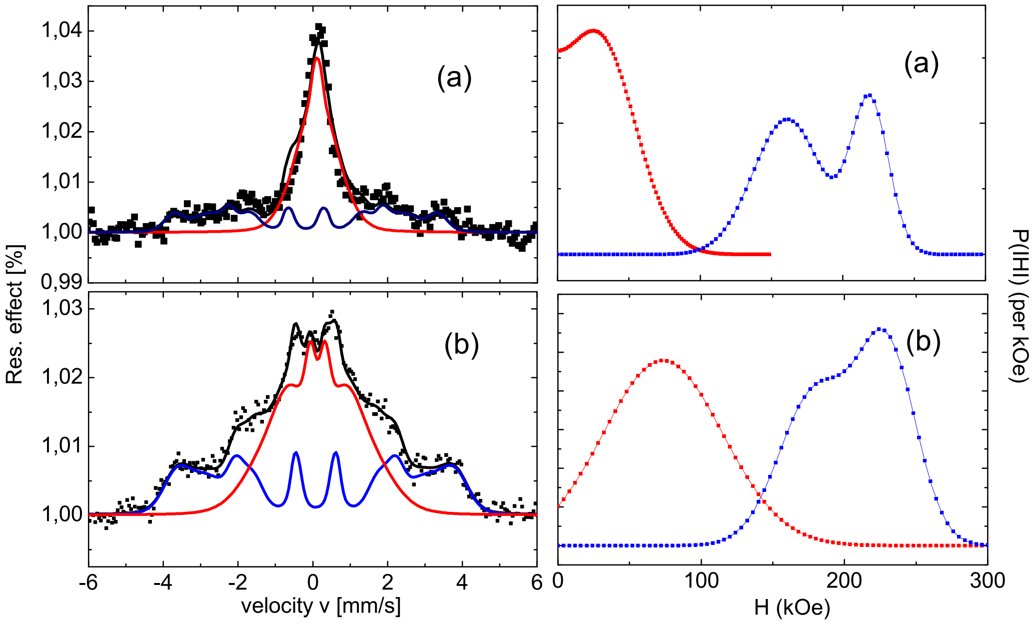

Figure 7.20: Backscattering Mössbauer spectra at 300 K (a) and 140 K (b) of Fe_2MnGa annealed at 1100 °C. Right: $|H_{hf}|$ distributions obtained from the spectra on the left.

7.7 Conclusions

In conclusion, we have synthesized the bulk Fe_2MnGa Heusler compound and characterized it by various techniques. Emphasis was on the as-grown sample without further annealing. For further elucidating the relation between crystal structure, bulk magnetic properties and microscopic phase-behavior we have investigated the influence of mechanical treatment and annealing conditions on the properties. Whereas the XRD patterns are very similar for all the materials and may be described by the pseudocubic Cu_3Au-like structure model in all the cases, the magnetic properties and the Mössbauer spectra are considerably different. In all the cases the Mössbauer spectra at room temperature can be described by the superposition of a non-magnetic and a magnetic signal, the intensity ratio of which depends on annealing conditions and mechanical treatment. The non-magnetic fractions order below 200 K. Mechanical treatment and annealing conditions influence the defect level and the detailed local arrangement of the atoms which determines the magnetic properties. The coexistence of different species in the Mössbauer spectra may point to a phase separation on the microscale. The broad hyperfine patterns evidence the high degree of disorder in all the samples. In agreement with the Mössbauer spectra this suggests high level of Mn/Fe disorder.

According to the magnetic data, Fe_2MnGa not annealed sample undergoes a first-order FM-AFM transition, where, disorder in the sample may lead to nucleation centers for this transition. Mössbauer spectra suggest the presence of two distinct phases with different ordering temperatures. The non-magnetic component orders below 150 K. The hard magnetic behavior of the low temperature M (H) curves is related to the spin-flop type of magnetization change of the AFM phase that results in a mixed phase. The sample shows a large EB behavior which mainly originates from the co-existence of FM and AFM phases below the FM-AFM transition temperature. The existence of a large T_C with large EB behavior make the sample as a potential material for magneto-electronics applications.

8 Magnetic and structural properties of $Mn_{3-x}Rh_xSn$

8.1 Introduction

Currently, very attractive Heusler alloys are those that are suitable for spin torque transfer applications in spintronics i.e. the electron spins influence the magnetization orientation in the ferromagnetic component of GMR (giant magnetoresistance) layers [4]. As a nonmagnetic tunnel barrier Al_2O_3 and MgO have been shown as suitable. Based on this, the ferromagnetic component should possess a certain structure with lattice parameters that match to the lattice parameters of Al_2O_3 and MgO [4.19 Å]. However, as general properties the compounds that may be used for STT, should exhibit a low magnetic moment, low Gilbert damping constant and high spin polarization. A huge number of Heusler alloys [4] has been synthesized and studied trying to find potentially interesting compounds with these features. Furthermore, perpendicular anisotropy was discovered in thin films based on Mn-Heusler compounds. This effect decreases the switching current time [74].
The main idea of this work is to induce a transition in hexagonal Mn_3Sn to a tetragonal structure. It was assumed that to increase the lattice parameters of Mn_3Sn doping with Rh could be realized, as Rh(134 pm) has a larger atomic radii as than Mn(127 pm). However, Mn_3Sn has been found to be hexagonal, and therefore adding a large atom could lead, probably, to the desired tetragonal structure. In fact the tetragonal structure was achieved for certain concentrations of Rh. Above (see, chapter Fe_2MnGa, Mn_2FeGa and $Mn_{3-x}Fe_xGa$) Mn-based materials have been discussed with different concentration of Fe and Ga, and now we extend this subject to the magnetic and structural properties of the series $Mn_{3-x}Rh_xSn$ in a composition range with x=0 - 1. In this series compounds of inverse tetragonal structure with a low magnetic moment were predicted and successfully synthesized. Thus, these alloys could be very interesting for applications in spintronics.

8.2 Synthesis details

$Mn_{3-x}Rh_xSn$ samples were synthesized by repeated arc-melting of stoichiometric amounts of the elements in an argon atmosphere. To avoid oxygen contamination Ti was used as a getter material. The weight loss was less than 0.5%. As-cast samples were annealed at 400 °C for one week to improve the crystal quality and phase purity. Additionally they were quenched in ice/water mixture. Magnetic properties of the powdered sample have been determined using a SQUID (superconducting quantum interference device) within the temperature range 5-400 K. Mössbauer measurements at room temperature and 80 K were carried out using a $Ca^{119m}SnO_3$ source in the transmission mode.

8.2.1 Structural properties

The inverse tetragonal structure was often obtained in Mn-based Heusler compounds [84, 28]. In the present case of Mn-based Heusler compounds, for $Mn_{3-x}Rh_xSn$ (x=0.5-1) the structure was found to be dominating inverse tetragonal (I$\bar{4}$m2, 119), whereas for $Mn_{3-x}Rh_xSn$ (x=0-0.5) the Mn_3Sn phase ($P6_3/mmc$, 194) prevails(see, fig. 8.1). Fig. 8.1 summarizes the diffraction patterns of several selected compounds, which exhibit mainly an inverse tetragonal structure. In addition the hexagonal pattern of Mn_3Sn is shown.

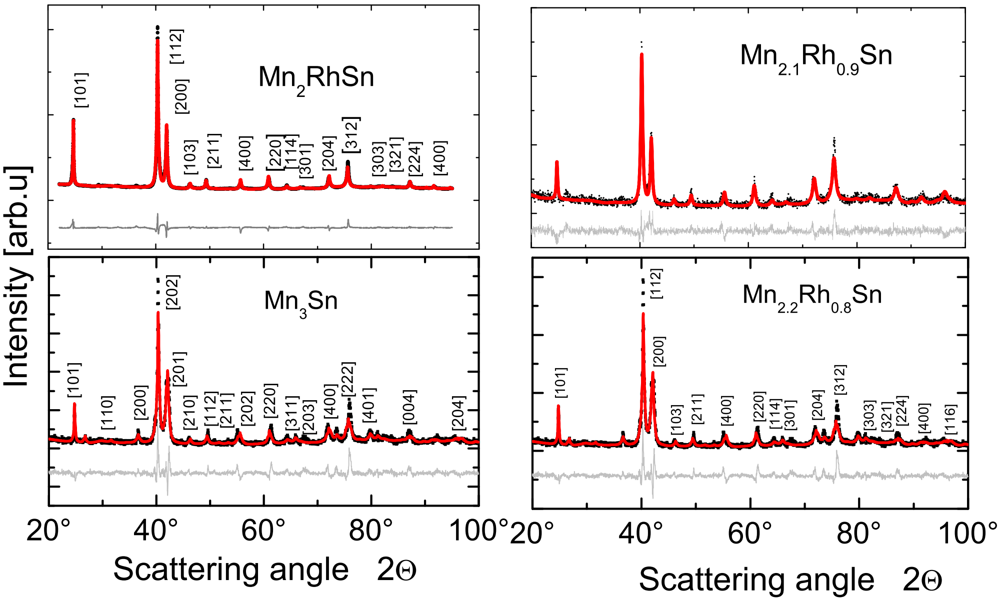

Figure 8.1: Diffraction pattern of $Mn_{3-x}Rh_xSn$ using Cu-Kα_1 excitation. For the XRD pattern of $Mn_{2.2}Rh_{0.8}Sn$ are shown only the peaks attributed to an inverse tetragonal structure.

The obtained results from the Rietveld refinements using the software program Full Prof are listed in Table 8.1. Mn_2RhSn was verified to be without any impurity. Also, $Mn_{2.1}Rh_{0.9}Sn$ shows a high purity, however, one should mention that the XRD pattern of this compound shows small peaks that cannot be attributed to the inverse tetragonal structure (I$\bar{4}$m2). This means that this compound does not show a 100% purity of the Heusler phase. However, $Mn_{2.2}Rh_{0.8}Sn$, $Mn_{2.3}Rh_{0.7}Sn$ and $Mn_{2.4}Rh_{0.6}Sn$ contain in

Table 8.1: The lattice parameters of $Mn_{3-x}Rh_xSn$ alloys annealed at 350 °C for one week. ∗) marks the presence of an undefined impurity phase, whereas a) marks the phase fraction.

compound	a [Å]	c [Å]	c/a ($I\bar{4}m2$)	[%]$^{a)}$ ($I\bar{4}m2$)	a [Å]	c [Å]	c/a ($P6_3$/m m c)	[%]$^{a)}$ ($P6_3$/m m c)
Mn_2RhSn	4.292(2)	6.619(2)	1.54	100	-	-		
$Mn_{2.1}Rh_{0.9}Sn$	4.288(8)	6.622(2)	1.54	100	-	-		
$Mn_{2.2}Rh_{0.8}Sn$	4.296(3)	6.630(2)	1.54	56	5.677(2)	4.539(4)	0.81	44
$Mn_{2.3}Rh_{0.7}Sn$	4.293(2)	6.622(3)	1.54	46	5.675(2)	4.538(2)	0.81	54
$Mn_{2.4}Rh_{0.6}Sn$	4.291(2)	6.613(4)	1.54	53	5.665(4)	4.531(3)	0.81	47
$Mn_{2.5}Rh_{0.5}Sn$	-	-	-$^{*)}$		5.670(7)	4.522(5)	0.81	
$Mn_{2.6}Rh_{0.4}Sn$	-	-	-$^{*)}$		5.666(5)	4.532(4)	0.81	
$Mn_{2.7}Rh_{0.3}Sn$	-	-	-$^{*)}$		5.671(4)	4.535(3)	0.81	
$Mn_{2.8}Rh_{0.2}Sn$	-	-	-$^{*)}$		5.667(4)	4.532(3)	0.81	
$Mn_{2.9}Rh_{0.1}Sn$	-	-	-$^{*)}$		5.668(4)	4.533(3)	0.81	
Mn_3Sn	-	-	-$^{*)}$		5.664(6)	4.530(4)	0.81	

addition to the tetragonal phase also the Mn_3Sn phase. From $Mn_{2.5}Rh_{0.5}Sn$ to Mn_3Sn just the hexagonal structure is found. These compounds ($Mn_{2.5}Rh_{0.5}Sn$ to Mn_3Sn) consist also of another phase that unfortunately could not be defined (Table 8.1, ∗-marked). Table. 8.1 demonstrates that increasing the amount of Rh the fraction (%) of the inverse tetragonal phase increases. The extracted lattice parameters for Mn_2RhSn are a=4.292(2) Å and c=6.619(2) Å (c/a=1.54) and those for Mn_3Sn-phase are found to be a=5.664(6) Å and c=4.530(4) Å (c/a=0.81). As mentioned above, materials with the lattice parameters of 4.03 Å are required to be structurally compatible with MgO.

8.2.2 Magnetic properties

Magnetic properties determined in the temperature range 5-400 K are illustrated in Figures 8.2 and 8.3. Hysteresis curves of $Mn_{3-x}Rh_xSn$ series do not show a magnetic saturation, hence, the magnetic moments given in Table 8.2 are recorded at 5 T. $Mn_{3-x}Rh_xSn$ (x=0.6-1) samples, which exhibit mainly an inverse tetragonal phase (space group: 119, $I\bar{4}m2$) revealed a higher magnetic moment at 300 K in contrast to those samples occurring mainly in the hexagonal structure (space group no: 194, $P6_3/mmc$). These samples show at room temperature a soft magnetic behavior, whereas at low temperatures (for instance at 5 K) they become hard magnetic. Decreasing the temperature increases the magnetic moment, which is consistent with an increasing Rh amount. However, an increase of the Rh amount from $Mn_{2.4}Rh_{0.6}Sn$ to Mn_2RhSn leads to higher magnetic moments, which possibly corresponds to an increasing amount of ferrimagnetic phase [21]. Samples with a hexagonal structure do not show any changes concerning the magnetic moment from 300 K to 5 K. Due to enhanced values of magnetic moments and hardness, the compounds $Mn_{3-x}Rh_xSn$ with (x=0.6-1) are in the main focus of this work. In this series, Mn_2RhSn shows interesting and unusual magnetic properties, however, further investigations are the subject of another work [96], that is why in this work detailed discussions about this sample will not be given. Magnetic moments and T_C or T_N, respectively are listed in the Table 8.2. As it follows, the $1/\chi$-curves (see, Fig 8.3)

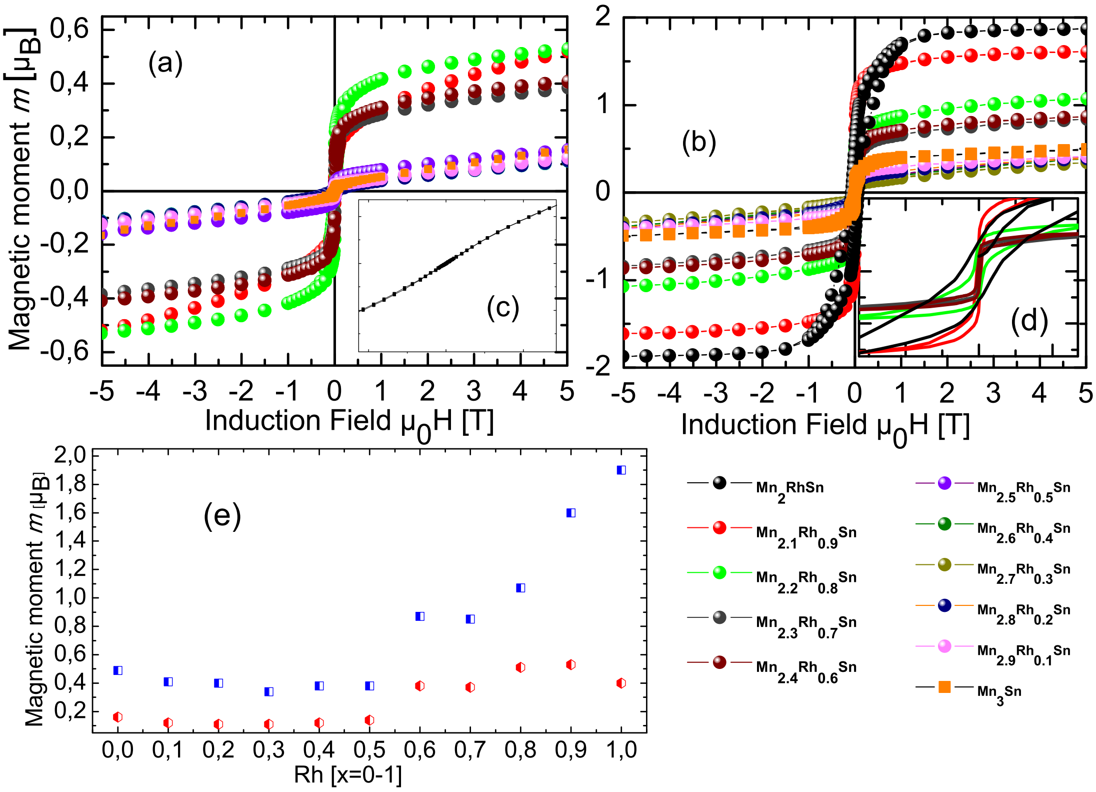

Figure 8.2: Magnetic properties of $Mn_{3-x}Rh_xSn$. The M(H)-curves were measured at 300 K (a) and 5 K (b). The summary of magnetic moments at 300 K(red) and 5 K (blue) recorded at 5 T is shown in Figure e). The inset c) and d) shows a zoom of the hysteresis at 300 K of Mn_2RhSn and 5 K of $Mn_{2.5-x}Rh_xSn$ for x=0-0.5, to make magnetic behavior visible.

confirm also the occurrence of two phases due to the two drops of magnetization.

8.2.3 Mössbauer study

In this chapter ^{119}Sn Mössbauer studies allow the detailed insight into the order/disorder phenomena in $Mn_{3-x}Rh_xSn$. This is important to be clarified, since it strongly influences the physical properties of Heusler compounds. To elucidate features of the magnetic state, the Mössbauer spectra were taken at 300 K and 80 K. One can conclude about magnetic properties due to the hyperfine magnetic fields resulting from the induced magnetism at the ^{119}Sn nuclei. Inequivalent sites of Mössbauer atoms lead to a distribution of the hyperfine fields. The Mössbauer spectra performed at room temperature are presented in Figure 8.4. In general, the spectra can be described by two principal components. To conclude about chemical bonding, the crystal symmetry and the values of the induced magnetic field at Sn-nuclei in $Mn_{3-x}Rh_xSn$, the CS [mm/s],

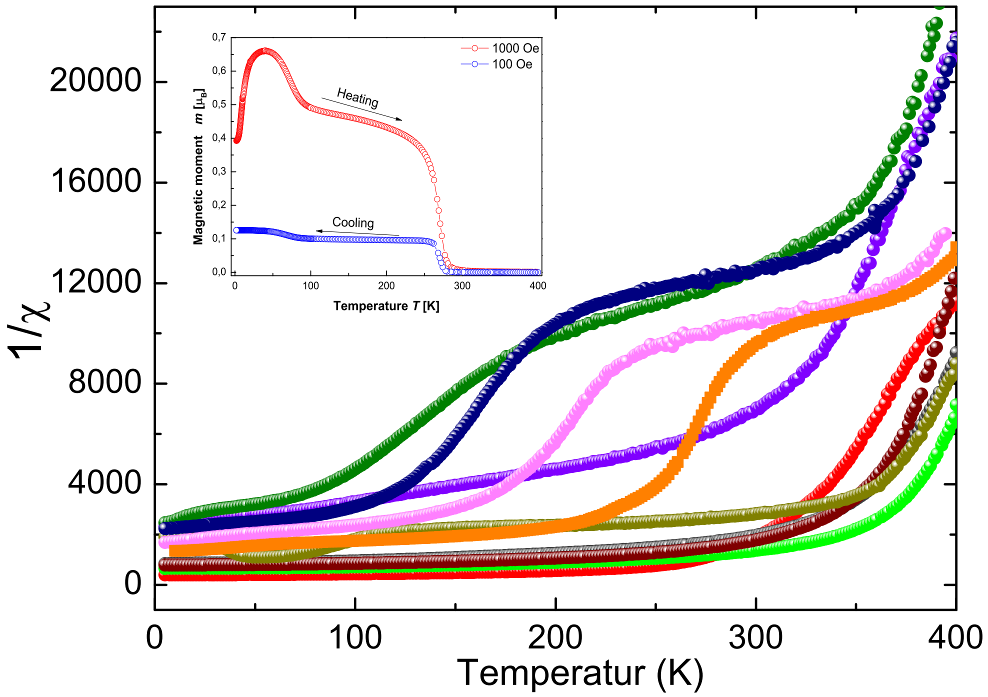

Figure 8.3: Magnetic properties of $Mn_{3-x}Rh_xSn$. The $1/\chi$-curves were measured within the temperature range of 400 K-2 K. The inset gives M(T)-measurements of Mn_2RhSn under magnetic fields of 100 Oe and 1000 Oe. The corresponding color to each compound is shown in Figure 8.2.

the QS [mm/s] and H_{hf}[kOe] within the concentration range [x=0 - 1] are given in Table 8.3. As it follows from the XRD-data, Mn_2RhSn appears in the inverse tetragonal structure, where Sn is surrounded by 8-Mn atoms and 4-Rh atoms in the first coordinations sphere. According to the magnetic data, Mn_2RhSn is weak magnetically ordered at room temperature and therefore a weak magnetic splitting in the Mössbauer spectrum was observed (H_{hf}=5.53(13) kOe). The Mössbauer results at 80 K demonstrate a distinct difference to the data obtained at room temperature. A further investigation of Mn_2RhSn is given in Reference [96]. The high magnetic moment at low temperatures and the hard magnetic behavior of this compound have been further supported by Mössbauer measurements, which revealed a high magnetic field at the Sn atoms. The main component of the magnetically split spectrum with relative intensity of 90% indicates strong degree of anti site disorder, firstly because of the occurrence of more than

Table 8.2: Magnetic moments and T_C or T_N, respectively, of $Mn_{3-x}Rh_xSn$.

$Mn_{3-x}Rh_xGa$	m at 300 K [μ_B]	m at 5 K [μ_B]	T_C or T_N [K]
Mn_2RhSn	0.40	1.90	290
$Mn_{2.1}Rh_{0.9}Sn$	0.53	1.60	295
$Mn_{2.2}Rh_{0.8}Sn$	0.51	1.07	343
$Mn_{2.3}Rh_{0.7}Sn$	0.37	0.85	329
$Mn_{2.4}Rh_{0.6}Sn$	0.38	0.87	340
$Mn_{2.5}Rh_{0.5}Sn$	0.14	0.38	285
$Mn_{2.6}Rh_{0.4}Sn$	0.12	0.38	284
$Mn_{2.7}Rh_{0.3}Sn$	0.11	0.34	329
$Mn_{2.8}Rh_{0.2}Sn$	0.11	0.40	288
$Mn_{2.9}Rh_{0.1}Sn$	0.12	0.40	230
Mn_3Sn	0.16	0.49	420

Table 8.3: Mössbauer data revealed at 300 K of $Mn_{3-x}Rh_xSn$.

$Mn_{3-x}Rh_xGa$	p [%]	H_{hf} [kOe]	CS [mm/s]	QS [mm/s]
Mn_3Sn	68	41.51 (30)	-1,0850 (79)	-0.274 (28)
	32	6*	-1,0850 (79)	-0.274 (28)
$Mn_{2.9}Rh_{0.1}Sn$	89	41.52 (17)	-0,810 (22)	-0.274 (28)
	11	40.66 (28)	-0,810 (22)	-0.274 (28)
$Mn_{2.8}Rh_{0.2}Sn$	86	9.63 (31)	-0,810 (18)	-0.246 (23)
	14	96 (3)	-0,810 (18)	-0.246 (23)
$Mn_{2.7}Rh_{0.3}Sn$	89	38.03 (40)	-0,810 (18)	-0.195 (18)
	11	9.74 (26)	-0,810 (18)	-0.195 (18)
$Mn_{2.6}Rh_{0.4}Sn$	84	38.4 (12)	-0,792 (42)	-0.237 (58)
	16	9.64 (74)	-0,792 (42)	-0.237 (58)
$Mn_{2.5}Rh_{0.5}Sn$	87	30.95 (70)	-0,810 (13)	-0.239 (23)
	13	10.22 (27)	-0,810 (13)	-0.239 (23)
$Mn_{2.4}Rh_{0.6}Sn$	49	108.4 (14)	-0,8306 (49)	0.010 (11)
	51	28.02 (84)	-0,8306 (49)	0.010 (11)
$Mn_{2.3}Rh_{0.7}Sn$	55	8.40 (98)	-0,7447 (22)	-0.263 (20)
	45	23.4 (12)	-0,7447 (14)	-0.263 (20)
$Mn_{2.2}Rh_{0.8}Sn$	76	105.4 (27)	-0,853 (17)	-0.109 (22)
	24	16.5 (22)	-0,853 (17)	-0.109 (22)
$Mn_{2.1}Rh_{0.9}Sn$	41	5.61 (26)	-0,780 (84)	-0.274 (27)
	59	25.4 (39)	-0,780 (84)	-0.274 (27)
Mn_2RhSn	90	5.53 (13)	-0,880 (37)	-0.720 (44)
	10	10	-0,880 (37)	-0.720 (44)

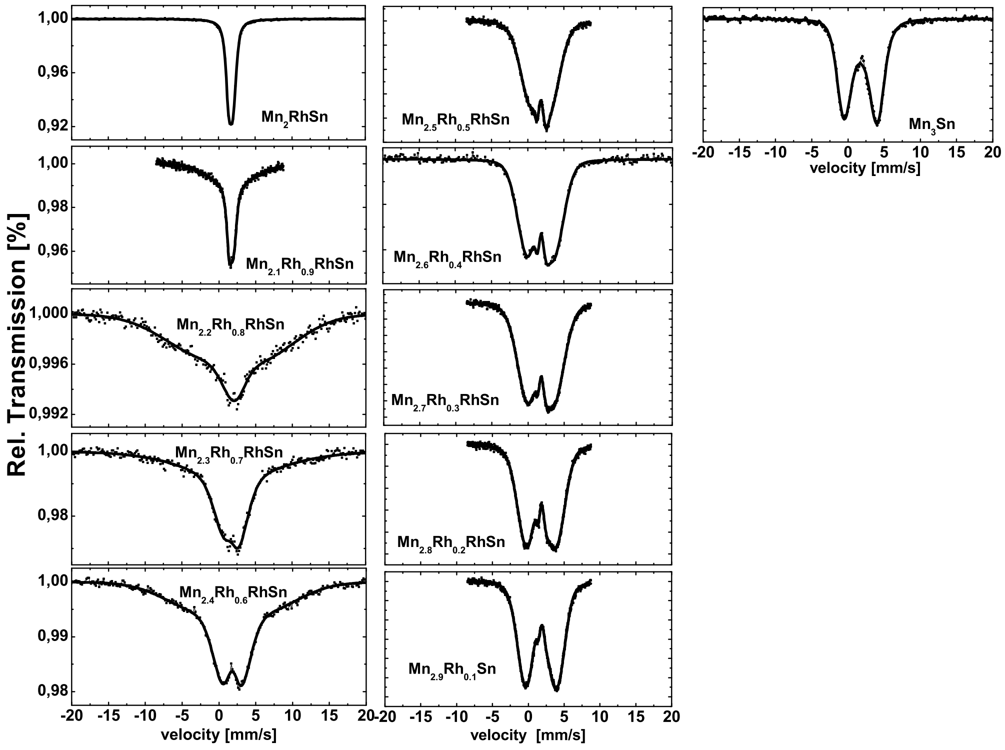

Figure 8.4: Mössbauer spectra of $Mn_{3-x}Rh_xSn$ performed at room temperature in transmission mode.

one position of Sn-atoms and secondly due to the high distribution of H_{hf} reflected in the broad linewidth . The average magnetic field derived from fitting is 120 kOe and the corresponding isomer shift is CS=-0.88(3) mm/s. The fitting demonstrates an absence of the quadrupole splitting. These values are due to the strong shielding of Sn atoms by the eight nearest Mn neighbours [97]. A small amount of a magnetic component (10%) with larger H_{hf} (194(2) kOe) occurs probably because of the anti-site disorder, which could be a consequence of more Rh-atoms in the first coordination sphere of Sn-atoms that destroys the entire antiferromagnetic balance of Mn magnetic moments. Another end -member of this series of compounds, namely Mn_3Sn shows at room temperature a magnetically split spectrum with an average magnetic hyperfine splitting of 39(2) kOe. This is also in agreement with the data given in Ref [97]. Similar to the compounds containing Rh the quadrupole splitting in Mn_3Sn is small [97]. Decreasing the temperature increases the value of the hyperfine magnetic field, which amounts to 46(1) kOe at

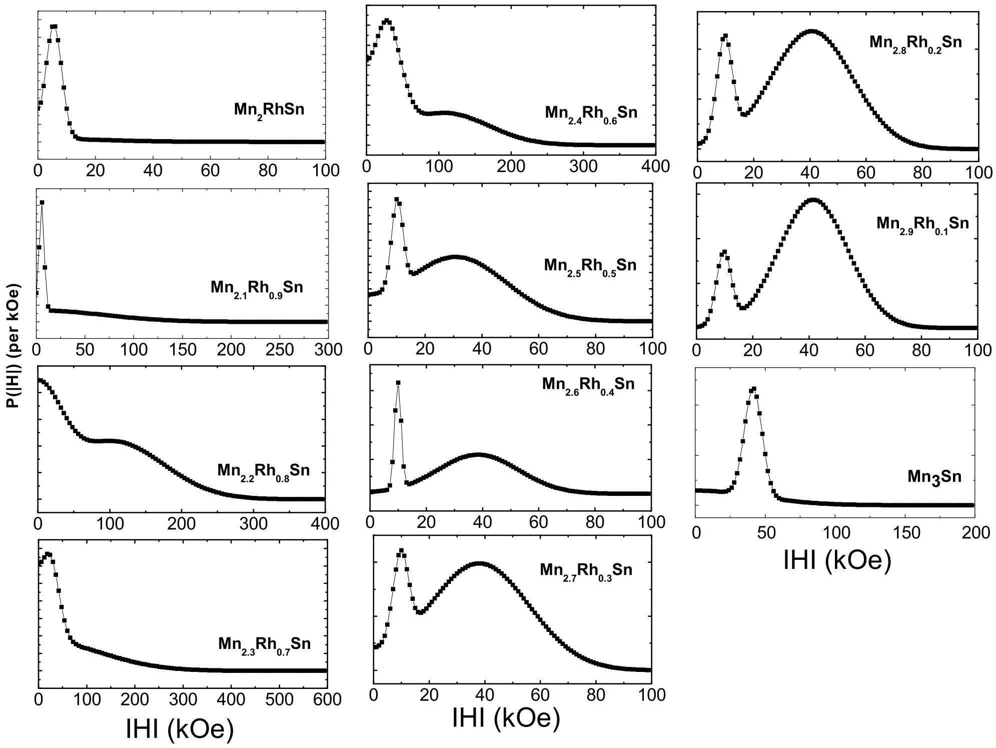

Figure 8.5: $|H_{hf}|$ distributions obtained from the Mössbauer spectra performed at 300 K. $*$) marks a fixed component.

80 K. However, in this case appears a magnetic subspectrum with 16% of relative intensity and a hyperfine magnetic field of 194(2) kOe. Based on earlier publications [97], one could interrelate this subspectrum (16%) with the weak ferromagnetic remanence below T_N, however, in the present case, this component is assigned to an inpurity of the sample, which is apparent in the XRD data. The much smaller value of H_{hf} in Mn_3Sn than in Mn_2RhSn is due to the antiferromagnetic compensation of magnetic moments of twelve Mn-atoms comprising the first coordination sphere of Sn-atoms. In the vicinity of the magnetic transition magnetic fluctuations are strongly developed. With increase of the Rh-concentration the magnetic ordering temperature shifts towards room temperature, this is why Mössbauer measurements at room temperature reveal strong magnetic fluctuations in $Mn_{2.2}Rh_{0.8}Sn$-$Mn_{2.5}Rh_{0.5}Sn$, which give rise to the broad H_{hf} distributions. Mn_3Sn contains no Rh-atoms and is weak ferromagnetic [98] at room tempera-

ture. Apparently, evolution of the Mössbauer spectra with decreasing Rh-concentration in $Mn_{3-x}Rh_xSn$ allows to visualize a transition between the weak magnetic Mn_3Sn phase and the Mn_2RhSn phase revealing larger magnetic moments. Antiferromagnetic compensation of Mn magnetic moments is disturbed by nonmagnetic Rh-atoms. Therefore, it leads to a higher value of the hyperfine magnetic field on Sn-atoms, in comparison with Mn_3Sn. One should notice, that there is no structural transition found at low temperatures for Mn_2RhSn [96]. Since the spectra at room temperature frequently have shown a dynamic part, the measurements at 80 K are helpful to clarify the reason of spectral broadening. With decreasing the Rh-concentration from Mn_2RhSn to $Mn_{2.5}Rh_{0.5}Sn$ the inverse tetragonal structure vanishes and for $0.6 \leq x \leq 0.8$ a coexistence of tetragonal and hexagonal phase was found in XRD. The phase coexistence is the origin for the spectral shapes in this region. Therefore, the Mössbauer data drastically differ from each other. One can explain their difference by Rh destroying the magnetic exchange pathways between the antiferromagnetic Mn atoms. The fitting results from the Mössbauer measurements at 300 K are given in Table 8.4. As it follows from the comparison of Figure 8.4 and Figure 8.6, the main difference from the Mössbauer spectra of Mn_2RhSn and $Mn_{2.1}Rh_{0.9}Sn$ is the broad component at room temperature emerging in the case of the latter one. At 80 K these two compounds have similar spectra. Based on this fact and taking into account temperatures of magnetic ordering (Table 8.2), we conclude that the broad part is not due to the magnetic fluctuations and should be attributed to an anti site disordering effect. $Mn_{2.2}Rh_{0.8}Sn$ consists of two phases (tetragonal and hexagonal), which appears clearly in the corresponding XRD pattern. The Mössbauer spectrum of this compound recorded at room temperature consists of very broad components and demonstrates no quadrupole splitting like the other members of this series. The broad component with a relative intensity of 74% (CS=-0.72(3) mm/s, H=112(1) kOe) should be assigned to a larger anti site disorder effect. The spectrum of this compound at 80 K is difficult to analyse. Finally, we assume that at room temperature an overlapping between the magnetic fluctuations (due to the coexistence of two different crystal structure phases) and a huge anti site disorder occurs. According to the magnetic data the T_C lies slightly above room temperature, therefore, one could expect a magnetic splitting even at room temperature, but we assume that the high degree of antisite disorder and the magnetic fluctuations interfere (there could be a distribution of $T_C^{'}$s due to the disorder), that makes the analysis of this spectrum difficult. $Mn_{2.3}Rh_{0.7}Sn$ can be also explained with the same scenario like $Mn_{2.2}Rh_{0.8}Sn$, but one should notice, the latter shows a higher degree of anti site disordering. The Mössbauer spectrum of $Mn_{2.4}Rh_{0.6}Sn$ also consists of two components. According to the XRD data this sample consists of tetragonal and hexagonal phases in approximately equal amounts. According to this finding, a broad subspectrum with CS=-0.83(2) mm/s and H_{hf}=108(1) kOe could be assigned to the tetragonal phase, whereas the part with a sharper signal order (CS=-0.83(2) mm/s; H_{hf}=28(1) kOe) could be attributed to the hexagonal phase.

Table 8.4: Mössbauer data revealed at 80 K of $Mn_{3-x}Rh_xSn$. p gives the weight of the component (sum of p's is 1) [33].∗) marks a fixed component.

$Mn_{3-x}Rh_xGa$	p [%]	H_{hf} [kOe]	A [%]	CS [mm/s]	QS [mm/s]
Mn_3Sn		46 (1)	84	-0,76 (1)	0
		194 (2)	16	-0,22 (1)	0.14(2)
$Mn_{2.9}Rh_{0.1}Sn$	61	51 (1)		-0,76 (2)	0
	39	81 (1)		-0,76 (2)	0
$Mn_{2.8}Rh_{0.2}Sn$	84	50 (1)		-0,81 (2)	0
	16	119 (4)		-0,81 (2)	0
$Mn_{2.7}Rh_{0.3}Sn$	39	55 (1)		-0,61 (2)	0
	61	13 (1)		-0,61 (2)	0
$Mn_{2.6}Rh_{0.4}Sn$	93	46 (1)		-1,01 (1)	0
	7	126 (4)		-1,01 (1)	0
$Mn_{2.5}Rh_{0.5}Sn$	75	45 (1)		-0,95 (7)	0
	25	71 (1)		-0,95 (7)	0
$Mn_{2.4}Rh_{0.6}Sn$	23	46 (1)		-0,86 (3)	0
	77	145 (1)		-0,86 (3)	0
$Mn_{2.3}Rh_{0.7}Sn$	20	48 (1)		-0,82 (3)	0
	80	122 (4)		-0,82 (3)	0
$Mn_{2.2}Rh_{0.8}Sn$	74	112 (1)		-0,72 (3)	0.19(2)
	26	195 (2)		-0,72 (3)	
$Mn_{2.1}Rh_{0.9}Sn$	78	150 (2)	98	-0,88 (1)	0.07(2)
	22	114 (1)		-0,88 (1)	
	22	300 (∗)	2	-0,88 (1)	0.15(6)
Mn_2RhSn		212 (1)	7	-0,86 (2)	0
	47	112 (1)	93	-0,86 (2)	0.07(1)
	53	124 (4)		-0,86 (2)	

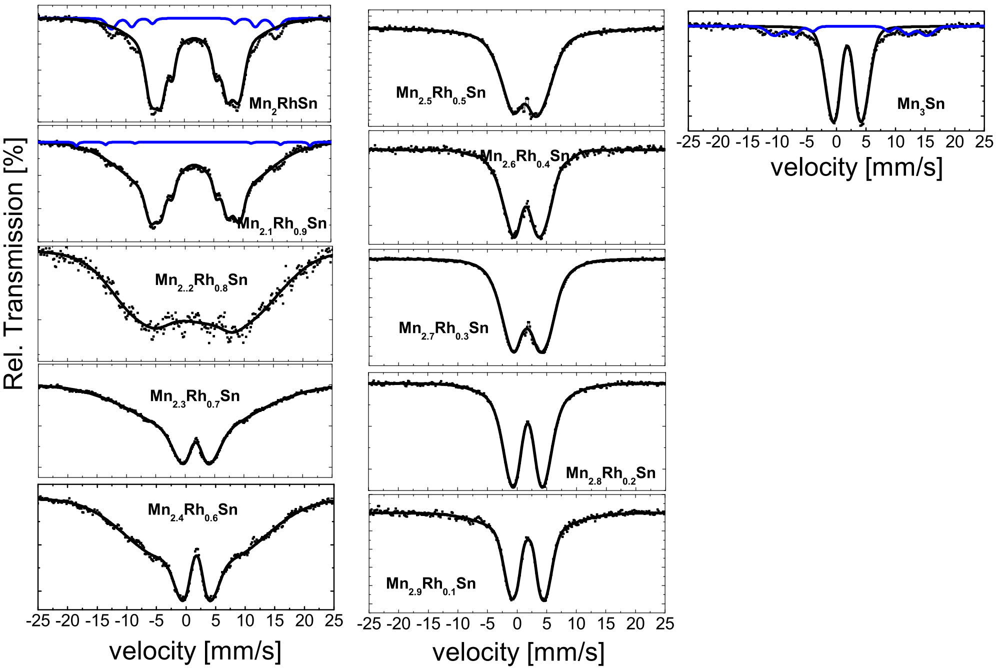

Figure 8.6: Mössbauer spectra of $Mn_{3-x}Rh_xSn$ performed at 80 K in transmission mode.

8.3 Conclusion

The series $Mn_{3-x}Rh_xSn$ with the concentration range x=0-1 has been synthesized and experimentally investigated. To clarify their structure XRD measurements were done, which proved the presence of the inverse tetragonal structure ($I\bar{4}m2$) in four samples (Mn_2RhSn, $Mn_{2.1}Rh_{0.9}Sn$, $Mn_{2.3}Rh_{0.7}Sn$ and $Mn_{2.4}Rh_{0.6}Sn$) from this series. However, the corresponding ratio c/a of the lattice parameters is found to be too low (c/a=1.54) for applications with the MgO-system. These compounds exhibit low magnetic moments, which is one of the conditions that materials should fulfill to be potential compounds for STT. Further support for the magnetic properties of these compounds were obtained using ^{119}Sn-Mössbauer spectroscopy. The amount of site/antisite disorder effects and the emergence of magnetic fluctuations phenomena have been considered and clarified from the Mössbauer data. The Mössbauer effect on these compounds found high values of the average magnetic hyperfine fields induced on Sn-atoms at 80 K from 40 kOe (Mn_3Sn) to 120 kOe ($Mn_{2.2}Rh_{0.8}Sn$). As it follows, only the end members Mn_3Sn (hexagonal)

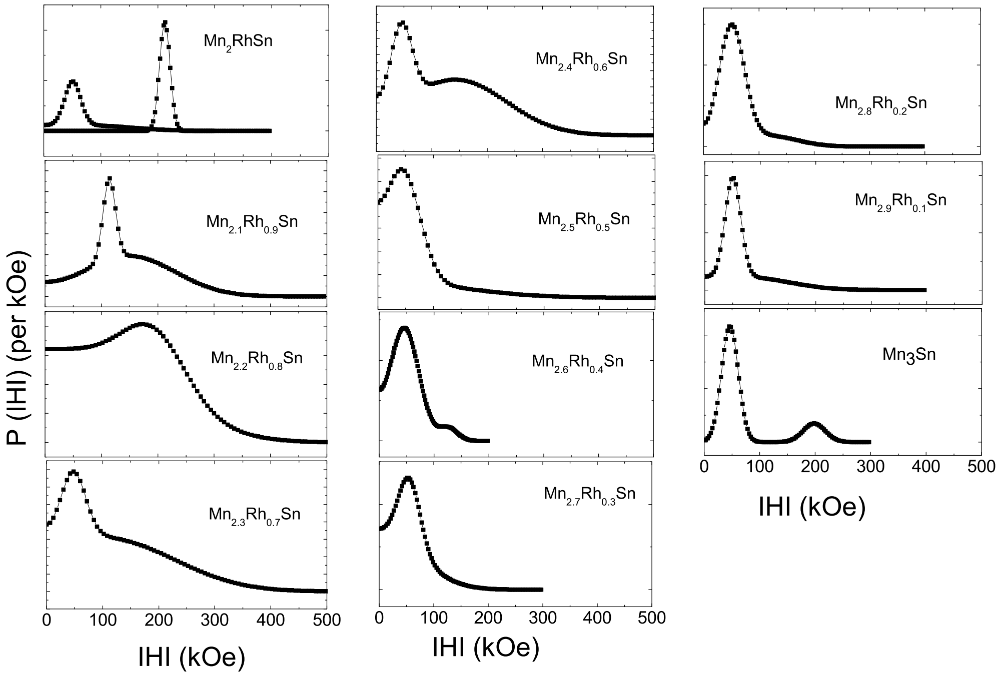

Figure 8.7: $|H_{hf}|$ distributions obtained from the Mössbauer spectra performed at 80 K.

and Mn_2RhSn (tetragonal) are quite well defined materials. All the other materials are mixed phases and strongly disordered, where with increasing the Rh amount the tetragonal phase becomes dominant. In particular, the XRD lattice parameters do not change systematically with x for a given phase, i.e tetragonal or hexagonal. It seems that only Mn_2RhSn may be interesting for potential applications. The interpretation of the properties of the other materials remains difficult due to the occurrence of a phase mixture.

9 Structural and magnetic properties of $Mn_{3-x}Fe_xGa$

9.0.1 Introduction

Besides the great number of Heusler materials typically crystallizing in the centrosymmetric form (space group No. 225 for cubic or 139 for tetragonal), Mn-rich compounds were recognized as a special type of alloys exhibiting outstanding magnetic properties following from the lack of the inversion symmetry (space grup 216 for cubic, or 119 for tetragonal) and the presence of localized magnetic moments. Often it is also combined with tetragonal strain. In these materials, Mn spins typically occupies two different Wyckoff positions. In cubic symmetry (group No. 216) these are $4a$ (or $4b$) and $4c$ (or $4d$), in tetragonal (group No. 119) - $2a$ (or $2b$) and $2c$ (or $2d$). In both cubic and tetragonal cases Mn atoms tend to couple with antiparallel electron spins. For this reason the total magnetic moment in these materials is typically small, which makes them attractive for spin-torque transfer applications (if magnetic anisotropy is present). The prototype tetragonal Mn_3Ga (Mn_2MnGa) material with a small magnetic moment of $1\ \mu_B$, but high Curie temperature and strong magnetic anisotropy, was basis for the various $Mn_{3-x}Y_xGa$ series (with Y=Co, Ni, Rh, etc.) [77, 42, 96] in attempts to implement the attractive properties of Mn_3Ga within often used configurations of nowadays spintronics devices. In this chapter we discuss the studies performed on the series obtained by Fe substitution, namely the magnetic and structural properties of $Mn_{3-x}Fe_xGa$ for $1 \leq x \leq 3$. It was assumed that Mn_2FeGa, Fe_2MnGa and Fe_3Ga are attractive for their shape-memory properties. In particular, Fe-rich alloys, i. e. Fe_3Ga (Fe_2FeGa) single crystals with DO_3 structure demonstrate giant pseudoelasticity at room temperature, which is one of the primary conditions to exhibit the shape memory effect. The pseudoelasticity is a reversible response to an applied stress as a consequence of a phase transformation between the austenitic and martensitic phases [99]. In contrast, here we studied the series of the polycrystalline samples.

9.0.2 Synthesis of the materials

$Mn_{3-x}Fe_xGa$ samples were synthesized by repeated arc-melting of stoichiometric amounts of the elements in an argon atmosphere. To avoid oxygen contamination Ti was used as a getter material. The weight loss was less than 0.5%. As-cast samples were annealed at 400 °C and at 1100 °C for one week to improve the crystal quality and phase purity. In addition samples of Fe_2MnGa and Mn_2FeGa were annealed at 600° C. Additionally they were quenched in ice/water mixture. Magnetic properties of the disc sample have been determined using a SQUID (superconducting quantum interference device) within the temperature range 5-400 K. Mössbauer measurements at room temperature were carried out using a ^{57}Co source in the backscattering mode.

9.0.3 Structural characterization

The structural information was obtained from XRD measurements carried out at room temperature. The lattice parameters were determined by Rietveld refinement using the FullProf package. Figure 9.1 illustrates four typical diffraction patterns for Fe_2MnGa (approx. 75% of the tetragonal and 25% of the hexagonal phase), $Fe_{1.95}Mn_{1.05}Ga$ (almost the hexagonal phase), $Fe_{1.5}Mn_{1.5}Ga$ (almost equal amounts of the tetragonal and hexagonal phases) and Mn_2FeGa (only tetragonal).The as-cast samples and the samples annealed at temperatures lower than 350° C exhibit a pseudocubic phase (not shown in this work). Samples annealed at 400° C revealed a mixture of two phases pseudocubic (I4/mmm) and hexagonal ($P6_3$/mmc) except for Mn_2FeGa (see Fig. 9.1). The latter exhibits the tetragonal phase (space group $I\bar{4}m2$). The lattice parameters for this series are listed in the Tables 9.1 and 9.2. As it follows overall in these compounds both tetragonal and hexagonal phases posses very close energies, which often leads to the decomposition (phase separation) more or less evidently seen in XRD. For instance, even a slight change in composition or annealing temperature can lead to a drastic change of the structural properties. For instance, 5% increase of Mn content (from Fe_2MnGa to $Fe_{1.95}Mn_{1.05}Ga$) leads to a decomposition into 90% of β-Fe_3Ga (hexagonal, $P6_3/mmc$) plus about 10% of pseudocubic Fe_2MnGa. Recent studies of the ternary phase diagram of Gd-Fe-Ga demonstrate that the intermediate cubic α-Fe_3Ga phase ($Pm\overline{3}m$) emerges for the annealing temperature $T > 600°$ C, whereas hexagonal β-Fe_3Ga ($P6_3/mmc$) - for $T < 600°$ C [100]. The latter is also confirmed by our observations. Fe_3Ga annealed at 1100 ° C exhibits the cubic α-Fe_3Ga ($Pm\overline{3}m$) structure. Overall, according to the XRD data, the amount of hexagonal phase increases with amount of Fe. Indeed, for Fe-poor $Mn_{1.95}Fe_{1.05}Ga$ the hexagonal phase can be hardly resolved from the corresponding XRD patterns (for the case of Mn_2FeGa it totally vanishes). The distinction between the tetragonal and hexagonal phases is mostly evident in Fig. 9.1, where the hexagonal component is marked by red and the tetragonal - by blue. It is important to notice, that $Mn_{1.4}Fe_{1.6}Ga$ also contains about 7-8 % of elementary Fe phase (space group No. 229). In contrast to the samples annealed at 400° C, the samples annealed at higher temperatures (800° C and 1100° C) tend to exhibit a pseudocubic structure. Within a range from $Fe_{2.2}Mn_{0.8}Ga$ to Fe_3Ga the samples were annealed only at 1100° C to ensure the highest diffusion rate [101], and therefore the observed structure is attributed to the cubic one (Fm-$3m$, space group No. 225, BiF_3-type) (see Fig. 9.2). The BiF_3 type of the Heusler structure is not easy to distinguish from the well ordered Heusler structure $L2_1$ only from the XRD measurements, because of their similar XRD patterns. However, the Pearson Database and Mössbauer results (which confirm a large antisite disorder), exclude the latter one [102].

It is known that the ordered Heusler alloys are characterized by the presence of (111) and (200) superlattice reflections, which correspond to the ordered (B, D) and (A, C) sublattices, respectively [100]. As it follows from Figure 9.3,

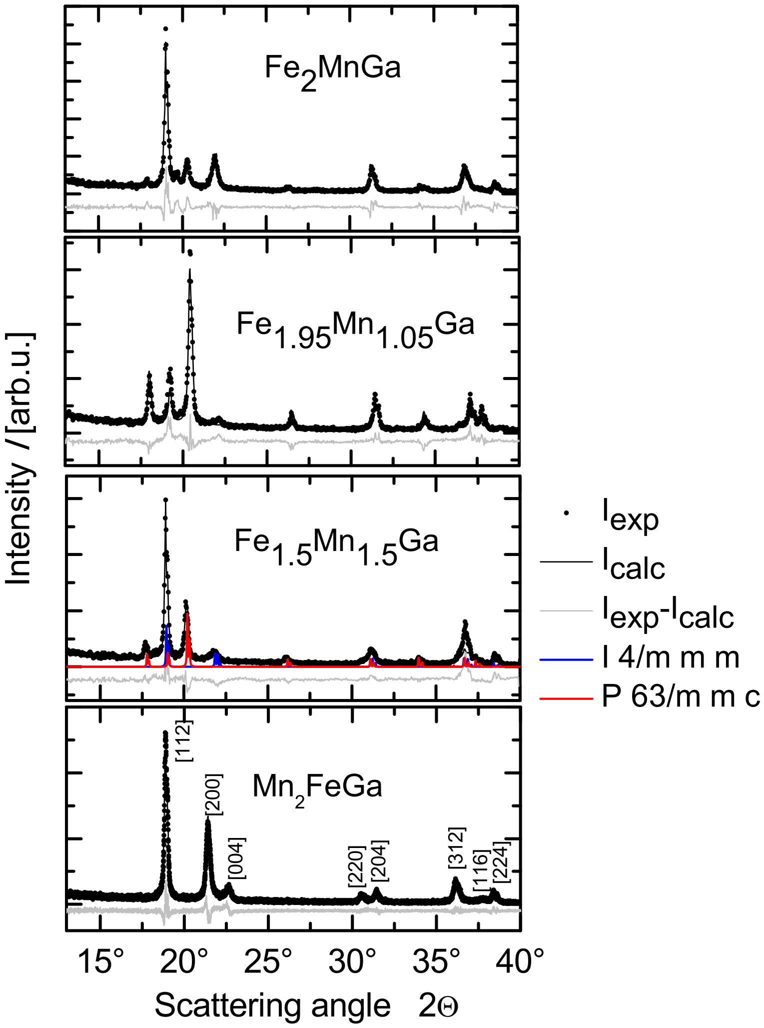

Figure 9.1: XRD patterns of $Mn_{3-x}Fe_xGa$ alloys annealed at 400° C. The diffraction patterns (black dots) of Fe_2MnGa, $Fe_{1.95}Mn_{1.05}Ga$, $Fe_{1.5}Mn_{1.5}Ga$ and Mn_2FeGa are compared to the curve fits (black solid line) from the Rietveld refinements; the difference between them is shown in gray. Red and blue colors correspond to hexagonal ($P6_3/mmc$) and tetragonal ($I4/mmm$) model fits. In contrast, Mn_2FeGa occurs in the inverse tetragonal structure ($I\bar{4}m2$). The measurements were carried out at room temperature using Mo $K_{\alpha1,\alpha2}$ radiation.

Table 9.1: XRD data of the $Mn_{3-x}Fe_xGa$ alloys annealed at 400° C. Rietveld refinements were done only for certain samples, whereas for most of the samples a phase analysis using the software program package pcw was done. $*$ marks the space group I$\bar{4}$m2 corresponding to an inverse tetragonal structure.

Composition	a [Å]	c [Å]	c/a	a [Å]	c [Å]	c/a
		($I4/mmm$)			($P6_3/mmc$)	
Mn_2FeGa $*$	3.7915(1)	7.1850(2)	1.89	-	-	-
$Mn_{1.95}Fe_{1.05}Ga$	3.6857	7.4421	2.02	5.2499	4.2607	0.81
$Mn_{1.8}Fe_{1.2}Ga$	3.7202	7.2868	1.96	5.4001	4.3512	0.81
$Mn_{1.6}Fe_{1.4}Ga$	3.7272	7.5743	2.03	5.3076	4.2946	0.81
$Mn_{1.5}Fe_{1.5}Ga$	3.7003	7.5806	2.05	5.3115	4.2824	0.81
$Mn_{1.4}Fe_{1.6}Ga$	-	-	-	5.2655	4.2715	0.81
$Mn_{1.3}Fe_{1.7}Ga$	3.6994	7.4683	2.02	5.2597	4.2687	0.81
$Mn_{1.2}Fe_{1.8}Ga$	3.7341	7.5834	2.02	5.2820	4.2952	0.81
$Mn_{1.05}Fe_{1.95}Ga$	3.7102	7.5978	2.05	5.2867	4.2934	0.81
Fe_2MnGa	3.7225(2)	7.4708(3)	2.01	5.2847(8)	4.3015(3)	0.81

Table 9.2: XRD data of the $Mn_{3-x}Fe_xGa$ alloys annealed at 1100° C. For Mn_2FeGa, $Mn_{1.95}Fe_{1.05}Ga$ and $Mn_{1.8}Fe_{1.2}Ga$ are displayed the XRD data from the annealing temperature 800° C.

Composition	a [Å]	c [Å]	c/a	a [Å]
		($I4/mmm$)		($Fm-3m$)
Mn_2FeGa	3.7150(6)	7.5108(1)	2.02	-
$Mn_{1.95}Fe_{1.05}Ga$	3.7512	7.5679	2.02	-
$Mn_{1.8}Fe_{1.2}Ga$	3.7286	7.5476	1.96	-
$Mn_{1.6}Fe_{1.4}Ga$	3.7409	7.4371	1.99	-
$Mn_{1.5}Fe_{1.5}Ga$	3.6959(5)	7.4275(6)	2.01	-
$Mn_{1.4}Fe_{1.6}Ga$	3.7279	7.4025	1.99	-
$Mn_{1.3}Fe_{1.7}Ga$	3.7103	7.4748	2.03	-
$Mn_{1.2}Fe_{1.8}Ga$	3.7350	7.3789	1.98	-
$Mn_{1.05}Fe_{1.95}Ga$	3.7101	7.4760	2.02	-
Fe_2MnGa	3.6993(2)	7.4609(1)	2.02	-
$Mn_{0.8}Fe_{2.2}Ga$	3.6847(8)	7.6089(8)	2.06	5.8824(9)
$Mn_{0.6}Fe_{2.4}Ga$	-	-	-	5.9207(9)
$Mn_{0.4}Fe_{2.6}Ga$	-	-	-	5.8882(9)
$Mn_{0.2}Fe_{2.8}Ga$	-	-	-	5.8530(8)
Fe_3Ga	-	-	-	5.8657(4)

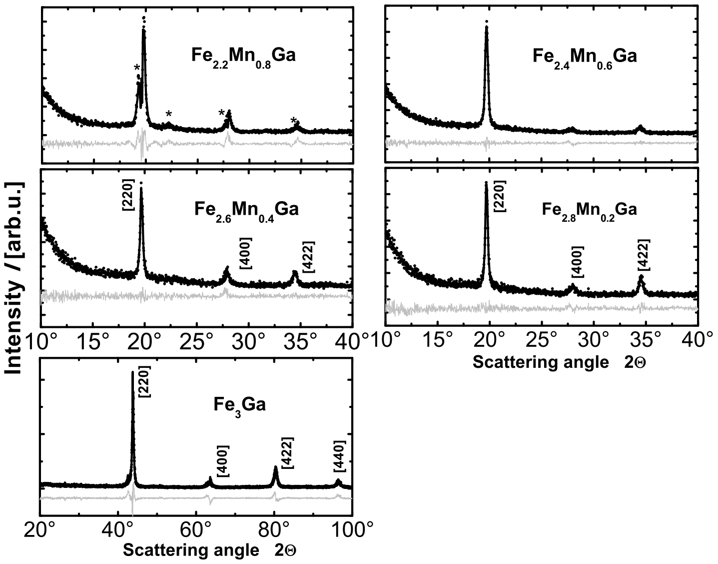

Figure 9.2: XRD patterns of $Fe_{2.2}Mn_{0.8}Ga$-Fe_3Ga annealed at 1100° C for one week. The diffraction patterns are compared to the curve fits from the Rietveld refinements. The measurements were carried out at room temperature using Cu K_α and Mo $K_{\alpha1,\alpha2}$ radiation. ∗) marks the tetragonal structure (I4/mmm).

Table 9.3: XRD data of Fe_2MnGa and Mn_2FeGa alloys annealed at 600° C.

Composition	a [Å]	c [Å]	c/a	a [Å]	c [Å]	c/a
		($I4/mmm$)			($P6_3/mmc$)	
Mn_2FeGa	3.7830	7.5063	1.98	2.6770	4.3800	1.64
Fe_2MnGa	3.7030	7.5020	2.03	5.2684	4.2673	0.81

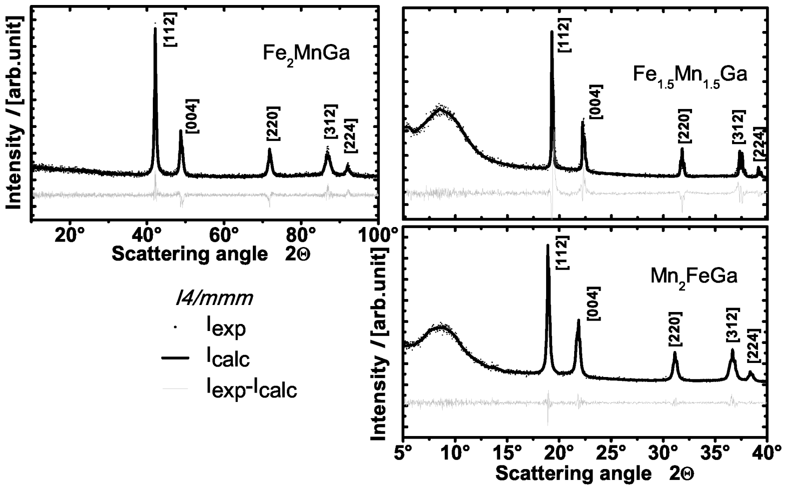

Figure 9.3: XRD patterns of Fe_2MnGa, $Fe_{1.5}Mn_{1.5}Ga$ and Mn_2FeGa annealed at 1100° C or 800° C, respectively, for one week. The diffraction patterns are compared to the curve fits from the Rietveld refinements. The measurements were carried out at room temperature using Cu K_α (left) and Mo $K_{\alpha 1,\alpha 2}$ (right) radiation.

these superstructure peaks are missing. Thus, the presence of the anti-site disorder using Mössbauer results will be confirmed.

Further investigated were Fe_2MnGa and Mn_2FeGa annealed at 600° C, respectively. The XRD patterns of these two samples are shown in Figure 9.4. Both samples consist of two phases. The major part represents the hexagonal structure ($P6_3/mmc$), whereas the minor part the pseudocubic one (I4/mmm). In contrast to Fe_2MnGa, Mn_2FeGa shows the hexagonal structure (Mg-type), where a high anti site disorder is expected. The lattice parameters used for the Rietveld refinement are given in Table 9.3.

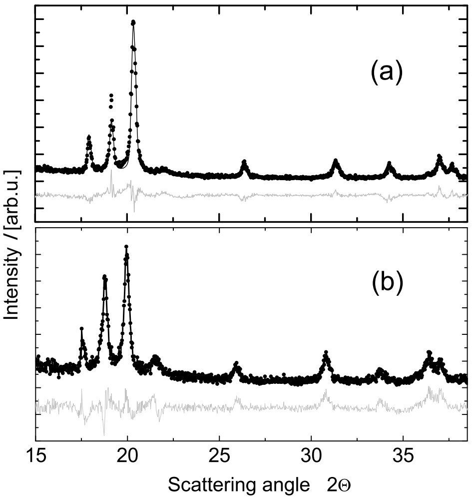

Figure 9.4: XRD patterns of Fe_2MnGa (a) and Mn_2FeGa (b) alloys annealed at 600° C. The diffraction patterns (black dots) are compared to the curve fits (black solid line) from the Rietveld refinements; the difference between them is shown in gray. The measurements were carried out at room temperature using Mo $K_{\alpha1,\alpha2}$ radiation.

9.1 Magnetic characterization

9.1.1 SQUID measurements

Magnetic measurements were performed by means of SQUID within the range of 5 − 800 K. As it follows from Figures 9.5 and 9.6,

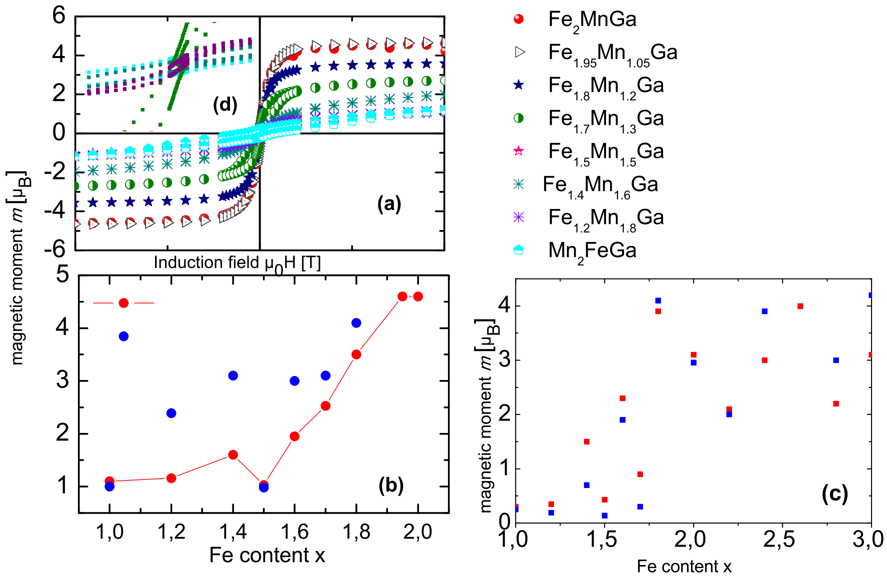

Figure 9.5: Hysteresis at 300 K (a) of $Mn_{3-x}Fe_xGa$ annealed at 400° C for two weeks. Figure (b) and (c) display the summary of the magnetic moments measured at 300 K (red) and 5 K (blue) of $Mn_{3-x}Fe_xGa$ annealed at 400° C or 1100° C, respectively, d) zoom of Mn_2FeGa, $Mn_{1.8}Fe_{1.2}Ga$, $Mn_{1.6}Fe_{1.4}Ga$ and $Mn_{1.5}Fe_{1.5}Ga$ hysteresis.

the samples from Mn_2FeGa to $Mn_{1.5}Fe_{1.5}Ga$ are hard ferrimagnets (with small total magnetic moments), whereas from $Fe_{1.6}Mn_{1.4}Ga$ to Fe_3Ga - soft ferromagnetic materials are found(excluding $Mn_{1.3}Fe_{1.7}Ga$, which is also a hard ferrimagnet). For $Fe_{1.7}Mn_{1.3}Ga$, $Fe_{1.2}Mn_{1.8}Ga$ and $Mn_{1.5}Fe_{1.5}Ga$ the coercive fields H_C were found to be 0.1 T, 0.045 T and 0.2T, respectively, whereas the remanent magnetizations are 0.5 μ_B/f.u, 0.1 μ_B/f.u and 0.1 μ_B/f.u. Remarkably high values of the magnetic moments at 5 K are exhibited by Fe_2MnGa (4 μ_B) and $Fe_{2.6}Mn_{0.4}Ga$ (4.8 μ_B). For the cubic Fe_3Ga the measured magnetic moment 3 μ_B agrees well with the Slater-Pauling rule, whereas the other compounds do not obey this rule. According to XRD data (Fig. 9.1)

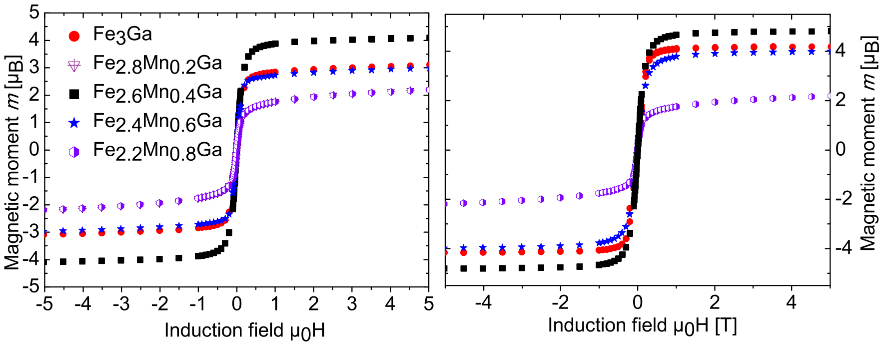

Figure 9.6: Hysteresis at 300 K (a) and hysteresis at 5 K (b) of Fe_3Ga,$Fe_{2.8}Mn_{0.2}Ga$, $Fe_{2.6}Mn_{0.4}Ga$, $Fe_{2.4}Mn_{0.6}Ga$, $Fe_{2.2}Mn_{0.8}Ga$ annealed at 1100° C for one week.

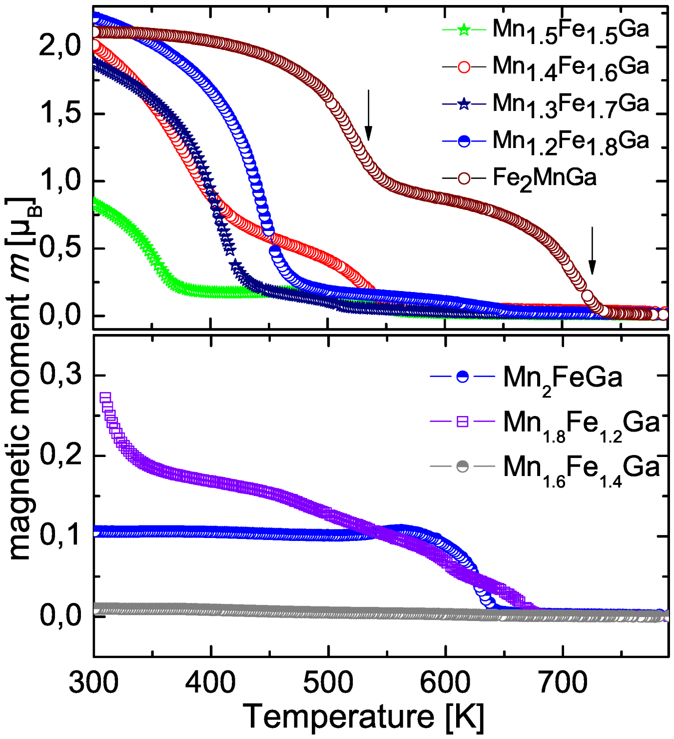

Figure 9.7: Magnetization at 0.1 T as a function of temperature for $Mn_{3-x}Fe_xGa$ annealed at 400° C.

for all compounds annealed at 400° C there were two phases obtained (except Mn_2FeGa). Hence, the high-temperature magnetic measurements show a clear fraction of the two phases (see Fig. 9.7). Almost all the curves exhibit two drops of magnetization. As it follows from the structural and magnetic data, the explanation of properties in these materials has to consider that they are mostly phase mixtures. The observed behavior indicates the energetic proximity of the tetragonal and hexagonal phases, which may suggest these materials as possible shape-memory candidates.
Also for Fe_2MnGa and Mn_2FeGa annealed at 600° C, respectively, were done magnetic measurements. Note that these materials are not single phase, in contrast to samples annealed under different conditions.

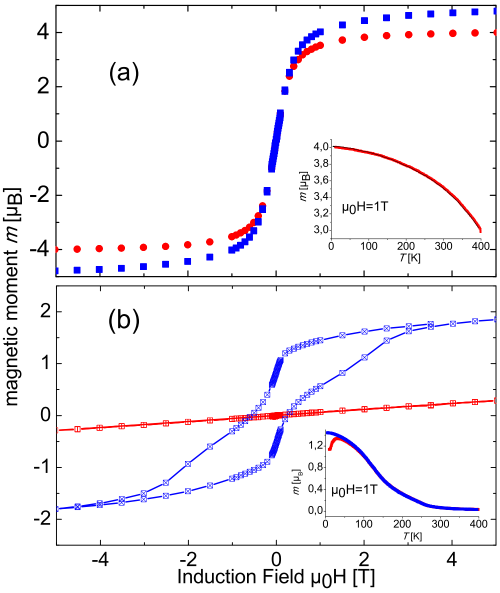

Figure 9.8: Hysteresis at 300 K (red) and hysteresis at 5 K (blue) of Fe_2MnGa (a) and Mn_2FeGa (b) annealed at 600° C for one week. The insets show M (T)-curves applying a magnetic field of 1 T.

As in Figure 9.8 is shown, Fe_2MnGa reveals at 300 K a magnetic moment of 4.0 μ_B, whereas the magnetic moment at 5 K amounts to 4.8 μ_B. In this case the interpretation of the magnetic data is difficult, since the sample contains also an elementary Fe fraction. In contrast, Mn_2FeGa is magnetic just at 5 K. As it follows, Mn_2FeGa becomes hard magnetic and Fe_2MnGa remains soft magnetic at room temperature as well as at low temperatures, respectively. For Mn_2FeGa the coercive field H_C was found to be 0.42 T whereas the remanent magnetization is $0.95\,\mu_B/f.u.$

9.1.2 Mössbauer spectroscopy

Here we discuss the results of Mössbauer spectroscopy on Fe atoms, needed to obtain the information about their local magnetic environment. The measurements were done at room temperature in backscattering geometry using disc-shaped samples rather than powder due to their high ductility. As it follows from Figure 9.9,

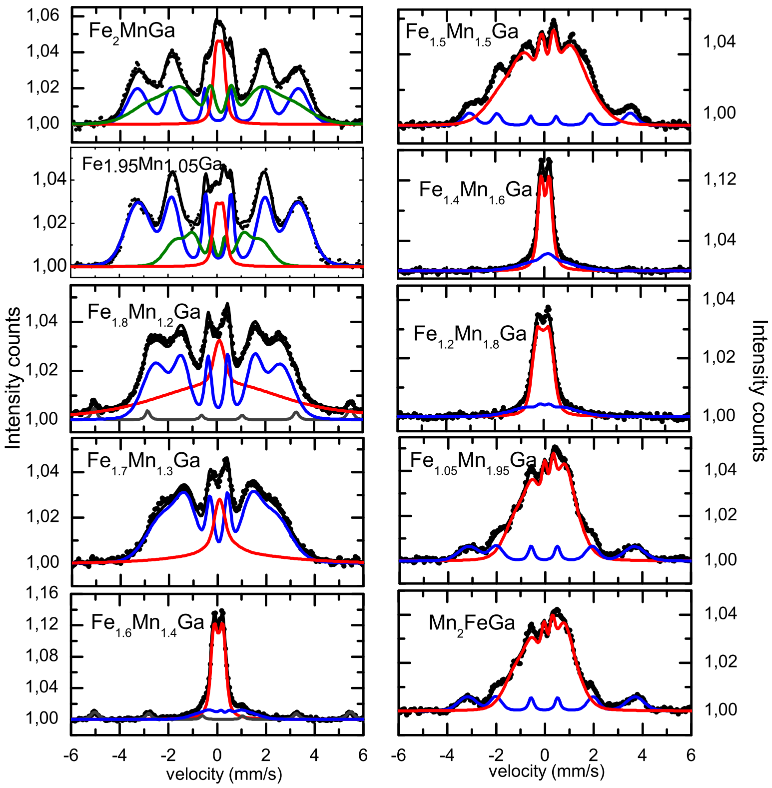

Figure 9.9: Mössbauer spectra of $Mn_{3-x}Fe_xGa$ annealed at 400° C for two weeks, measured at room temperature.

the measured Mössbauer spectra consist of several sextets. Since the spectra cannot be fitted by Lorentzians due to their broad shape, we have used the Voigt-based fitting (VBF) method. In disordered compounds with a general random distribution, like

Table 9.4: Mössbauer parameters of $Mn_{3-x}Fe_xGa$ annealed at 400° C. CS is the center shift, H_{hf} the hyperfine magnetic field, A the intensity area.

x	CS_1 [mm/s]	H_{hf1} [kOe]	A_1 [%]	CS_2 [mm/s]	H_{hf2} [kOe]	A_2 [%]	CS_3 [mm/s]	H_{hf3} [kOe]	A_3 [%]
2	0.036(2)	207(2)	37	0.100(2)	12(1)	13	0.160(3)	166(7)	50
1.95	0.057(2)	204(1)	68	0.053(2)	107.42	23	0.107(2)	12(1)	9
1.8	-0.010(3)	162(2)	45	-0.020(2)	158(3)	41	-0.022(4)	30(4)	15
1.7	0.066(3)	140(2)	77	0.106(3)	19(4)	23			
1.6	0.051(2)	15(1)	66	0.220(2)	325(2)	12	0.327(4)	64(4)	22
1.5	0.107(3)	205(3)	10	0.068(2)	91(2)	81	0.061(7)	185(8)	10
1.4	0.051(3)	15(1)	66	0.220(2)	325(1)	10	0.327(4)	64(4)	22
1.2	-0.011(2)	21(1)	74	0.047(9)	70(1)	26			
1.05	0.056(2)	64(1)	80	0.111(3)	212(3)	20			
1.0	0.116(3)	213(2)	20	0.044(1)	64(1)	80			

$(X_{1-x}X'_x)_2YZ$, $X_2Y_{1-x}Y'_xZ$ or $X_2YZ_{1-x}Z'_x$, one expects simultaneously the occurrence of different surroundings of the probed atoms. In turn to each particular environment of Fe-atoms a hyperfine field corresponds. Here we have used a powder model with intensity ratios 3:2:1:1:2:3. In case of the hexagonal structure we expect a disordering at least between Fe and Mn, since Fe and Mn sit at the 3c Wyckof positions. Hence, Fe and Mn positions are not distinguishable. As it follows from Figure 9.9, all the spectra consist of one non-magnetic and at least two different magnetic contributions. Despite the slight change in composition, for instance, from Fe_2MnGa to $Fe_{1.95}Mn_{1.05}Ga$, noticeable changes in the structural phase composition were determined but the Mössbauer data alter only slightly for $1.7 \leq x \leq 2$. The larger amount of anti-site disorder is observed for Fe_2MnGa. A comparison of the Mössbauer spectra for Mn_2FeGa and $Mn_{1.95}Fe_{1.05}Ga$ reveals similar features as well, even though they exhibit different crystal structures. Both spectra consist of one sextet with higher H_{hf} with relative intensity of 20 % and another sextet corresponding to a smaller value of H_{hf} with relative intensity of 80 %. Thus, using Mössbauer spectroscopy enables the observation of two distinct environments of Fe atoms, which were not resolved by XRD. One should mention that in the present case the large distribution of the hyperfine magnetic fields observed from the fitting results of the Mössbauer spectra reflects a distribution of Fe-positions. In the $Mn_{1.2}Fe_{1.8}Ga$ and $Mn_{1.4}Fe_{1.6}Ga$ spectra, one of the sextets can be assigned to metallic Fe with relative intensity less than 10 %. Due to the broad distribution of the internal magnetic fields it is complicated to identify from which crystallographic phase (tetragonal or hexagonal) the various sextets originate. According to the magnetic data, both $Mn_{1.8}Fe_{1.2}Ga$ and $Mn_{1.4}Fe_{1.6}Ga$ exhibit a low magnetic moment, which agrees well with Mössbauer results, since the hyperfine field H_{hf} on Fe is proportional to its magnetic moment [103]. Mössbauer spectra of $Mn_{1.8}Fe_{1.2}Ga$ can be decomposed into one nearly nonmagnetic sextet, with relative intensity of 74 % and a magnetic field of 21(1) kOe and a sextet which corresponds to the remaining 26 % with H_{hf} of 70(1) kOe. Just as well represents $Mn_{1.4}Fe_{1.6}Ga$ the same behavior. The nearly nonmagnetic component appears as a major part with intensity fraction of 66%, and small H_{hf} (15(1) kOe), whereas the remaining intensity is 22% and corresponds to the highest magnetic splitting H_{hf} =64(4) kOe. It is already known that the hyperfine field on Fe is very sensitive and by slight changes of the nearest neighbors it could be influenced. Information from the quadrupole splitting in such high by disordered materials is not so effectual, because of the two coexisting phases (the tetragonal and the hexagonal one). In the present case, the average effective hyperfine field increases with increasing iron concentration. The results from the fitting are given in Table 9.4. Furthermore, Mössbauer spectra of Mn_2FeGa and Fe_2MnGa annealed at 600 ° C are given in Figure 9.10.

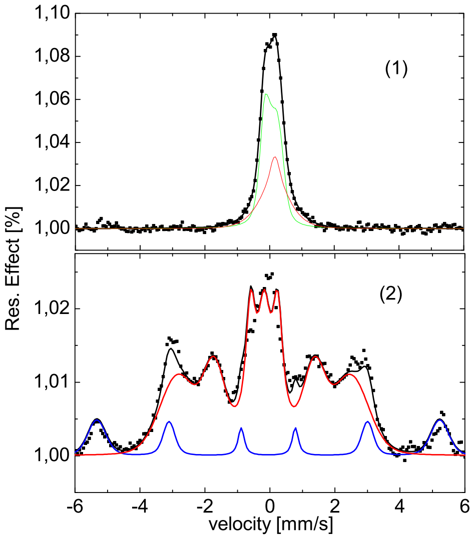

Figure 9.10: Mössbauer spectra of Mn_2FeGa (1) and Fe_2MnGa (2) annealed at 600 ° C , respectively, measured at room temperature.

As it follows, the Mössbauer spectrum of Mn_2FeGa consists of two broad nearly nonmagnetic components, which confirm disordering of the elements of this compounds as expected from XRD data. In contrast, the Mössbauer spectrum of Fe_2MnGa shows a majority part with a broad magnetic component and a minority part with a nearly nonmagnetic component. Unfortunately, in this compound was found elementary Fe. The Mössbauer data confirm this fact (see, blue curve, Figure 9.10, b).The results from the fitting are given in Table 9.5.

Additionally, Mössbauer spectra from Mn_2FeGa to Fe_3Ga annealed at 1100° C are given in Figure 9.11.

Table 9.5: Mössbauer parameters of Fe_2MnGa and Mn_2FeGa annealed at 600° C. CS is the center shift, H_{hf} the hyperfine magnetic field, A the intensity area.$*$ marks the presence of α iron.

sample	CS_1	H_{hf1}	A_1	CS_2	H_{hf2}	A_2
	[mm/s]	[kOe]	[%]			
Fe_2MnGa	-0.051(2)	327(2)$*$	16	0.176(8)	165(2)	84
Mn_2FeGa	0.050(3)	17(1)	62	0.149(5)	28(2)	38

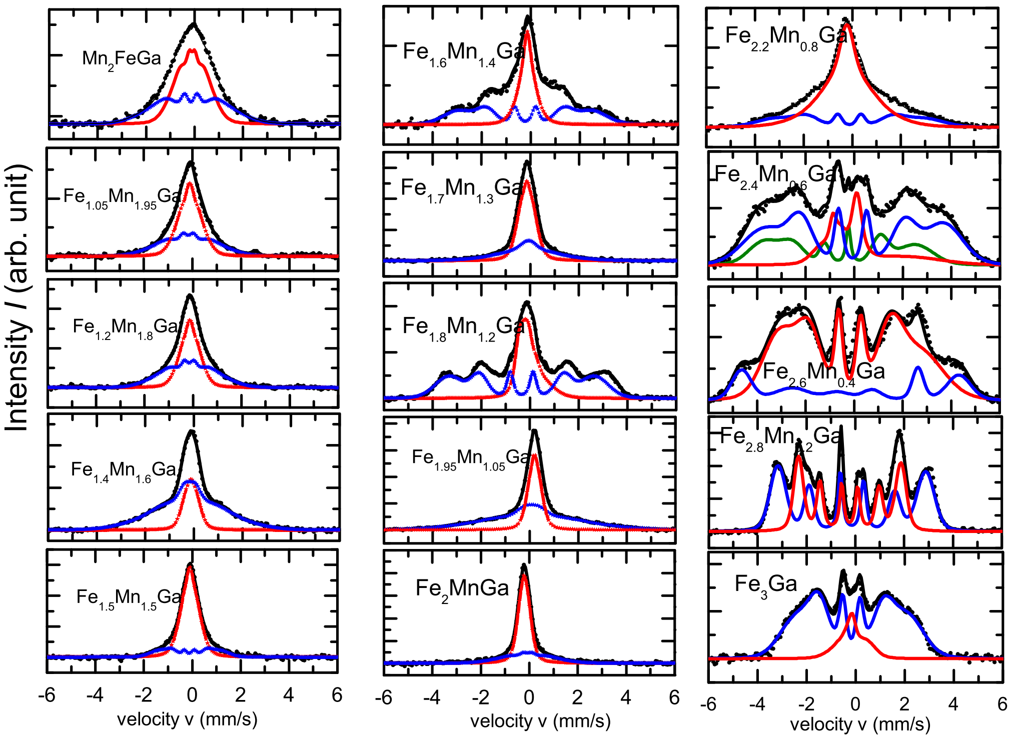

Figure 9.11: Mössbauer spectra of $Mn_{3-x}Fe_xGa$ annealed at 1100° C for one week, measured at room temperature.

Table 9.6: Mössbauer parameters of Mn$_{3-x}$Fe$_x$Ga annealed at 1100° C. CS is the center shift, H$_{hf}$ the hyperfine magnetic field, A the intensity area.

x	CS_1 [mm/s]	H_{hf1} [kOe]	A_1 [%]	CS_2 [mm/s]	H_{hf2} [kOe]	A_2 [%]	CS_3 [mm/s]	H_{hf3} [kOe]	A_3 [%]
1.0	0.116(3)	213(2)	20	0.044(1)	64(1)	80			
1.05	-0.165(4)	75(3)	44	-0.108(3)	28(2)	56			
1.2	-0.121(2)	23(2)	49	-0.146(3)	71(8)	51			
1.4	-0.117(2)	18(1)	24	-0.161(3)	84(5)	76			
1.5	-0.091(2)	21(1)	77	-0.114(4)	79(6)	23			
1.6	-0.226(3)	168(5)	38	-0.147(1)	13(3)	30	-0.169(3)	83(3)	32
1.7	-0.132(1)	19(1)	62	-0.062(6)	52(5)	38			
1.8	-0.158(2)	27(1)	33	0.503(3)	158(2)	17	-0.340(2)	185(2)	50
1.95	0.086(4)	111(9)	62	0.204(5)	15(4)	38			
2	-0.180(5)	219(4)	38	-0.180(5)	161(1)	62	0.114(2)	30(1)	61
2.2	-0.12(4)	187(2)	28	-0.213(9)	69(2)	72			
2.4	-0.63(2)	193(5)	25	-0.25(2)	60(6)	20	0.08(1)	228(3)	54
2.6	-0.457(4)	177(1)	79	0.204(2)	278(2)	21			
2.8	-0.326(5)	188(1)	57	-0.385(6)	130(1)	43			
3	-0.153(5)	138(2)	87	-0.005(2)	24(6)	13			

All the spectra from Mn$_2$FeGa to Fe$_2$MnGa show a broad nearly nonmagnetic component as a major component. An exception is found in Fe$_{1.8}$Mn$_{1.2}$Ga and Fe$_{1.6}$Mn$_{1.4}$Ga, respectively, where the magnetic component prevails. In contrast, from Fe$_{2.2}$Mn$_{0.8}$Ga to Fe$_3$Ga the magnetic component drastically increases. For Fe$_2$MnGa annealed at 1100° C and Mn$_2$FeGa annealed at 800° C the investigation is reported in detail in Chapters (Fe$_2$MnGa and Mn$_2$FeGa). The results from the fitting of the Mössbauer data are given in Table 9.6.

However, in this part we discuss the compounds from Fe$_{2.2}$Mn$_{0.8}$Ga to Fe$_3$Ga, the structures of which appears to be cubic (Fm$\overline{3}$m, space group no. 225, BiF$_3$). In the regular ordered and stöchiometric cubic phase there are two iron positions, one iron corresponds to the octahedral site surrounded by four Fe atoms and four Ga atoms, and the second position of Fe in the tetrahedral sites consists of eight Fe atoms, hence, two Fe positions are expected with a different hyperfine magnetic splitting and an even ratio of the relative intensities in the resulting Mössbauer spectrum. The best resolved Mössbauer spectrum was shown by Fe$_{2.8}$Mn$_{0.2}$Ga, where the two components due to the two Fe sites are therefore readily resolved with a relative intensity of 56 % and 44 % and hyperfine magnetic fields 188(1) kOe and 130(1) kOe, respectively. The higher magnetic field (188(1) kOe) is assigned to a tetrahedral site of Fe, where the first eight neighbors of Fe are magnetic viz. eight Fe atoms. In contrast, the Mössbauer spectra of Fe$_3$Ga, Fe$_{2.6}$Mn$_{0.4}$Ga and Fe$_{2.2}$Mn$_{0.8}$Ga revealed a large distribution of hyperfine magnetic fields.

Bibliography

[1] T Graf, F Casper, J Winterlik, B Balke, G H Fecher, and C Felser. *Z. Anorg. Allg. Chem.*, 635:976, 2009.

[2] S Wurmehl, G H Fecher, K Kroth, F Kronast, H A Dürr, Y Takeda, Y Saitoh, K Kobayashi, H-J Lin, G Schönhense, and C Felser. *J. Phys. D: Appl. Phys.*, 39:803, 2006.

[3] Changhai Wang. *A chemical approach to Heusler compounds and nanoparticles.* Universität Mainz, pp. 100, 2011.

[4] T Graf, S Parkin, and C Felser. *Solid State Commun.*, 47:367, 2011.

[5] Jung V, Balke B, Fecher G, and Felser C. *Appl. Phys. Lett.*, 90:012508, 2007.

[6] S Ouardi, G H Fecher, B Balke, A Beleanu, X Kozina, G Stryganiuk, C Felser W Klöss, H Schrader F Bernardi, J Morais, E Ikenaya, Y Yamashita, S Ueda, and K Kobayashi. *Phys. Rev. B*, 84:155122, 2011.

[7] M Meinert, J M Schmalhorst, C Klewe, G Reiss, E Havenholz, T Böhnert, and K Nielsch. *Phys. Rev. B*, 84:132405, 2011.

[8] P Klaer, C A Jenkins, V Alijani, J Winterlik, B Balke, C Felser, and H J Elmers. *Appl. Phys. Lett.*, 98:212510, 2011.

[9] J Kübler, A R Williams, and C Sommers. *Phys. Rev. B*, 77:1745, 1983.

[10] Y Kurtulus, R Dronskowski, G Samolyuk, and V Antropov. *Phys. Rev. B*, 71:014425, 2005.

[11] E Sasioglu, L Sandratskii, P Bruno, and I Galanakis. *Phys. Rev. B*, 72:184415, 2005.

[12] E Liu, W Wang, L Feng, W Zhu, G Li, J Chen, H Zhang, G Wu, Ch Jiang, H Xu, and F Boer. *nature communications*, 635:976, 2012.

[13] A de Campos, D Rocco, A Magnus, G Carvalho, L Caron, Adelino A Coelho, S Gama, L M da Silva1 F C G Gandra, A O dos Santos, L P Cardoso, P J von Ranke, and N A de Oliveira. *Nature Materials*, 5:976, 2006.

[14] Y Li, Ch Jiang, T Liang, Y Ma, and H Xu. *Scripta Materialia*, 48:1255–1258, 2003.

[15] C Felser, G H Fecher, and B Balke. *Angew. Chem.*, 46:668, 2007.

[16] J Winterlik, G H Fecher, B Balke, T Graf, V Alijani, C A Jenkins V Ksenofontov, O Meshcheriakova, and C Felser. *Phys. Rev. B*, 83:174448, 2011.

[17] M Meinert, J M Schmalhorst, G Reiss, and E Arenholz. *J. Phys. D: Appl. Phys.*, 44:215003, 2011.

[18] M Meinert, J M Schmalhorst, and G Reiss. *Appl. Phys. Lett.*, 97:12501, 2010.

[19] S Wurmehl, G H Fecher, H C Kandpal, V Ksenofontov, and C Felser. *Appl. Phys. Lett.*, 88:032503, 2006.

[20] S Trudel, S Gaier, J Hamrle, and H Hillebrands. *J. Phys. D: Appl. Phys.*, 43:193001, 2010.

[21] J Winterlik, B Balke, G H Fecher, and C Felser. *Phys. Rev. B*, 77:054406, 2008.

[22] H Sukegawa, Zh Wen, K Kondou, Sh Kasai, S Mitani, and K Inomata. *Appl. Phys. Lett.*, 100:182403, 2012.

[23] J C Slonczewski. *J. Magn. Magn. Materials*, 159:L1, 1996.

[24] L Berger. *Phys. Rev. B*, 54:9353, 1996.

[25] J Winterlik, B Balke, G H Fecher, C Felser, M C M Alves, F Bernardi, and J Morais. *Phys. Rev. B*, 77:054406, 2008.

[26] G E BACON and J S PLANT. *J. Phys. F: Met. Phys.*, 1:524, 1971.

[27] S Wurmehl, H C Kandpal, H C Fecher, , and C Felser. *J. Phys.: Condens. Matter*, 18:6171, 2006.

[28] J Winterlik, S Chadov, A Gupta, V Ailjani, T Gasi, K Filsinger, B Balke, G H Fecher, C A Jenkins, J Kübler, G Liu, L Gao, S Parkin, and C Felser.

[29] S Ikeda, K Miura, H Yamamoto, K Mizunuma, H D Gan, M Endo, S Kanai, J Hayakawa, F Matsukura, and H Ohno. *Nature Materials*, 9:721, 2010.

[30] Tezuka N, Ikeda N, Sugimoto S, and Inomata K. *Appl. Phys. Lett.*, 93:042507, 2008.

[31] Laurent Chapon and Juan Rodriguez-Carvajal. *FullProf, version 2.0*, 2008.

[32] P Gütlich, E Bill, and A X Trautwein. *Mössbauer Spectroscopy and Transition Metal Chemistry.* Springer 2011, 2011.

[33] K Lagarec and D G Rancourt. *Recoil, version 1.0*, 1998.

[34] Heusler F. *Verh. d. DPG*, 5:219, 1903.

[35] H C Kandpal, G Fecher, and C Felser. *J. Phys. D: Appl. Phys.*, 40:1507–1523, 2006.

[36] R A de Groot, F M Müller, P G van Engen, and K H J Buschow. *prl*, 50:2024, 1983.

[37] S Wurmehl, G H Fecher, K Kroth, F Kronast, H A Dürr, Y Takeda, Y Saitoh, K Kobayashi, H J Lin, G Schönhense, and C Felser. *J. Phys. D: Appl. Phys.*, 39:803, 2006.

[38] H J Elmers, G H Fecher, D Valdaitsev, S A Nepijko, A Gloskovskii G Jakob, G Schönhense, S Wurmehl adn T Block, and C Felser. *Phys. Rev. B*, 67:104412, 2003.

[39] B Balke, G H Fecher, H C Kandpal, C Felser, K Kobayashi, E Ikenaga, J J Kim, and S Ueda. *Phys. Rev. B*, 74:104405, 2006.

[40] P J Webster. *Contemp. Phys.*, 10:559, 1969.

[41] K Özdogan, i Galanakis, E Sasioglu, and B Aktas. *ssc*, 142:492–497, 1983.

[42] Vajiheh Alijani Zamani. *Structure and Properties of Quaternary and Tetragonal Heusler Compounds for Spintronics and Spin Transfer Torque Applications.* Universitä Mainz, 2012.

[43] G H Fecher, H C Kandpal, S Wurmel, C Felser, and G Schönhense. *J.Appl.Phys*, 99:08J106, 2006.

[44] J Kübler. *Theory of Itinerant Electron Magnetism.* Clarendon Press, Oxford, 2000.

[45] J C Slater. *Phys.Rev.*, 49:931, 1936.

[46] L Pauling. *Phys.Rev.*, 54:899, 1938.

[47] J Kübler. *Physica B+C*, 257:127, 1984.

[48] A Dannenberg, M Siewert, M E Gruner, M Wuttig, and P Entel. *Phys. Rev. B*, 82:214421, 2010.

[49] V I Goldanskii. *Chemical Applications of Mössbauer Spectroscopy*, page 75, 1968.

[50] G Klingelhöfer, R V Morris, B Bernhardt, D Rodionov, P A de Souza Jr, S W Squyres, J Foh, E Kankeleit, U Bonnes, R Gellert, C Schrder, S Linkin, E Evlanov, B Zubkov, and O Prilutski.

[51] Rajagopalan Subramanian. *Mössbauer spectroscopy, nuclear inelastic scattering and density functional theory studies on oxobridged iron complexes and their reaction under Gif-type condisions.* Institut fr Physikalische Chemie der Universität Stuttgart, pp. 165, 2010.

[52] F.E. Fujita. *Physics of New Materials*. Springer, Heidelberg, 1998.

[53] G V Kurdjumov. *Journal of Metals*, 66:449–453, 1959.

[54] L C Chang and T A Read. *Trans AIME*, 191:47, 1951.

[55] C A Jenkins, A Scholl, R Kainuma, H J Elmers, and T Omori. *Appl. Phys. Lett.*, 100:032401, 2012.

[56] P Hohenberg and W Kohn. *Phys. Rev. B*, 136:864, 1964.

[57] W Kohn and L J Sham. *Phys. Rev. B*, 140:1133, 1965.

[58] J Winterlik, G H Fecher, B Balke, T Graf, V Alijani, V Ksenofontov, C Jenkins, O Meshcheriakova, C Felser, G Liu, S Ueda, K Kobayashi, T Nakamura, and M Wojcik. *Phys. Rev. B.*, 83:174448, 2011.

[59] M Gillessen and R Dronskowskii. *J. Comp. Chem.*, 30:1290–1299, 2008.

[60] M Gillessen and R Dronskowskii. *J. Comp. Chem.*, 31:612–619, 2009.

[61] Z Ren, S T Li, and H Z Lu. *Physica B*, 405:2840–2843, 2010.

[62] J H Westbrook and R L Fleischer. page 255. 2000.

[63] M Meinert, J-M Schmalhorst, C Klewe, G Reiss, E Arenholz, T Böhnert, and K Nielsch. *Phys. Rev. B*, 84:132405, 2011.

[64] P Soven. Coherent potential model of substitutional disordered alloys. *Phys. Rev.*, 156:809–813, 1967.

[65] W H Butler. Theory of electronic transport in random alloys: Korringa-kohn-rostoker coherent-potential approximation. *Phys. Rev. B*, 31:3260–3277, 1985.

[66] M Ellner, K Kolatschek, and B Predel. *J. Less-Common Met.*, 170:171–184, 1991.

[67] P J Schurer, N J G Hall, and A H Morrish. *Phys. Rev. B*, 18:4860–4874, 1978.

[68] Jung V, Balke B, Fecher G, Ksenofontov V, and Felser C. *J. Phys. D: Appl. Phys.*, 42:084007, 2009.

[69] V Ksenofontov, M Wojcik, Sabine Wurmehl, Horst Schneider, Benjamin Balke, Gerhard Jakob, and Claudia Felser. *J. Phys. D: Appl. Phys.*, 107:9106, 2010.

[70] O Massenet, H Daver, V D Nguyen, and J P Repobouillat. *F–Metall Phys*, 9:1687, 1979.

[71] U Eberz, W Seelentag, and H U Schuster. *Z. Naturf. B*, 35:1341, 1980.

[72] H Ebert, D Ködderitzsch, and J Minár. Calculating condensed matter properties using the kkr-green's function method - recent developments and applications. *Rep. Prog. Phys.*, 74:096501, 2011.

[73] Vosko S H, Wilk L, and Nusair M. *Can. J. Phys.*, 58:1200, 1980.

[74] F Wu, S Mizukami, D Wtanabe, H Naganuma, M Oogane, Y Ando, and T Miyazaki. *apl*, 94:122503, 2009.

[75] Felser C, Fecher G H, and Balke B. *Angew. Chem. Int. Ed.*, 46:668, 2007.

[76] Kandpal H C, Fecher G. H, and Felser C. *J. Phys. D: Appl. Phys.*, 40:1507, 2007.

[77] V Alijani, J Winterlik, G Fecher, and C Felser. *Appl. Phys. Lett.*, 99:222510, 2011.

[78] H Z Luo, H W Zhang, Z Y Zhu, L Ma, S F Xu, G H Wu X X Zhu, C B Jiang, and H B Xu. *jap*, 103:083908, 2008.

[79] J Winterlik, D Schaerf, B Balke, G H Fecher, C Felser, R Dinnebier, M Jansen, and S P Parkin. *unpublished result*, 2010.

[80] T Gasi, A K Nayak, M Nicklas, and C Felser. *J. Appl. Physics*, x:x, 2012.

[81] H van Leuken and R A de Groot. *Phys. Rev. B*, 95:1171, 1995.

[82] B Balke, G H Fecher, J Winterlik, and C Felser. *Appl. Phys. Lett.*, 90:152504, 2007.

[83] M. Venkatesan P. Stamenov H. Kurt, K. Rode and J. M.D̃. Coey. *Phys. Rev. B*, 83, 2011.

[84] A K Nayak, Sh Chandra, J Winterlik, A Gupta, and C Felser. *Appl. Phys. Lett.*, 100:152404, 2012.

[85] A T Zayak, P Entel, K M Rabe, W A Adeagbo, and M Acet. *prb*, 83:020405, 2011.

[86] Y V Kudryavtsev, N V Uvarov, V N Iermolenko, I N Glavatskyy, and J Dubowik. *Adv. Materials*, 60:4780, 2012.

[87] X D Tang, W H Wang, W Zhu, E K Liu, G H Wu, F B Meng, H Y Liu, and d H Z Luo. *Appl. Phys. Lett.*, 97:242513, 2010.

[88] T Omori, K Watanabe, R Y Umetsu, R Kainuma, and K Ishida. *Appl. Phys. Lett.*, 95:082508, 2009.

[89] S Singh, M Maniraj, S W DSouza, R Ranjan, and S R Barman. *Appl. Phys. Lett.*, 96:081904, 2010.

[90] S B Roy, G K Perkins, M K Chattopadhyay, A K Nigam, K J S Sokhey, P Chaddah, A D Caplin, and L F Cohen. *prb*, 92:147203, 2004.

[91] J Nogués, J Sort, V Langlais, V Skumryev, S Suri nach, J S Mu noz, and M. D. Baré. *Phys. Rev.*, 65:422, 2005.

[92] Fernando Palacio, Eric Ressouche, and Jacques Schweizer. *Introduction to Physical Techniques in Molecular Magnetism: Structural and Macroscopic Techniques.* Springer 2011, 2011.

[93] M Khan, I Dubenko, S Stadler, and N Ali. *Appl. Phys. Lett.*, 91:072510, 2007.

[94] H C Xuan, Q Q Cao, C L Zhang, S C Ma, S Y Chen, D H Wang, and Y W Du. *Appl. Phys. Lett.*, 96:202502, 2010.

[95] T Omori, K Watanabe, X Xu, R Y Umetsu, R Kainuma, and K Ishida. *Scripta Materialia*, 64:669–672, 2011.

[96] Olga Mescheriakova. canted magnetism in mn$_2$rhsn heusler compound. 2012.

[97] G Grosse, F E Wagner, V E Antonov, and T E Antonova. *J. Appl. Cryst.*, 253-254:339–342, 1997.

[98] W J Feng, D Li, W J Ren, Y B Li, W F Li, J Li, Y Q Zhang, and Z D Zhang. *J. Alloys Comp.*, 437:27–33, 2007.

[99] H Y Yasuda, M Aoki, Y Oda, K Fukushima, and Y Umakoshi. 165:012053, 2009.

[100] D C Liu, J Q Li, M Ouyang, F S Liu, and W Q Ao. *J. Alloys Comp.*, 479:134–139, 2009.

[101] Alison B Flatau. *Department of Aerospace Engineering*, 2009.

[102] L R Newkirk and C C Tsuei. *Appl. Phys. Lett.*, 42:5250–5253, 1971.

[103] P Panissod, J Durand, and J I Budnick. *Nucl. Inst. Methods*, 99:199, 1982.